



**HAL**  
open science

# Post Examination of a High Flux Reactor Single Element with Ultra-Sounds

Ghita Zaz

► **To cite this version:**

Ghita Zaz. Post Examination of a High Flux Reactor Single Element with Ultra-Sounds. Electronics. Université Montpellier, 2015. English. NNT : 2015MONT252 . tel-02160964

**HAL Id: tel-02160964**

**<https://theses.hal.science/tel-02160964>**

Submitted on 20 Jun 2019

**HAL** is a multi-disciplinary open access archive for the deposit and dissemination of scientific research documents, whether they are published or not. The documents may come from teaching and research institutions in France or abroad, or from public or private research centers.

L'archive ouverte pluridisciplinaire **HAL**, est destinée au dépôt et à la diffusion de documents scientifiques de niveau recherche, publiés ou non, émanant des établissements d'enseignement et de recherche français ou étrangers, des laboratoires publics ou privés.

# THÈSE

Pour obtenir le grade de  
Docteur

Délivré par l'**Université de Montpellier (UM)**

Préparée au sein de l'école doctorale  
**Information Structures Systèmes (I2S)**

Et de l'unité de recherche  
**Institut d'Électronique et Systèmes (IES)**  
**UMR CNRS 5214**

Spécialité : **Électronique, Composant et Systèmes**

Présentée par **Mme. Ghita ZAZ**

**Post Examination of a High Flux Reactor  
Single Element with Ultra-Sounds**

Soutenue le 14 Décembre 2015 devant le jury composé de

Mr. Alain FOUCARAN, Professeur, Institut d'Électronique et des Systèmes, Université de Montpellier.	Président
Mr. Philippe BENECH, Professeur, IMEP-LAHC, Grenoble INP.	Rapporteur
Mr. Emmanuel MOULIN, Professeur, IEMN-DOAE, Université de Valenciennes et du Hainaut-Cambrésis.	Rapporteur
Mr. Abdeslam HOUMMADA, Professeur, Académie HASSAN II des Sciences et Techniques, Rabat, Maroc.	Examineur
Mr. Mustapha BENNOUNA, Professeur, Université Euro-Méditerranéenne, Fès, Maroc.	Examineur
Mr. Yoann CALZAVARA, Docteur - Chef de service, Institut Laue-Langevin, Grenoble.	Examineur
Mr. Laurent DUSSEAU, Professeur, Institut d'Électronique et des Systèmes, Université de Montpellier.	Invité
Mr. Gilles DESPAUX, Professeur, Institut d'Électronique et des Systèmes, Université de Montpellier.	Directeur de thèse
Mr. Emmanuel LE CLEZIO, Professeur, Institut d'Électronique et des Systèmes, Université de Montpellier.	Co-encadrant de thèse



***“Learn from yesterday, live for today, hope for tomorrow. The important thing is not to stop questioning.”***

*Albert Einstein*

## **Acknowledgment:**

*This work was achieved within the team of Materials, Micro-sensors and Acoustic (M2A) of the Institute of Electronics and Systems (IES) of the University of Montpellier (UM).*

*The Professor Alain FOUCARAN welcomed me into his laboratory (IES). I want to thank him for allowing me to integrate myself into the IES life.*

*I extremely grateful to Pr. Emmanuel Le Clezio and Pr. Gilles Despaux, my supervisors, for the three years that allowed me to progress scientifically and humanly. I would like to thank them again to make me discover the world of research.*

*I sincerely thank Dr. Yoann Calzavara for its hospitality at the ILL, his confidence and support.*

*I want to thank Laurent Podevin and Alain Portal respectively assistant engineer and study engineer in the IES for their contributions in the achievement of the ultrasonic sensors and the associated electronics.*

*I warmly thank all my friends that I have discovered during this thesis for their good humor and for their help: Céline Engrand, Ali Dekious, Pierre-Antoine Meignen, Redha Boubenia.*

*I also want to thank all the members of the IES institute and especially the M2A team.*

*My profound thanks go to my parents for their precious support throughout my university studies.*

*I also thank my two little brothers for their encouragement.*

*Abdessalam, you have accepted the distance (France/Morocco) during these three years and you have always encouraged me to trace my way. Thank you! I thank God for giving us our little Yasmine which further beautifies our lives.*

## Résumé :

Le Réacteur à Haut Flux (RHF) de l'Institut Laue-Langevin (ILL), uniquement dédié à la recherche fondamentale, produit le flux continu de neutrons thermiques le plus intense au monde, soit  $1.5 \cdot 10^{15}$  neutrons par seconde et par  $\text{cm}^2$ , avec une puissance thermique de 58 MW. Ce réacteur possède un cœur constitué d'un élément combustible unique en uranium très enrichi. La modération est assurée par de l'eau lourde afin de ralentir les neutrons produits par la réaction de fission au sein du réacteur. Le réservoir d'eau lourde contenant l'élément combustible est ensuite situé dans une piscine remplie d'eau déminéralisée qui assure une protection vis-à-vis des rayonnements neutrons et gammas.

Plus en détail, l'élément combustible qui sert à faire fonctionner le réacteur est constitué de 280 plaques maintenues entre deux viroles concentriques. Les plaques d'une épaisseur de 1.27 mm, renferment l'uranium hautement enrichi (>93% d' $^{235}\text{U}$ ) et sont cintrées en développante de cercle afin de maintenir une distance constante entre chaque plaque. Cette distance appelée « canal d'eau » sert de passage de l'eau de refroidissement. La largeur du canal d'eau est de 1.8 mm au nominal.

Dans le cadre d'une étude sur le comportement des éléments combustibles après irradiation, l'ILL souhaite développer un dispositif capable d'aller mesurer la largeur du canal d'eau. Cette mesure permettra de caractériser le gonflement des plaques, inhérent à l'irradiation, ainsi que les modifications de structure (corrosion, décollement,...). Cependant, cette mesure de distance est délicate puisqu'une résolution de l'ordre du micromètre est recherchée alors que la dimension de l'espace inter-plaques est proche du millimètre. Les contraintes d'accès sont également difficiles du fait que l'élément combustible est placé à environ 5 m sous la surface de l'eau. En outre, tous les systèmes sont soumis à de fortes radiations.

Basés sur des méthodes magnétiques, capacitatives ou optiques, des dispositifs permettent aujourd'hui de mesurer des distances avec une résolution nanométrique et avec des fonctionnalités pouvant être adaptées dans des conditions de températures et de pressions difficiles. Ces méthodes ne peuvent cependant pas être appliquées à des systèmes fortement radiatifs ou en immersion. Afin de répondre à cette problématique, deux transducteurs ultrasonores fonctionnant en émission-réceptions ont été conçus, étudiés et ensuite développés dans le cadre de cette thèse. Ces transducteurs sont montés sur une lame en acier inoxydable de 1 mm d'épaisseur afin d'autoriser l'accès à l'espace inter-plaques. Du fait de la haute résolution recherchée, les transducteurs sont excités à une fréquence au-delà de 120 MHz et intégrés dans un ensemble d'instruments de mesure comprenant un système d'acquisition haute fréquence, un traitement de signal de haute précision et une électronique spécifique développée pour améliorer le signal d'excitation.

Connaissant la vitesse du son dans l'eau et l'épaisseur de la lame, les transducteurs mesurent la distance inter-plaque à partir de la détermination du temps de vol entre l'émission d'un pulse ultrasonore et la réception des échos réfléchis sur la surface de chacune des plaques.

Montés à l'une des extrémités de la lame, les éléments de transductions possèdent chacun la même structure multicouche composée essentiellement d'une pastille en matériau piézoélectrique sur laquelle est placée une électrode en aluminium. Sur l'autre surface de la pastille une couche conductrice en or est déposée. L'intégralité de ce système est ensuite collée sur une ligne à retard en silice.

## Post Examination of the RHF Single Element with Ultra-Sounds

---

En hautes fréquences, la structure multicouche des capteurs joue un rôle dans la forme des signaux émis et reçus. En effet, lorsqu'une impulsion de tension est appliquée à l'électrode du transducteur, un champ électrique est créé faisant entrer l'élément piézoélectrique en vibration. L'onde ultrasonore produite par vibration de l'élément piézoélectrique se propage dans la ligne à retard en silice, ensuite se reflète partiellement sur la face interne de la silice tandis que le reste du signal se propage à travers l'eau pour se réfléchir sur la plaque combustible. Par réciprocity, chaque transducteur acquiert les échos réfléchis provoquant ainsi une déformation de la pastille piézo-électrique qui fait apparaître des charges électriques et donc une tension est générée à la sortie du transducteur. Du fait de la présence des différentes interfaces, un signal caractéristique de la structure du capteur est constitué d'une série de salves et acquit. Afin d'optimiser les propriétés géométriques et mécaniques des différentes couches des capteurs et d'identifier leurs influences sur la structure temporelle des signaux finaux, les structures multicouches ont été modélisées et des images acoustiques de microscopie ultrasonore ont été réalisées afin de vérifier la qualité des transducteurs (planéité, fissures...).

Une expérience in-situ conduisant à une première série de mesures de distance inter-plaque a été réalisée au sein de l'élément combustible irradié du réacteur à haut flux de l'ILL. Lors de cette expérience, le sabre instrumenté est guidé pour venir se positionner sur un canal d'eau. Il est ensuite glissé parallèlement aux plaques combustibles le long du canal d'eau pour effectuer des mesures en continu. De manière à autoriser la manipulation du capteur ultrasonore à une distance correspondant à la profondeur de l'élément combustible étudié (5 m sous l'eau), une extension tubulaire en acier inoxydable a été reliée au capteur. Les résultats obtenus durant cette expérience montrent clairement que, malgré la forte nature radiative de l'environnement, la qualité des signaux ultrasonores était suffisante pour assurer une identification stable des distances inter-plaques. Cette expérience a également prouvé que les différents composants du capteur ultrasonore, en particulier la ligne à retard en silice et l'élément piézoélectrique ont présenté une bonne tenue aux radiations. Bien que la validité des valeurs absolues obtenues doive encore être confirmée, l'excellente résolution relative, de l'ordre de quelques microns, semble déjà permettre d'identifier des zones de rétrécissement de l'espace inter-plaque. La faisabilité de la mesure de la distance inter-plaque a donc été prouvée et les contraintes expérimentales liées au protocole de mesure ont été identifiées. La dépendance en température des mesures a été considérée comme un paramètre important nécessitant le développement d'un outil permettant la mesure de la température du canal d'eau. En effet, la précision de la mesure de distance dépend de l'évaluation du temps de vol d'une onde ultrasonore et de sa vitesse dans l'eau qui varie en fonction de la température.

Pour améliorer à la fois, la fiabilité et la précision, du système de mesure de distance, un dispositif permettant l'identification de la température du canal d'eau a été étudié, ensuite développé dans le cadre de cette thèse. Bien que les techniques de mesure de la température par contact (thermocouple, les sondes à résistance...) ou optiques (La thermographie infrarouge, la Microscopie à thermorélectance ...) peuvent être trouvées dans la littérature, nous proposons une technique basée sur l'analyse des composantes spectrales d'un signal acoustique qui se propage à l'intérieur de la structure du transducteur. En effet, lorsque les transducteurs sont immergés dans le canal d'eau, la variation de la température conduit à une dilatation thermique de leur structure multicouche, en particulier celle de l'élément piézoélectrique. La dilatation thermique de ce dernier a pour effet la variation de son épaisseur, la variation de la vitesse du son dans le matériau et par conséquent la variation de la fréquence de résonance du transducteur. Grâce à cette technique, une courbe traçant la variation de la fréquence de résonance du transducteur en fonction de la température a été réalisée à partir de laquelle la température de l'eau peut être déduite.

## Post Examination of the RHF Single Element with Ultra-Sounds

---

L'étape suivante était l'évaluation des performances du capteur ultrasonore haute fréquence, dans des conditions normales, afin de déduire les différentes sources d'erreurs liées au système de mesure. Dans ce but, un processus d'étalonnage a été réalisé permettant la mesure de la vitesse d'une onde ultrasonore dans l'eau, contenue dans un réservoir ayant une épaisseur connue. Les résultats de ce système étaient proches de ceux précédemment proposés dans la littérature avec une erreur inférieure à 2%, prouvant ainsi la fiabilité et la précision de dispositif à ultrasons.

Une seconde expérience est ensuite effectuée dans un élément combustible irradié du réacteur à haut flux. Les mesures ont été réalisées par un dispositif ultrasonore, fonctionnant à des fréquences allant jusqu'à 120 MHz et ayant les dimensions suivantes : une épaisseur de 1 mm, une largeur de 10 mm et une longueur d'environ 1500 mm. Ces dimensions ont permis au capteur d'être facilement inséré entre les plaques combustibles et de glisser le long du canal d'eau.

Au cours de cette expérience, des mesures quantitatives de la distance inter-plaques ont été obtenues dans différents canaux d'eau. Des résultats en accord aux valeurs spécifiées par le fabricant de plaques combustibles ont été trouvés et de légères variations indiquent probablement des modifications de l'épaisseur du canal d'eau. La faisabilité de la mesure de température du canal d'eau a également été prouvée. Les résultats montrent clairement que, malgré la nature fortement irradiée de l'environnement, la qualité des mesures était suffisante pour assurer une identification stable de la température du canal d'eau. Les contraintes expérimentales attachées au protocole de mesure sont en phase d'analyse afin de permettre, dans les études futures, d'améliorer la précision des résultats.

Les perspectives de cette thèse sont nombreuses. Dans un premier temps, un système de guidage, est conçu pour faciliter l'insertion du capteur dans l'élément combustible et stabiliser sa position entre les plaques. La position verticale de la lame sera enregistrée afin de pouvoir corréler les mesures avec la position du capteur. Celui-ci pourra également être positionné sur trois rayons différents (coté virole intérieure, virole extérieure et au milieu) et dans les 280 canaux. L'ensemble sera piloté à partir d'une plateforme située au-dessus de l'eau.

Ensuite, afin d'améliorer la précision des mesures, un nouveau dispositif ayant deux transducteurs focalisés est conçu. Cette étape nécessitera cependant le développement de modèles plus complexes autorisant la compréhension des phénomènes relatifs à la propagation des ondes au sein de structures non planes.

Dans des études à venir, le capteur ultrasonore doit pouvoir caractériser d'autres modifications de la structure de plaques combustibles irradiées, dont la première sera l'identification d'une couche d'oxyde d'aluminium apparaissant sur la surface des plaques. Cette couche estimée à 10  $\mu\text{m}$  doit donc être caractérisée par la plus grande précision disponible. L'ILL souhaite également imager l'interface entre le revêtement des plaques et le combustible, où les bulles de gaz de fission peuvent apparaître et conduire ainsi à des effets de gonflement par exemple.

# Post Examination of the RHF Single Element with Ultra-Sounds

---

## **Abstract**

The fuel elements of High Performance and Research Reactors are usually made of plates instead of rods. During irradiation, the fuel plates undergo limited swelling and an oxide layer appears on the outer surface of the cladding. However, measuring the inter-plate distance of such fuel elements isn't trivial mainly because of the requested resolution to be obtained in constraint geometry. Indeed while the typical dimensions of the water channel between plates is close to two millimeter, a resolution of one micron is needed to characterize any fuel plate swelling. In order to perform such measurements, we designed a robust device based upon high frequency ultrasonic probes and adapted to the high radiation environment. It was thinned until 1 mm in order to be inserted into the 1.8 mm width water channel. To achieve the expected resolution, the system is excited with frequencies up to 120 MHz. Thanks to a highly performing signal processing, distance measurement is carried out through the ultrasonic waves' time of flight. One of the crucial points is then the evaluation of the local water temperature inside the water channel. To obtain a precise estimation of this parameter, the ultrasonic sensor is used as a thermometer thanks to the analysis of the spectral components of the acoustic signal propagating inside the sensor multilayered structure. The feasibility of temperature and distance measurement has already been proved with success on a full size irradiated fuel element of the Laue-Langevin Institute RHF. Some experimental constraints were identified to improve the accuracy of the measurement system in future works.

---

---

## Summary

Abstract.....	3
<b>General Introduction.....</b>	<b>8</b>
References .....	12
<b>Chapter I: Background.....</b>	<b>14</b>
I. Introduction.....	16
II. The High Flux Reactor (HFR).....	17
1. General description of the installation.....	17
2. The fuel element .....	18
3. The fuel plates .....	18
III. Conversion into LEU high density fuel.....	19
IV. LEU Uranium-Molybdenum (UMo) alloy.....	20
1. U(Mo) dispersion fuel performance.....	21
2. U(Mo) plate swelling: .....	22
V. Need of Post Irradiation Examination on the RHF LEU fuel elements .....	22
VI. Post Irradiation Examination .....	25
1. Non-Destructive analyses.....	25
5.1 Visual inspection in hot-cell.....	25
5.2 BONAPARTE measuring bench .....	26
5.3 Gamma spectrometry.....	26
5.4 Burnup profilometry.....	27
5.5 Microscopy acoustic .....	27
2. Destructive analyses.....	28
5.6 Optical microscopy (OM).....	28
5.7 Scanning electron microscopy (SEM) .....	28
5.8 Electron-Probe Microanalysis (EPMA).....	29
5.9 X-ray diffraction.....	29
VII. Distance measurement techniques.....	29
1. Optical measurement.....	30
2. Capacitive measurement.....	32
3. Magnetic measurement .....	34
4. Ultrasonic measurement .....	35
4.1 Time-of-flight measurement and estimation .....	36
4.2 Measurement resolution and accuracy.....	38
VIII. Conclusion .....	39
List of Figures .....	40
Reference.....	41

<b>Chapter II: The high frequency ultrasonic device</b> .....	48
I. Introduction.....	50
II. Measurement principles .....	51
III. Transduction elements design .....	52
IV. Model of the ultrasonic transducer.....	55
1. Principle.....	55
2. Application.....	56
3. Results .....	60
V. Manufacturing of the ultrasonic transducer .....	61
VI. Structure control .....	63
VII. Mechanical holder: Blade and support .....	64
VIII. Electronic system.....	65
IX. The high frequency ultrasonic signal.....	67
X. Processing signal.....	69
XI. Conclusion .....	72
List of Figures .....	73
Reference.....	74
<b>Chapter III: Temperature &amp; velocity measurements</b> .....	78
I. Introduction.....	80
II. Temperature measurement .....	80
1. Techniques of temperature measurement .....	80
2. Resonant frequency change: the most relevant technique .....	81
3. The experimental set-up .....	84
4. Results .....	85
III. Velocity measurement .....	87
1. Principle.....	87
2. The experimental set-up .....	88
3. Results .....	88
IV. Estimation of the experimental uncertainty .....	89
V. Conclusion .....	92
List of Figures .....	93
Reference.....	94
<b>Chapter IV: Experiments on a real RHF spent fuel element</b> .....	96
Summary.....	97
I. Introduction.....	98
II. The first experiment on a full size irradiated fuel element of the RHF.....	98
1. The experimental set-up .....	98
2. Results and discussions .....	99

---

3.	Experimental feedback.....	100
III.	The second experiment on a full size irradiated fuel element of the RHF.....	101
1.	The experimental set-up .....	101
2.	Water pool temperature measurements.....	102
3.	Water channels temperature measurements.....	103
3.1	Temperature measurements of the first water channel.....	103
3.2	Temperature measurements of the second water channel.....	105
4.	Distance measurements before irradiations.....	107
5.	Water channel distance measurements post-irradiations.....	108
5.1	The first water channel thickness measurements post-irradiations.....	108
5.2	The second water channel thickness measurements post-irradiations.....	109
6.	Experimental feedbacks .....	111
IV.	Conclusion .....	114
	List of Figures .....	115
	Reference.....	116
	Conclusion & Prospects .....	117
	Conclusion and Prospects .....	118
	Glossary.....	121
	Appendix .....	123
	Appendix 1: Parameters of the Transfer Matrix Method .....	124
	Appendix 2: Acquisition software.....	125
	Appendix 3: Signal processing .....	127
	Appendix 4: Temperature measurement .....	129
	Communications .....	132





# General Introduction



## General Introduction

Historically, uranium enriched up to >90%  $^{235}\text{U}$  has been used in peaceful applications for approximately half of the research reactors [1]. However, the use of High Enriched Uranium (HEU) for civil applications is considered as a proliferation concern. Since the 1970's, global efforts are being devoted to replace the highly enriched, low-density research reactor fuel with high-density, low enriched (<20%  $^{235}\text{U}$ ) fuel [2].

In this context, the Institute Laue-Langevin (ILL) committed for decades, under the Memorandum of Understanding (MoU) between the ILL and the US Department of Energy granted in 1998, to convert its reactor, the RHF (Réacteur à Haut Flux) into low enriched uranium (LEU) high density fuel. The RHF based in Grenoble, France, is a research reactor designed for neutron beam experiments for fundamental science. It delivers one of the most intense neutron fluxes in the world. The reactor has a single fuel element with 280 involute-shaped fuel plates and is moderated by heavy water. Now deeply engaged in the conversion process, the ILL has designed an optimized LEU fuel element, which increases the total amount of fuel without changing the external plate dimensions. This proposed design is based upon the high density LEU fuel being qualified [3]. However, the qualification of a new fuel is a real concern. Thus, post irradiation examinations (PIE) of the new fuel element have to be carried out in order to achieve the qualification process. Post irradiation examination techniques lead to a better understanding of materials behavior. Historically, these techniques have contributed to the development of the design and the operation of all reactor systems. There are two kinds of PIE techniques: destructive and non-destructive.

As the name suggests, destructive testing (DT) includes methods where the inspected material is broken down in order to determine its mechanical properties. Destructive testing techniques include micro structural studies, elemental and isotopic analysis, measurement of physical and mechanical properties, etc [4].

Nondestructive testing (NDT) is related to a wide group of analysis techniques used in science and industry to evaluate the properties of a material, component or system without causing any damage. Because NDT does not permanently alter the article being inspected, it is a highly-valuable technique that can save both money and time in product evaluation. Common NDT methods for fuel element inspection include dimensional measurements, oxide layer thickness measurements, gamma scanning and tomography, neutron and X-ray radiography, etc [4], [5]. The feasibility of these techniques (NDT and DT) for the RHF has already been assessed. The total cost of such a project would be tremendously high. Moreover, the implementation of these techniques may require very rigorous precautions to be used.

Distance measurement between fuel plates can provide an alternative solution to these issues. It will make possible the assessment of the fuel plate swelling, i.e. the cooling channel thickness variation. This parameter is rich of information especially regarding the element irradiation history. However, the inter-plate distance identification is difficult because a high resolution is sought due to the microscopic structure modifications of the plates while the inter-plate distance is close to two millimeters (nominal distance of 1.8 mm). Furthermore, the access of the involute curved fuel plates located five meters below the surface of the water pool is very difficult. The measurement devices will thus be subject to a high-level of radiations.

# Introduction

---

Several methods could be considered for performing distance measurements. Optical [6]–[8], magnetic [9]–[13], capacitive [14], or other [15] (micro-waves sensor, tunneling sensors...) devices might be relevant and reach today the nanometer resolution even in high-temperature and/or high-pressure environments. However, they may not be integrated between the fuel plates where space is very limited or may not meet the requirement for high radiations. Some of them cannot even be immersed.

Designing ultrasonic sensors seems to be a wise choice for measuring the inter-plate distance. Indeed the latter are widely used in industrial applications for measuring both distance and velocity in the propagation medium. Advantages of large number of ultrasonic sensors include their small size, simple hardware and radiation resistance. The operating principle is based on the measurement of the time of flight (ToF), that is, the time necessary for an ultrasonic wave to travel from the transmitter to the receiver after being reflected from the facing object. The object's distance is estimated from the product of the TOF and the propagation velocity of an ultrasonic wave. Different techniques can be used to generate ultrasonic waves. Among them, continuous wave [16] and pulse echo [17] techniques. In the first method, the transmitter generates a continuous output, whose echo is detected by a separated receiver. Accuracy depends on the measurement of phase shift between the transmitter and the received wave. With the pulse echo techniques a short pulse is generated, enabling the same transducer to be used both as a transmitter and as a receiver [18].

The solution proposed in this thesis is a double-sided high-frequency ultrasonic device. It includes two transducers designed to be set on both sides of a blade with the constraint of a 1 mm total device thickness. Based on the pulse-echo method, each transducer allows distance measurements through the recording of the time of flight (ToF) of the signal reflected from the fuel plates surfaces. To achieve the expected resolution, the system is integrated into a set of high frequency acquisition instruments and excited with frequencies up to 120 MHz.

In the framework of this research project, the developed transducers have been tested with success between fuel plates of High Performance Research Reactor spent fuel element, proving the feasibility of such challenging measurement. Moreover, it was demonstrated that the different components of the ultrasonic transducers showed good resistance to radiations. Furthermore, the quality of the signal to noise ratio was clearly sufficient to obtain a very stable estimation of the interpolate distance. Experimental constraints were also identified and the temperature dependence of the ultrasonic velocity has been considered as a crucial parameter. To ensure the reliability of the distance measurement, this thesis deals also with the development of a device allowing the measurement of the water channel temperature. While contact [19] or optical [20] methods can be found in the literature, we propose a new technique based upon the analysis of the spectral components of an acoustic signal that propagates inside the transducer structure, the dimensions of this latter varying with thermal expansion.

To improve measurements' reliability and accuracy, a second optimized device have been designed and manufactured, taking into account the feedback from the first measurement. This updated device has been tested in a second experiment performed within the RHF fuel element. During this latter, quantitative distance measurements were performed and appropriate distance measurement results compared to the values specified by the fuel plate manufacturer have been found. Moreover, the feasibility of the temperature measurements was also proved. Results clearly showed that in spite performing measurement, for a long time, in highly irradiative environment, the quality of the measurements was sufficient to

# Introduction

---

ensure a stable identification of the water channel temperature while some flaws may still have to be corrected to perform an absolute measurement in future works.

## Overview of the different chapters

The main objective of this thesis is to provide a tool for non-destructive post irradiation examinations of High Performance Research Reactor spent fuel elements with a microscopic resolution. A device using two ultrasonic sensors, radiation resistant, has been developed for such applications. Design, studies, modeling, manufacturing and experiments have been carried out to achieve this under collaboration between the Institute Laue-Langevin (ILL) and the Institute of Electronics and Systems (IES).

The first chapter of this document gives a detailed description of the high flux reactor and, in particular, of the fuel element in which the fuel plates are arranged. Then, it describes the conversion process of research reactors: from HEU to alternative fuels using LEU. In this context, post irradiation examination (PIE) of the new fuel elements have to be carried out in order to achieve the qualification process. Therefore, the last section of this chapter focuses on different post irradiation examination techniques, especially, on the relevant solution: Post irradiation Examination with Ultra-Sounds.

In the second chapter, the general principle of the high frequency ultrasonic device, developed for water channel thickness measurements, i.e. inter-plate distance measurements, is presented. Then, the ultrasonic device components, including the mechanical holding and the transduction element are described. The ultrasonic wavelength is sensitive to the transducers layers and the structure of the sensors plays a central role in the shape of transmitted and received signals. These latter were then simulated to predict their behaviors. After presenting and commenting the simulation results, the chapter describes the manufacturing process of ultrasonic device. This device is integrated to a high frequency electronic system.

The third chapter reports a brief state-of-the-art of the temperature measurement techniques. Then it focuses on the new technique of temperature measurement developed for the water channel temperature evaluation. Then, in order to evaluate the performance of the high frequency ultrasonic device, and deduce the error sources of the measurement system, the second section of this chapter presents an experimental set-up measuring the propagation velocity of the ultrasonic wave in water according to the temperature.

Finally, the fourth chapter presents the results obtained during the first experiment on a full size irradiated fuel element proving, thus, the feasibility of distance measurement. Then, the results of the second series of experiments are presented, including the water channel thickness and temperature measurements. Through this experiment, the feasibility of temperature measurement was proved and the first series of quantitative distance measurements were obtained. At the end, the experimental constraints are identified.

## References

- [1] A. Travelli, « U.S. reduced enrichment research and test reactor (RERTR) program: accomplishments, plans, and schedules », 1980.
- [2] L. Sannen, S. van den Berghe, et A. Leenaers, « Status of the Low Enriched Uranium Fuel Development for High Performance Research Reactors », *Adv. Sci. Technol.*, vol. 94, p. 43-54, oct. 2014.
- [3] Y. Calzavara, F. Frery, F. Thomas, H. Guyon, A. Bergeron, A. Tentner, J. Stevens, et W. Haeck, « TOUTATIS: ILL CONVERSION FEASIBILITY STUDY ».
- [4] International Atomic Energy Agency, Éd., *Post-irradiation examination and in-pile measurement techniques for water reactor fuels*. Vienna: IAEA, 2009.
- [5] G. Sposito, C. Ward, P. Cawley, P. B. Nagy, et C. Scruby, « A review of non-destructive techniques for the detection of creep damage in power plant steels », *NDT E Int.*, vol. 43, n° 7, p. 555-567, oct. 2010.
- [6] J. Thiel, T. Pfeifer, et M. Hartmann, « Interferometric measurement of absolute distances of up to 40 m », *Measurement*, vol. 16, n° 1, p. 1-6, sept. 1995.
- [7] V. Lombardo, T. Marzulli, C. Pappalettere, et P. Sforza, « A time-of-scan laser triangulation technique for distance measurements », *Opt. Lasers Eng.*, vol. 39, n° 2, p. 247-254, févr. 2003.
- [8] M.-C. Amann, T. Bosch, M. Lescure, R. Myllyla, et M. Rioux, « Laser ranging: a critical review of usual techniques for distance measurement », *Opt. Eng.*, vol. 40, n° 1, p. 10-19, 2001.
- [9] S. M. Djuric, M. S. Damnjanovic, L. F. Nagy, L. D. Zivanov, et N. M. Djuric, « Displacement inductive sensor: Simulation tool algorithm », in *IEEE EUROCON 2009, EUROCON '09*, 2009, p. 671-676.
- [10] M. Jagiella et S. Fericean, « Miniaturized inductive sensors for industrial applications », in *Proceedings of IEEE Sensors, 2002*, 2002, vol. 2, p. 771-778 vol.2.
- [11] G. Lemarquand, « A variable reluctance sensor », *IEEE Trans. Magn.*, vol. 25, n° 5, p. 3827-3829, sept. 1989.
- [12] G. Y. Tian, Z. X. Zhao, R. W. Baines, et P. Corcoran, « Blind sensing [eddy current sensor] », *Manuf. Eng.*, vol. 76, n° 4, p. 179-182, août 1997.
- [13] W. Yin et A. J. Peyton, « Thickness measurement of non-magnetic plates using multi-frequency eddy current sensors », *NDT E Int.*, vol. 40, n° 1, p. 43-48, janv. 2007.
- [14] M. Sakai, « Capacitive Sensors », in *Handbook of Signal Processing in Acoustics*, D. Havelock, S. Kuwano, et M. Vorländer, Éd. Springer New York, 2008, p. 1339-1345.
- [15] A. S. Morris, « 13 - Sensor technologies », in *Measurement and Instrumentation Principles (Third Edition)*, A. S. Morris, Éd. Oxford: Butterworth-Heinemann, 2001, p. 247-270.
- [16] T. Ono, M. Kohata, et T. Miyamoto, « Ultrasonic Phase-Sensitive Rangefinder with Double Modulation Doppler-Free Method for Shallow Seafloor Survey », in *IEEE 1984 Ultrasonics Symposium*, 1984, p. 480-483.
- [17] D. Marioli, E. Sardini, et A. Taroni, « Ultrasonic distance measurement for linear and angular position control », *IEEE Trans. Instrum. Meas.*, vol. 37, n° 4, p. 578-581, déc. 1988.
- [18] D. Marioli, C. Narduzzi, C. Offelli, D. Petri, E. Sardini, et A. Taroni, « Digital time-of-flight measurement for ultrasonic sensors », *IEEE Trans. Instrum. Meas.*, vol. 41, n° 1, p. 93-97, févr. 1992.
- [19] A. J. Crandall, B. D. Cook, et E. A. Hiedemann, « Measurement of the Velocity of Sound in Water by Optical Methods », *J. Acoust. Soc. Am.*, vol. 44, no 1, p. 387-387, juill. 1968.

## Introduction

---

- [20] A. J. Crandall, B. D. Cook, et E. A. Hiedemann, « Measurement of the Velocity of Sound in Water by Optical Methods », *J. Acoust. Soc. Am.*, vol. 44, n° 1, p. 387-387, juill. 1968.

---

---

# Chapter I

## Background

---

## Summary

General Introduction .....	9
References .....	12
I. Introduction.....	16
II. The High Flux Reactor (HFR).....	17
1. General description of the installation.....	17
2. The fuel element .....	18
3. The fuel plates .....	18
III. Conversion into LEU high density fuel.....	19
IV. LEU Uranium-Molybdenum (UMo) alloy.....	20
1. U(Mo) dispersion fuel performance.....	21
2. U(Mo) plate swelling: .....	22
V. Need of Post Irradiation Examination on the RHF LEU fuel elements .....	22
VI. Post Irradiation Examination .....	25
1. Non-Destructive analyses.....	25
1.1 Visual inspection in hot-cell.....	25
1.2 BONAPARTE measuring bench .....	26
1.3 Gamma spectrometry.....	26
1.4 Burnup profilometry.....	27
1.5 Microscopy acoustic.....	27
2. Destructive analyses.....	28
2.1 Optical microscopy (OM).....	28
2.2 Scanning electron microscopy (SEM) .....	28
2.3 Electron-Probe Microanalysis (EPMA).....	29
2.4 X-ray diffraction.....	29
VII. Distance measurement techniques.....	29
1. Optical measurement .....	30
2. Capacitive measurement.....	32
3. Magnetic measurement .....	34
4. Ultrasonic measurement .....	35
4.1 Time-of-flight measurement and estimation .....	36
4.2 Measurement resolution and accuracy.....	38
VIII. Conclusion .....	39
List of Figures .....	40
Reference.....	41

## I. Introduction

In a combined effort to minimize nuclear proliferation risks, most worldwide research reactors (RR) have joined in a common project, since the 1970's, to decrease the enrichment of their fuels [1]. This project aims at replacing Highly Enriched Uranium (HEU) fuel in many civilian applications by Low Enriched Uranium (LEU) fuel. The conversion project includes the development of high-density fuels to replace the low volume-density (mostly) UAlx based HEU fuels. This led to the development and qualification of an  $U_3Si_2$  based dispersion fuel[2]. Most reactors were converted to Low-Enriched Uranium (LEU) using  $U_3Si_2$ [3], [4]. However, for the high performance reactors, the conversion could not be achieved without bearing unjustifiable performance losses with the existing fuels. As a consequence, a new high density (7.5-8.5 g/cm<sup>3</sup>) dispersed fuel based on a mixture of uranium – molybdenum (UMo) is expected to allow the conversion of compact high performance reactors [5] like the High Flux Reactor (HFR) of the Laue Langevin Institute (ILL) based in Grenoble, France. The dispersed UMo fuels possess acceptable irradiation stability, mechanical properties and corrosion resistance [6]. Nevertheless, the UMo dispersed fuel is not yet experimentally validated. Prior experiments have shown that dispersion UMo fuel can suffer a problem of swelling under irradiation [7], [8]. Fortunately, the swelling problem is controlled by the addition of Silicon to the aluminum matrix. That is the reason why the ILL decided to participate to the HERACLES program, launched in 2013 to develop a detailed roadmap focused on U-Mo dispersion fuel qualification and European High Performance Research Reactors (EU HPRR) conversions.

Thanks to a huge amount of work, the ILL and the Argonne National Laboratory (ANL) have collaborated to investigate LEU designs for the RHF reactor [9]. A promising candidate has been selected and studied. It allows an increase in the total amount of fuel without changing the external plate dimensions.

Nevertheless the LEU fuel qualification for a high performance reactor is not a trivial process. Post irradiation examinations (PIE) of the new fuel element will have to be carried out in order to achieve the qualification process. This is a strong caveat for the ILL because no PIE solution is available yet for the RHF fuel elements. The most relevant way to examine a fuel element is to carry out destructive PIE. The feasibility of this idea for the RHF has already been assessed. The total cost of such a project would be tremendously high.

That is the reason why an alternative solution has been considered: a robust device, based upon ultrasonic probes, adapted to the high radiation environment and thin enough to be inserted between two fuel plates. This is the PERSEUS project for Post Examination of the RHF Single Element with Ultra-Sounds. Design, studies, modeling, manufacturing and experiments were carried out during this thesis.

First, this chapter will describe the fuel design of the RHF reactor, in which thin curved plates, containing HEU dispersed fuel, are arranged in tube-type assemblies (fuel element). Then, background information on the conversion of research reactors operating on HEU to alternative fuels using LEU will be presented. In order to achieve the qualification process of designed RHF LEU fuel element, post irradiation examinations (PIE) are needed. In the remained of this chapter most attention will be focused on different post irradiation examinations, especially, on the relevant solution: Post irradiations Examination with Ultra-Sounds.

## II. The High Flux Reactor (HFR)

### 1. General description of the installation

The High Flux Reactor (HFR) of the Institute Laue-Langevin (ILL) is made of a unique fuel element of high enrichment Uranium cooled by heavy water (see Figure 1). It delivers one of the most intense neutron fluxes worldwide, with an unperturbed thermal neutron flux of  $1.5 \times 10^{15}$  n/cm<sup>2</sup>/s in its reflector. The reactor thermal power is 58.3 MW. However, in order to improve the fuel cycle efficiency, ILL usually decreases the power of the reactor to a thermal power of 53.3 MW (nuclear power 52 MW). Therefore, the reactor can continuously operate for 50 day cycles, followed by a shutdown to change the fuel element. In addition, there is a longer shutdown to enable necessary maintenance work to be carried out. Normally there are 4 cycles a year, providing 200 days of neutrons to a suite of 40 high-performance instruments. The reactor has only one fuel element, based upon the Oak Ridge National Laboratory High Flux Isotope Reactor (HFIR) design [10]. The heavy water tank of 2.50 m diameter, containing the fuel element, is surrounded by a light water pool which ensures the biological shielding. This water pool has a diameter of 6 m and a height of 14 m and it is placed at the center of a 60 m diameter cylindrical building. The reactor is controlled by bars absorbent of neutrons that are extracted during the consumption of uranium. It also has 5 safety bars (absorbent of neutrons), whose function is the emergency shutdown of the reactor.

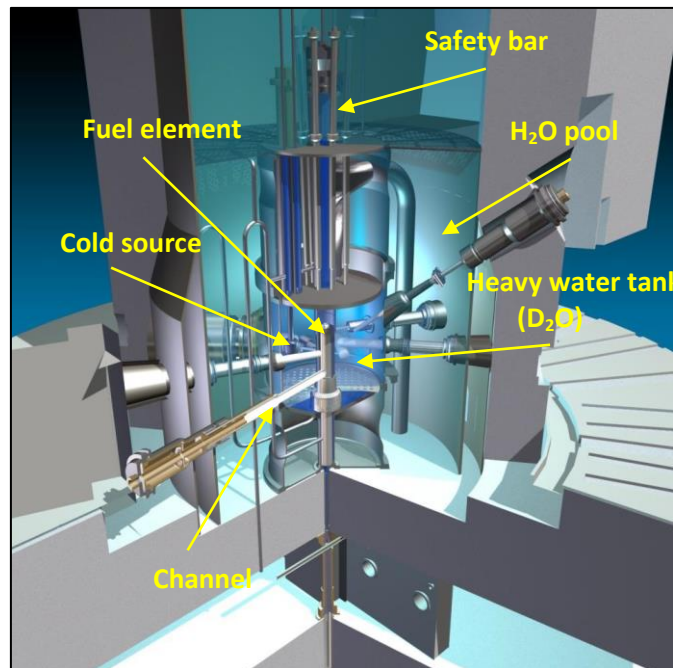


Figure 1: ILL high flux reactor

The neutrons produced by the uranium fission are extracted from the pile using beam tubes. The fission neutrons have a very high energy and must be slowed down by heavy water in order to be useful for scattering experiments on the ILL instruments. Three devices close to the fuel element can also produce hot neutrons (10 km/s) as well as cold and ultra-cold neutrons (700 m/s and 10 m/s): The hot source is made of a graphite sphere maintained at 2000 °C. Then, the more important of the two cold sources consists on a sphere containing 22

liters of Deuterium maintained in the liquid state at 25 K. Neutrons are then collected by twenty channels, some of which point on the cold sources and others on the hot ones. These channels are extended by neutron guides to feed experimental instruments out to 100 meters from the reactor [11].

## 2. The fuel element

The fuel designs differ from reactor to reactor, but can be classified as rod - or plate type. In Europe, most research reactors use plate-type fuel, in which thin plates (flat or curved), containing fissile material, are arranged in assemblies (box- or tube-type or even more complex). Most of the fuels are dispersion fuels in which the fissile material is dispersed in a matrix, mostly Al (a few exceptions exist to this, eg. Zr, ZrH, SS, ...), with an Al alloy cladding [12].

Dispersion fuels in general, consist of fuel-bearing particles dispersed in a metallic, ceramic or graphite medium. The basic idea of a dispersion fuel is to isolate the fuel particles so that a substantial volume of the matrix remains undamaged by the fission products that are ejected out of the fuel kernel. Fission products have a large kinetic energy creating defects in the matrix able to compromise the mechanical stability of the fuel plate. Therefore, in dispersion fuels, the fuel particles are contained and/or restrained, allowing much higher burn-ups than would be possible in bulk fuel [13].

Uranium aluminide-aluminum ( $UAl_x/Al$ ) dispersion fuels were used as a high-enriched fuel in many moderate- and high-power reactors around the world, namely the High Flux Reactor (RHF Grenoble).

The uranium aluminide is fabricated from a melting and casting operation and as a result usually contained a mixture of  $UAl_4$ ,  $UAl_3$  and  $UAl_2$  (a typical composition is around 63%  $UAl_3$ , 31%  $UAl_4$  and 6%  $UAl_2$ ). Such a composition is referred to as  $UAl_x$  [7], [14].

## 3. The fuel plates

To produce a fuel plate, a hot roll-bonding process is used: an assembly of a cladding plates curved around a picture frame in which a pressed compact of fuel-matrix mixture is put is hot and cold rolled to a full-size fuel plate. The middle part of the plate, containing the fissile material, is called the "meat" (see Figure 2) [13]. The fuel plates have a meat containing an enriched (93%  $^{235}U$ ) uranium-uranium alloy ( $UAl_x$ ), which is entirely covered with aluminum.

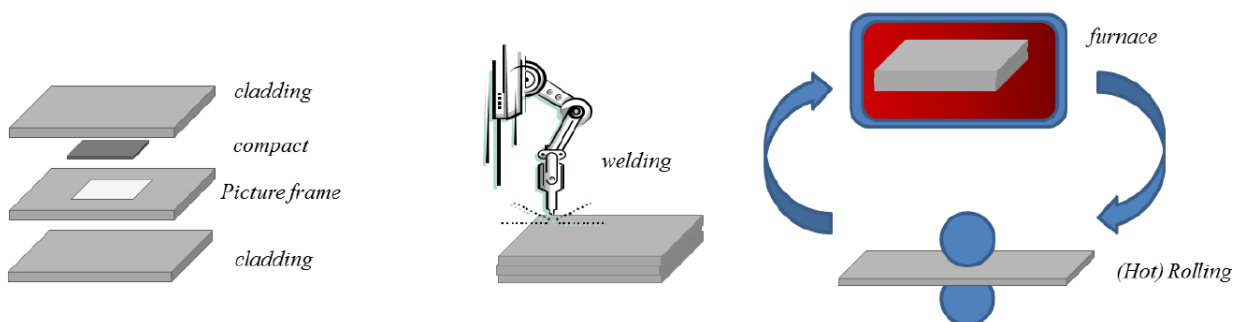


Figure 2: Schematic overview of the fuel plate production procedure

Due to its specific design, the High Flux Reactor is an assembled set of 280 aluminum curved fuel plates. It consists of regularly spaced plates (about 1.8 mm nominal) forming cylindrical tube (figures 3 & 4). These spaces allow a stream flow of water that serves as coolant and also as moderator to nuclear reaction.



Figure 3: The fuel element

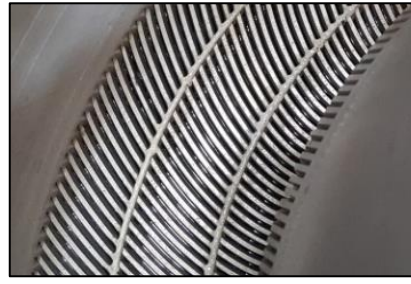


Figure 4: The fuel plates

The experimental fuel plates fabricated to be irradiated at the RHF are typically curved and have the following dimensions: 903 mm length, 69.54 mm width and a thickness of approximately 1.27 mm. The core, containing the fuel, is located in the central part of the plate and has following dimensions: nominal length ~800 mm, width ~65.14 mm. The nominal thickness of the core is approximately 510  $\mu\text{m}$ . Boron-10 burnable poisons at the tops and bottoms of the fuel plates are also manufactured (see Figure 5).

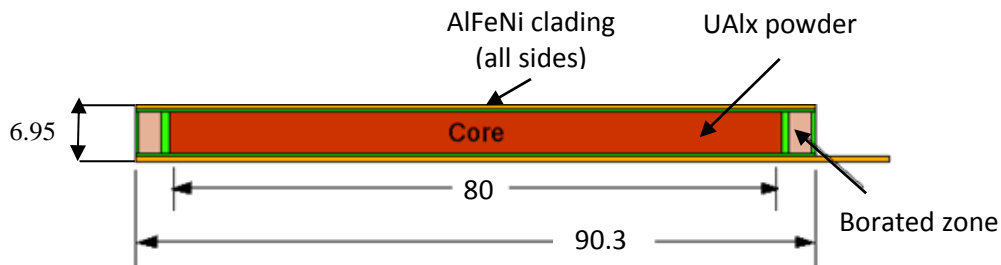


Figure 5: Top view of the fuel plate dimensions (in cm)

### III. Conversion into LEU high density fuel

Because of the proliferation risks associated to the high enrichment of the fissile material used, many programs were established for the enrichment reduction. These programs have been aiming at developing technologies to replace the high enriched uranium by a low-enriched one (less than 20 wt%  $^{235}\text{U}$ ). The European (EU) program HERACLES (Highly enriched European Reactor Action for their Conversion into Lower Enriched Solution) and the United states (US) program RERTR (Reduced Enrichment for Research and Test Reactors) are the most active today [1].

The States committed to minimize the use of HEU through the conversion of reactor fuel from HEU to LEU, where technically and economically feasible. This conversion can be achieved by:

- Increasing the U loading in the used fuels to the highest technological possible level. For UAlx/Al this means a limit of 2.3 gU/cm<sup>3</sup>.
- Changing the fuel material into another material with a higher uranium density.

All research reactors that required uranium densities lower than the technological limit were converted. For the other research reactors, needing a higher uranium loading, the high density LEU fuels are still being developed.

High density of uranium in the dispersion can only be achieved by using the dispersion of fissile compounds with high uranium content. The uranium silicides and  $U_6Fe$  compounds were initially considered promising. However, results of the irradiation performance of fuel plates is determined by excessive plate swelling, usually induced by unstable behavior of the fuel (formation of interaction layers and/or huge fission gas bubbles).

As an alternative fuel material,  $U_3Si_2$  alloy dispersion in aluminum loading to  $4.8 \text{ gU/cm}^3$ , has been developed, tested and found stable under irradiation in plate-type configurations. The  $U_3Si_2$  fuel was approved, by the U.S. Nuclear Regulatory Commission in 1988 [2], for a general use. The development and the qualification of the LEU  $U_3Si_2$  fuel have led to the conversion of nearly 90 % of the research reactors. However, many research reactors are awaiting a high-performance technology solution, needing a uranium density of  $6\text{-}9 \text{ gU/cm}^3$ . In Europe, these reactors are: BR2 (Belgium), RHF (France), FRM II (Germany) and Orphee (France).

In present state, the nearest alternative to be commercially deployed is the UMo alloy, which enables to achieve a density near to  $8 \text{ gU/cm}^3$ . This fuel is thus considered as one of the most promising candidate to convert the remaining high flux reactors, thanks to its good irradiation performance. However, it is not a commercial fuel yet.

#### IV. LEU Uranium-Molybdenum (UMo) alloy

High-density LEU fuel systems based on uranium-molybdenum (UMo) alloys are now under development for use in many high performance research reactors in the world. Uranium alloyed with molybdenum (Mo) possesses acceptable irradiation stability, mechanical properties and corrosion resistance [15]–[17]. Although it is a promising fuel, UMo dispersion fuel steel needs to be qualified for high performance research reactors. Several screening test were performed to assess the UMo alloys suitability.

Two LEU fuel systems based on the UMo alloy are now under development:

- Monolithic UMo fuel: Metallic UMo foils with a uranium density of  $15.5 \text{ gU/cm}^3$ . An LEU fuel system based on this material is being developed mainly for conversion of the U.S reactors[18].
- UMo dispersion fuel: An UMo alloy dispersed in an aluminum matrix with uranium densities up to  $8.5 \text{ gU/cm}^3$ . The conversion of the RHF and other reactors (BR2<sup>1</sup> and JHR<sup>2</sup>) are being developed based on this LEU fuel.

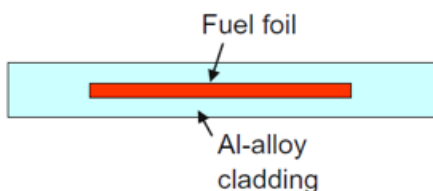


Figure 6: Monolithic fuel [19]

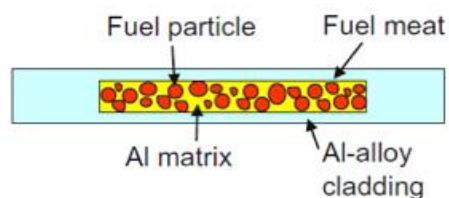


Figure 7: UMo dispersion fuel[19]

<sup>1</sup> Belgian Reactor (BR2) at the Belgian Nuclear Research Centre in Mol, Belgium.

<sup>2</sup> Jules Horowitz Reactor (JHR), under construction at the CEA Cadarache Research Centre in Cadarache, France.

## 1. U(Mo) dispersion fuel performance

UMo dispersion fuel has shown some limitations under high temperature and burnup conditions. These limitations, inducing microstructural changes, have been shown during the initial irradiations of fuel elements containing UMo dispersions:

**Interaction layer (IL)** (see Figure 8): The formation of interaction layers at the interfaces of the U-Mo particles and Al matrix during irradiation is one of the challenging issues in the development of dispersion fuel. The formation of such an IL, which has been proven to be amorphous [7][20], is substantial impact on the fuel plate behavior. The formation mechanism of interaction layers is mainly due to the interdiffusion of the U(Mo) fuel and the matrix. This interdiffusion may be simulated out-of-pile by thermal activation[21][5]. However, it was proved that for research reactors, generally operating at low temperatures, it is likely that the formation of the interaction layer in-pile is not resulting from thermally driven diffusion. It should be concluded that the formation of an interaction layer in-pile is mainly resulting from intermixing of the fuel and matrix as the interface is bombarded by fission products [14].

A significant amount of effort and research has been applied towards finding a remedy to stabilize the in-pile U(Mo) behavior. Recent developments focus on the addition of Si to the Al matrix of the fuel. The addition of these small amounts (~2 %) silicon to the aluminum phase was found to suppress the development of this interaction layer at burnups of up to 70 %. However, test irradiations (called E-FUTURE) of this fuel material at high power (~ 500 watts per square centimeter [ $\text{W}/\text{cm}^2$ ]), high uranium loadings ( $> 8 \text{ gU}/\text{cm}^3$ ), and high burnup ( $> 70 \%$ ) resulted in the formation of small blisters on the fuel plates[15], [22], [23].

As an alternative solution, the Si coating of fuel particles, by means of physical vapor deposition, was also considered and tried internationally. Follow-up experiments, under the SELENIUM project "Surface Engineering of Low Enriched Uranium-Molybdenum", were performed in 2011-2012. The post-irradiation examinations, of the tested fuel plates, showed that typical swelling has occurred and no pillowing has been observed on either plate [19]–[21].

**Recrystallization** (figure 9): The classification of the fission products in nuclear fuel is mainly based on their chemical state [9], [24]:

- Solid fission products: Some of these solid fission products will remain in solid solution during operation while others will form metallic or oxide precipitates (only in ceramic oxide fuels).
- Volatile fission products: The most abundant gases created from fission are the noble gases Kr and Xe (approximately 1/3 of all fissions). These gases, being largely insoluble in all materials, tend to precipitate into small gas bubbles and have a large impact on the microstructure and the swelling.

In fact, at high burnup, U–Mo fuel exhibits some form of recrystallization, by which fuel grains are subdivided. The effect of grain subdivision is to effectively enhance fission gas bubble swelling due to increased grain boundaries [24].

**Porosity** (figure 10): Initial irradiation testing of U-Mo dispersion fuels with pure Al as the matrix indicated that porosity, filled with fission gases, can be found between the matrix and the IL. This porosity may result in pillowing and eventual failure of fuel plates [25].

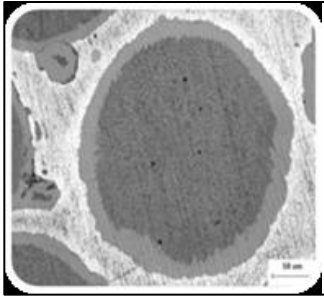


Figure 8: Interaction layer [16].

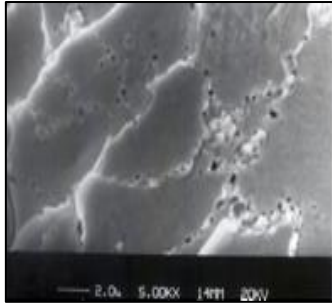


Figure 9: Fission products [22].

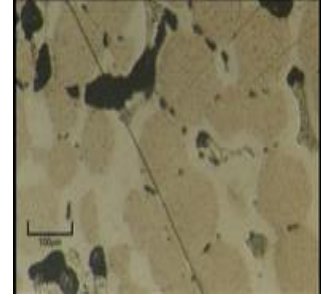


Figure 10: Porosity [16].

### 2. U(Mo) plate swelling:

Suitable irradiation behavior of dispersion fuel means:

- Dimensional stability of the fuel plate to high fissile burn-up, under expected operating conditions. No significant changes in reactivity and coolant flow must be resulted.
- The absence of cladding failure to preclude fission product.

The dimensional changes of the fuel plate are often caused by an increase in the fuel/meat thickness, while the cladding volume is almost unaffected by irradiation.

The meat swelling in U(Mo)/Al dispersion fuel is defined and quantified as consisting of two main contributions; one part caused by accumulation of fission product elements (solid and gaseous), and the other by fuel microstructural changes which include the formation of an interaction layer and porosity. Generally, the swelling phenomena depend on the local fission density.

Fuel swelling by gaseous fission products is considered the greatest factor that influences fuel performance. This swelling is affected by many parameters including burn-up, temperature, fission yield, etc. At low burn-up, the volume of gaseous fission products inside a fuel particle is considered as porosity. With increasing fission density, the gas bubbles grow and contribute significantly to the fuel swelling [26][27].

The volume change, due to solid fission products that precipitate, is affected by the partial volume of the solid fission product. The volume partial of these products can be larger than the host material's partial volume. This phenomenon leads to a net swelling.

The third phenomenon causing the fuel plate swelling is related to the formation of the layer around the fuel/meat resulting from the interaction of the fuel with the surrounding matrix during irradiation. If the density of this IL is not the same as the average of the reaction constitutes this would contribute to the overall swelling.

## V. Need of Post Irradiation Examination on the RHF LEU fuel elements

*This section is largely based on following publications [28][29].*

The RHF is currently fueled with a 93 percent enriched UAlx-aluminum dispersion fuel with boron-10 burnable poisons at the tops and bottoms of the fuel plates. The RHF is used as a neutron beam source, and a key requirement for conversion is the preservation of

## Chapter I: Background

---

“brightness” (i.e., intensity) of these beams and the reactor cycle length. The neutron brightness is a flux divided by an energy range and a solid angle. This brightness is recorded at the entrance of the ILL neutron guides, within the beam tubes. Thus, the Figure of Merit which serves as a basis for the performance evaluation is based upon variation of both the neutron fluxes and brightness in key locations. A normalized weight, which corresponds to the number of allocated beam time days at each location, has been applied to the calculation results. The nuclear reactor power, related to the cycle length, is taken into account in the flux / brightness normalization factor as a proportional value (in first approximation). Thermal hydraulics calculations have also been carried out in order to check the feasibility of the conversion and its impact on the steady state safety margin. More details in [30].

To meet the RHF reactor conversion objectives, a new fuel element design is performed that could safely replace the HEU element currently used to the use of the dispersed UMo LEU fuel. The proposed LEU design has been called TOUTATIS (French acronym: Traitement Optimisé de l'Uranium et Thermique Améliorée pour une Technologie Intégrant la Sûreté) and is being qualified by the HERACLES group.

The HERACLES program was launched in 2013, where CEA<sup>3</sup>, CERCA<sup>4</sup>, ILL, SCK-CEN<sup>5</sup> and TUM<sup>6</sup> have team-up to optimally share experience and equipment. The US/DoE is a partner of the HERACLES program. Dispersed UMo is one of the three options selected by the HERACLES group, besides high density U<sub>3</sub>S<sub>2</sub> and monolithic UMo. The group is actively developing a strategy, a road map and timeline for the future of UMo dispersion fuel development, as well as for designing further experiments, industrialization of the production processes (power and/or plate), qualification of the fuel system and the production route, etc [31]. The ILL conversion is thus strongly dependent upon the success of the HERACLES irradiation experiments.

The new RHF fuel element design has been developed to maximize performance, minimize changes and preserve strong safety margins. Neutronics and thermal-hydraulics models of the RHF have been developed and qualified by benchmark against experiments and/or against other codes and models. The models developed were then used to evaluate the RHF performance if LEU UMo were to replace the current HEU fuel 'meat' without any geometric change to the fuel plates. Results of these direct replacement analyses have shown a significant degradation of the RHF performance, in terms of both neutron flux and cycle length. Consequently, Argonne National Laboratory (ANL) and ILL have collaborated to investigate alternative designs. A promising candidate design has been selected and studied. In this design, the fueled height of the reactor core will be increased by eliminating the burnable poison zones at the tops and bottoms of the fuel plates. (These poisons will be moved to another location in the reactor) (see figure 11). With this new design, neutronics analyses have shown that performance losses could be limited to 10% or less. In addition, studies have shown that the thermal-hydraulic and shutdown margins for the proposed LEU design would satisfy technical specifications. The slight loss of brightness can be compensated for by increasing the beam times for some experiments, but it will not affect overall throughput of experiments in the reactor.

---

<sup>3</sup> Commissariat à l'énergie atomique (CEA).

<sup>4</sup> Compagnie pour l'Étude et la Réalisation de Combustibles Atomiques (CERCA)

<sup>5</sup> SCK • CEN (Dutch: Studiecentrum voor Kernenergie; French: Centre d'Étude de l'énergie Nucléaire).

<sup>6</sup> The Technische Universität München (TUM) is a research university in Munich.

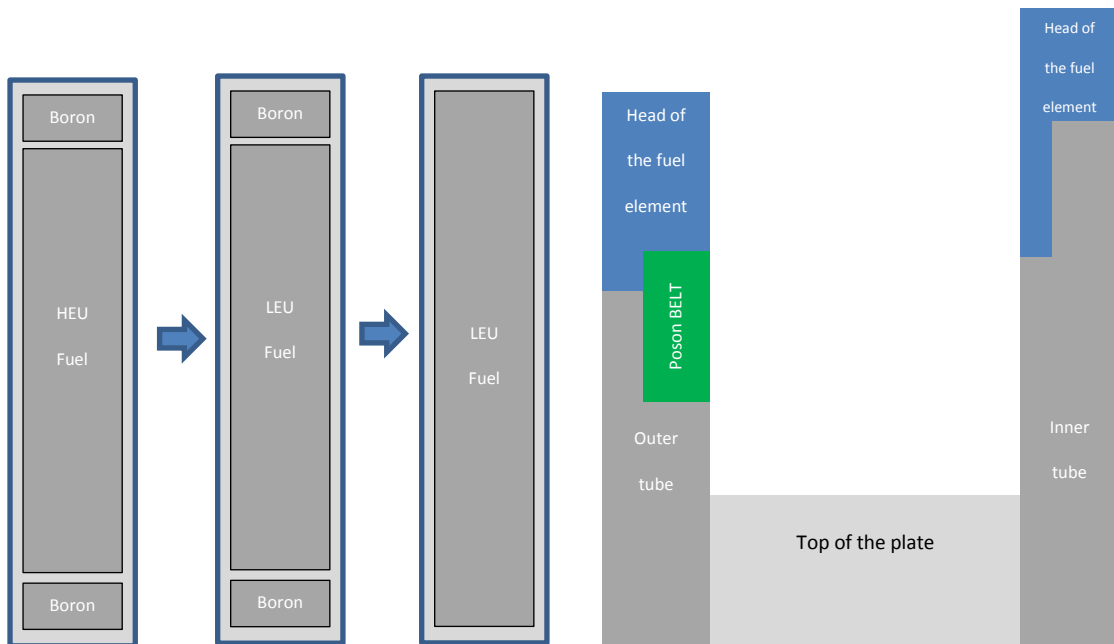


**Figure 10: Scheme of HEU plates, LEU plates as studied in a first step and TOUTATIS LEU plates. The last figure illustrates the boron location which is set above the fuel plate in the outer tube of the element.**

Nevertheless there are still a number of caveats which are conditions for the RHF possible conversion, like success of the HERACLES experiments, the commercialization of the UMO, the experimental validation of the UMO in normal and transient operating conditions and eventually the approval of the French Safety Authority.

Achieving a new fuel qualification is a real challenge. Thus, post irradiation examinations (PIE) of the new fuel element will have to be carried out in order to achieve the qualification process. The PIE will concern irradiated fuel elements parameters of crucial importance:

- **The fuel plates swelling**, i.e. the water channel thickness variations, which is one the most unwanted behavior of dispersed UMO. The impact on reactor safety by lowering the cooling efficiency is obviously dramatic.
- **The aluminum oxide layer** growth on all the fuel plates. Indeed, most research reactors are used aluminum alloys as fuel cladding material, due to its high thermal conductivity and low neutron absorption cross section. Of course, the fuel must operate at low-enough temperatures to be compatible with aluminum. Aluminum alloys undergo oxidation, even at room temperature, if oxygen is available. They produce a protective oxide ( $\text{Al}_2\text{O}_3$ ) of which the growth rate saturates in a short time. The protective oxide, however, degrades in water over time by the formation of various oxide-hydrates at the outer surface, leaving only a thin protective  $\text{Al}_2\text{O}_3$  layer on the aluminum surface [32]. Thus, the formation of oxides on the cladding affects fuel performance by increasing fuel temperature. The most frequently found oxide-hydrates are boehmite ( $\text{Al}_2\text{O}_3 \cdot \text{H}_2\text{O}$ ) and bayerite ( $\text{Al}_2\text{O}_3 \cdot 3\text{H}_2\text{O}$ ) [33]. In the RHF reactor, these (hydr) oxide layers that may grow up to thicknesses of 10-20  $\mu\text{m}$ , have a tremendous impact on the thermal-hydraulic margins. It must thus be characterized with the highest available accuracy for ensuring the best available safety of the RHF facilities.
- The interface between the cladding and the meat, where **fission gas bubbles** may grow and lead to pillowing effects for example.

This thesis will concern the first step: post irradiation examinations of **the fuel plates swelling**.

### VI. Post Irradiation Examination

One of the main conversion prerequisites is the qualification of the new fuels supplied for research reactor core. Fuel performance qualification is limited to the Post Irradiation Examinations (PIE) performed to demonstrate that the new product can be used as a driver fuel in one or more reactors and meets the specified requirements.

In more details, Post Irradiation Examination is the study of nuclear fuel and structural components after irradiation in the reactor. PIE of fuel helps to evaluate performance and analyze failure of reactor operated fuel elements. Moreover, the PIE aims to collect data on various performance parameters such as, swelling, fission gas release and dimensional changes. PIE provides also relevant feedback to the fuel designer, the fuel fabricator and the reactor operator to aim for zero fuel failures and improved fuel performance.

Post Irradiation Examination of the irradiated nuclear fuel is categorized in 3 items:

- **Non-Destructive Techniques (NDT) in hot cell**, such as: visual inspection [34], BONAPARTE measuring bench [35], Gamma spectrometry [36]–[39] and burnup profilometry [14]. With the Non Destructive Examinations (NDE), the fuel plates remain intact.
- **Destructive Techniques (DT) in hot cell**, such as: optical microscopy (OM), scanning electron microscopy (SEM) [40], [41], electron-probe microanalysis (EPMA) [42], [43] and X-ray diffraction [44]–[46]. These destructive examinations need working out on the material, thus they eliminate any return to integrity.
- **Underwater inspection** covers various examination items physically and/or mechanically, such as [47]–[50]:
  - Gamma spectroscopy for the fuel assembly,
  - Visual inspection by a mean of a radiation resistant underwater camera. Video imaging can provide information about the general structural conditions of the fuel and an estimate of breached cladding and exposed fuel meat.
  - Dimensional measurement and geometrical change inspection, etc.

The following sections will describe briefly the most used techniques of the Post irradiation examination: the non-destructive and destructive techniques.

#### 1. Non-Destructive analyses

##### 5.1 Visual inspection in hot-cell

Visual inspection consists in video recording and photographing fuel plates and/or fuel pins in the hot cells, to document their general aspect and the nature or type of damage suffered, namely that caused by irradiation (oxide layer,...). In addition, the visual inspection system is used to check the general conditions of the fuel assembly (physical integrity, fuel metallurgical defects, welding failures...) [34], [51], [52].

### 5.2 BONAPARTE measuring bench

*This section is based on following publications [35].*

The BONAPARTE (Bench fOr Non-destructive Analyses of Plate And Rod Type fuel Elements) measurement bench is installed in a hot cell licensed for accepting both intact and defective fuels (plates and rods). The bench consists of a modular fuel plate clamping system which allows plate rotation (only for curved fuel plates and rods) and a modular measurement head with motorised X- and Y-movement (Y-movement only used for flat fuel plates). Positioning feedback is provided to the stepper motors by a magnetic ruler system based on the Sony Magnescale product line. This allows repeatable positioning of the measurement head to within  $\pm 100 \mu\text{m}$  (68% confidence interval) on a plate (see Figure 12).

The measurement head on the BONAPARTE bench holds probes for plate thickness and oxide thickness measurements. The latter can be performed simultaneously on both sides of the fuel plate. In addition, it can also house a video camera for visual inspection of the plate.

The oxide thickness measurement is based on the eddy current (EC) principle. EC probes measure the distance to a conductive material. When in contact with a material surface, they therefore directly provide a value for the thickness of any non-conductive layer on that surface (e.g. the oxide layer). The probes consist of a ferrite core with an electrical coil surrounding them; with a ceramic top pushed against the measured surface. Calibration is performed using certified Mylar foils or alternatively using a well-characterized oxidized surface of cladding material.

Plate thickness measurements are done using two opposed, customized Sony Magnescale contact probes, whose measurement principle is based on a magnetic ruler. Ceramic thickness reference samples are used to calibrate the probes.

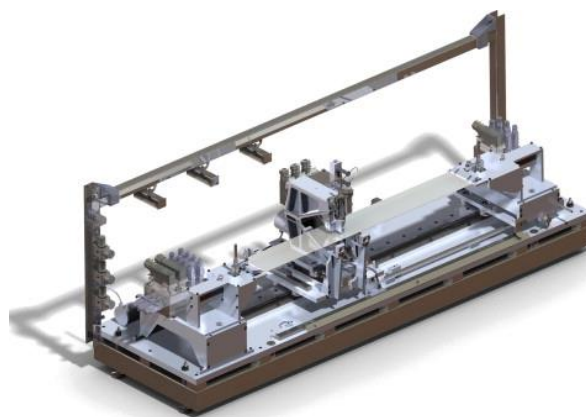


Figure 11: Schematic view of the BONAPARTE measuring bench.

### 5.3 Gamma spectrometry

*This section is based on following publications [36]–[39].*

The fission power of the fuel plates is a basic vital quantity both to judge on the fuel plate behavior and their specification in terms of safeguards.

## Chapter I: Background

---

Quantitative determination of this fission power can be performed by Gamma-spectrometry. This measurement technique has the advantage:

- to be non-destructive, hence to be reversible and applicable at intermediate irradiation stages;
- to be fast;
- to generate at the same time reliable quantitative data on total fuel plate fission power, the fission power profile along the plate, the axial profile of individual radionuclides, hence allowing to recognize fission product migration.

The Gamma spectrometric methodology relies on the sequential measurement, within a fixed collimated geometry, of the fuel plate under examination and a calibration source. From these measurements the absolute concentration of fission products inside the fuel, and hence the fission power, can be obtained.

Two methods of Gamma spectrometry can be employed:

- Distribution of the total activity: it consists in reporting the axial distribution of the total gamma activity emitted by the fuel plate.
- Distribution of the specific activity: opposing to the total activity, this method consists in reporting the axial distribution of a specific nuclide such as Cs or Zr. The gamma spectrometry allows accurate determination of the meat position, size and shape inside the plate by mapping out the  $^{137}\text{Cs}$  distribution.

### 5.4 Burnup profilometry

A model of RHF including detailed axial and radial fuel burn-up distributions in the core has been developed using MCNPX 2.6f and ORIGEN 2.2.VESTA codes [29]. MCNPX is a general-purpose Monte Carlo radiation transport code for modeling the interaction of radiation with everything. MCNPX stands for Monte Carlo N-Particle eXtended [53]. It is also capable of simulating particle interactions of 34 different types of particles (nucleons and ions) and 2000+ heavy ions at nearly all energies. Fuel depletion, actinide transmutation and fission product buildup and decay are calculated using ORIGEN 2.2.

VESTA is a Monte Carlo depletion interface code that is currently under development at IRSN (France). It also offers users a wide array of general modeling features for a complete and detailed description of the irradiation environment. This includes temperature changes, material changes and even geometry changes that for instance allow a user to modify the position of a control rod during an irradiation cycle [54].

The RHF MCNP model has been benchmarked with series of measurements carried out by the ILL and validated in the International Handbook of Evaluated Reactor Physics Benchmark Experiments (IRPhEP), published by the Nuclear Energy Agency (NEA) in 2009.

In this model, all in-pile elements have been taken into account, i.e. all beam tubes, safety rods, cold and hot neutron sources, etc.

### 5.5 Microscopy acoustic

The acoustic microscopy is a non-destructive technique sensitive to variations of mechanical properties of a material. The essential component of the acoustic microscope is a piezoelectric thin film transducer whose thickness depends on the frequencies to be used. It transforms a high frequency electrical signal into an ultrasound wave propagating at the same frequency. The piezoelectric element is located on a small rod of silica that acts as an acoustic

delay line. To focus the acoustic beam a spherical cavity is drilled onto the other face of the rod (see Figure 13). These focused sensors make possible to probe the mechanical properties of very small volumes whose diameter is given by the Rayleigh diffraction. The best performing acoustic microscopes allow now to obtain a resolution of one micron at 1GHz.

High-frequency acoustic waves do not propagate in air and a coupling liquid is necessary to transmit the acoustical signal from the lens to the sample. This fluid plays a fundamental part in the resolution of the acoustic microscope. It is the attenuation in the liquid that determines the highest frequency and the shortest wavelength that can be used, and therefore the best resolution that can be obtained. Water is employed in the majority of applications.

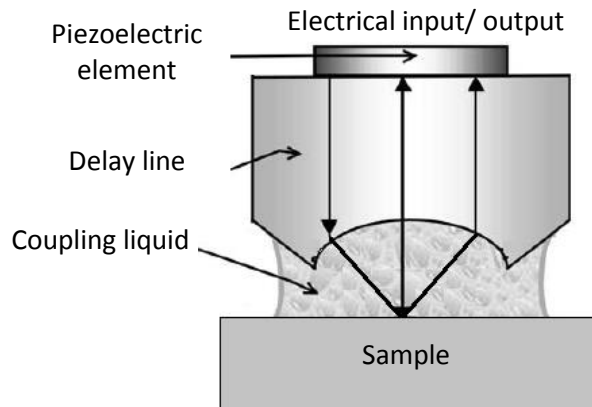


Figure 12: schematic representation the acoustic microscope.

The acoustic microscope can work in two modes: reflection and transmission. In the reflection mode, the acoustic microscope operates with a single transducer for transmitting and receiving the acoustic signal. In transmission, two transducers are symmetrically arranged with respect to the sample to be studied. The object's acoustic image, in a plane parallel to its surface, is called C-scan image. This image is obtained by mechanically scanning the sample in two directions (x-y) perpendicular relative to the transducer. Each pixel of the images corresponds to the amplitude of the reflected beam which is coded according to a gray level scale. When the acoustic wave is focused at the surface of a plane sample, the gray levels correspond to the location of areas with different mechanical properties.

Acoustic image performed in a plane perpendicular to the object surface, is called B-scan image. This image is obtained by moving in a direction to get either a cross section image in X or Y direction. The depth of different structures can be measured [55]–[57].

## 2. Destructive analyses

### 5.6 Optical microscopy (OM)

Optical microscopy gives information about structure morphology like cracks, bubbles or manufacturing porosity, grain geometry (size, distribution spectrum...). Optical microscopy allows magnification up to 1000 with lateral resolution of 1 $\mu$ m.

### 5.7 Scanning electron microscopy (SEM)

The microstructure of fuel plates can be analyzed by Scanning Electron Microscopy (SEM). The SEM uses a focused beam of high-energy electrons to generate a variety of signals at the surface of the sample. The signals that derive from electron-sample interactions

can reveal information about the morphology, the crystalline structure and the orientation of materials, on polish sample or fracture surface. SEM magnification is up to 10.000 with lateral resolution of 0.05 $\mu\text{m}$  [40], [41].

### 5.8 Electron-Probe Microanalysis (EPMA)

The Electron Probe Micro-Analyzer is fundamentally the same as the SEM, with the added capability of chemical analysis. The EPMA is able to give precise quantitative elemental analyses and detailed images of a very small sample. It also allows much higher resolution images to be obtained than can be seen using visible-light optics. Therefore, features that are irresolvable under a light microscope can be readily imaged to study detailed micro-textures.

### 5.9 X-ray diffraction

X-ray diffraction (XRD) is a rapid analytical technique primarily used for phase identification of a crystalline material and can provide lattice parameter determination and micro distortion detection. These X-rays are generated by a cathode ray tube, filtered to produce monochromatic radiation, collimated to concentrate, and directed toward the sample. The interaction of the incident rays with the sample produces constructive interference (and a diffracted ray) when conditions satisfy Bragg's Law ( $n\lambda=2d \sin \theta$ ). These diffracted X-rays are then detected, processed and counted. By scanning the sample through a range of  $2\theta$  angles with a horizontal theta/theta goniometer setup, all possible diffraction directions of the lattice should be attained. A 500  $\mu\text{m}$  beam size can be achievable for local data collection [44]–[46].

**Note:** To summarize, the use of non-destructive and destructive techniques is often necessary to study detailed aspects of fuel performance. However, such off-site remote handling facilities and techniques are expensive and limited in throughput, and can involve considerable delay. An alternative technique, which is economic and allowing the assessment of the fuel plate swelling was and still developed. This technique is determined through the inter-plate distance measurement.

## VII. Distance measurement techniques

In the framework of the conversion study of the RHF into Low Enriched Uranium, the ILL launched a study aiming to the development of tools allowing the evaluation of the fuel plates swelling, i.e. the water channel thickness variations. This parameter, here determined through the inter-plate distance measurement, is rich of information especially regarding the element irradiation history. Distance measurement techniques which can be non-destructive and remotely operated, have advantages relative to conventional PIE, by:

- increasing of feedback on irradiated fuel plates,
- allowing the inspection of the 280 fuel plates if necessary.
- shortening of the cooling time needed before usual ND PIE,
- considerably reducing the cost than the PIE.

However, this identification is difficult because a micrometer resolution is sought due to the microscopic structure modifications of the plates while the inter-plate distance is close to two millimeters. Furthermore, the access to the involute curved fuel plates situated five meters

below the surface of the moderating pool is very difficult and the measurement devices will be subjected to high-level radiations.

Therefore, several methods could be considered to perform distance measurements. Optical, magnetic, capacitive, ultrasonic, or other (micro-waves sensor, tunneling sensors...). The following sections describe briefly these methods.

## 1. Optical measurement

Optical distance measurement methods can technically be put into three categories: interferometry, time-of-flight and triangulation methods. Reviews of absolute distance measurement can be found in [58].

- **Triangulation** [59], [60]:

Distance measurements using triangulation principle are typically based on eye safe lasers. The laser projects a laser spot in front of the sensor to the point that the sensor will measure the distance. A camera is mounted so it images the laser spot. Depending on the distance to the spot, the angle  $\theta$  between the camera and the laser spot will change due to triangulation. The triangulation principle is sketched in Figure 13. The distance can be calculated as:

$$Distance = \frac{L}{\tan(\theta)}. \quad (1)$$

The laser spot can only be measured with a finite angular accuracy due to laser spot centroiding limitations, noise, mechanical stability, target homogeneity, speckles etc. Therefore, the uncertainty on the measured distance increases with the distance, as shown in the equation below. Typically, it is very difficult to get any useful distance information at distances larger than 100 times the laser-camera baseline (L).

$$\Delta Distance = \left[ \frac{L}{\tan(\theta)} - \frac{L}{\tan(\theta + \Delta angle)} \right]. \quad (2)$$

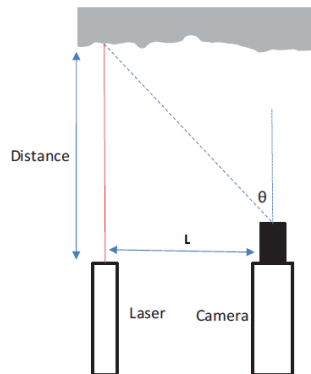


Figure 13: Distance measurement utilizing triangulation.

- **Interferometers**[61]:

Interferometry can be implemented either by using a high coherence light source (i.e laser) and the object should be mirror or by using a broad-band or low-coherence light source (i.e. lamp, LED, SLD, etc.). A great advantage of low-coherence light interferometer is that it can be used to measure objects with rough surface.

The basic idea for measuring distances with high-coherence interferometric is to feed an interferometer with two or more optical wavelengths to produce a synthetic or equivalent

wavelength, much longer than that of the original beams. The distance measurement is extracted by gauging the phase of a signal having a period equal to that of the equivalent wavelength. The most effective approaches are based on double-heterodyne interferometry (DHI) [62] that makes use of a detection scheme based on optical heterodyning of two slightly different optical frequencies.

As an alternative to multiple wavelength interferometry, techniques based on optical frequency modulation of the laser source are very promising due to the potential for simple and robust systems [63]. Among the various possibilities, frequency-modulated continuous wave interferometry (FMCW) presents the simplest optical layout which is essentially based on a Michelson-type (see figure 14) interferometer where a tunable single frequency laser is modulated to obtain a beat signal at the photodetector.

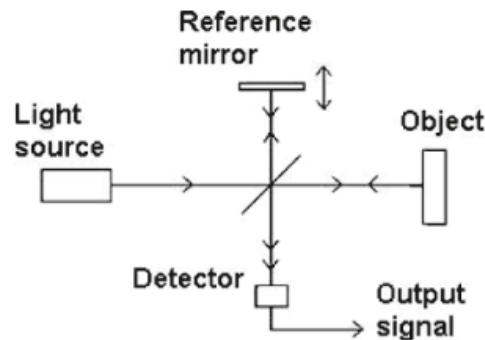


Figure 14: Michelson interferometer.

Absolute distance measurements can also be performed on the basis of low-coherence or white light interferometry (WLI). In this case the measuring range is shorter than that of DHI or FMCW while the resolution can be better than  $\lambda$ . Possible light sources for WLI are: lamps, LEDs, super-luminescent diodes (SLD) and multi-mode laser diodes. The most popular, compact and reliable solid-state sources for WLI are SLDs. In WLI systems, the measurement resolution is practically related only to the coherence characteristics of the excitation light.

- **Time-of-flight (TOF) method**

Time-of-flight method can be realized by many different methods. Mostly used principles are: phase shift method, and pulsed TOF method.

- Phase shift or phase difference method [64] is a common technology for surveying. It allows the measurement of distances as depicted in figure 15.

A sinusoidally modulated laser beam is sent to a target, usually a reflector, e.g., a corner cube. Reflected light (from diffuse or specular reflections) is detected, and the phase of the power modulation is compared with that of the sent light. The obtained phase shift is  $2\pi$  times the time-of-flight ( $2L/c$ ) times the modulation frequency ( $f$ ). If the total phase shift ( $\Delta\phi$ ) is inside one cycle, it leads to a distance as follows:

$$Distance = \frac{\Delta\phi \times c}{4\pi f}. \quad (3)$$

Distance measurement by the phase-shift technique is a good method to obtain a resolution of some millimeters in the 1 to 20 m ranges with non-cooperative targets. For cooperative targets (cube corner), the resolution can be better than  $50 \mu\text{m}$ , with high-frequency modulation.

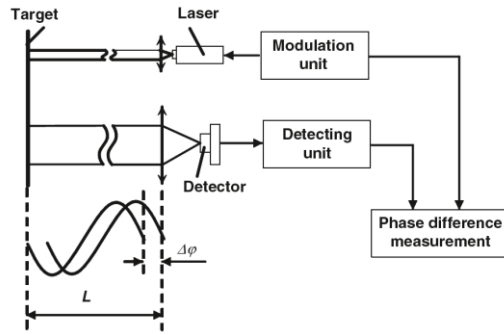


**Figure 15: Phase-shift method for distance measurement.**

- The Pulse time-of-flight (TOF) [65] refers to the time it takes for a pulse of energy to travel from its transmitter to an observed object and then back to the receiver ( $t$ ). If light is used as energy source, the relevant parameter involved in range counting is the speed of light (roughly  $c=30$  cm/ns). A TOF system measures the round trip time between a light pulse emission and the return of the pulse echo resulting from its reflectance off an object. Using elementary physics, distance is determined by multiplying the velocity ( $c$ ) of light by the time ( $t$ ) light takes to travel the distance. In this case, the measured time is representative of traveling twice the distance and must, therefore, be reduced by half to give the actual range to the target. To obtain a 1 mm accuracy, the accuracy of the time interval measurement should be 6.7 ps.

$$Distance = \frac{t \times c}{2}. \tag{4}$$

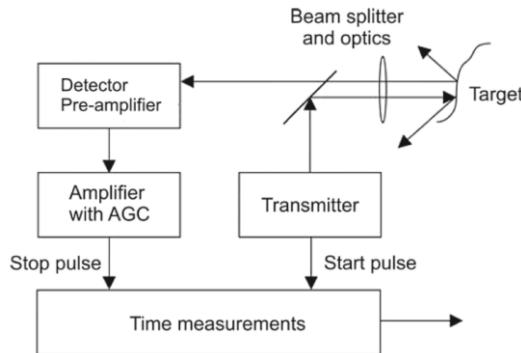


**Figure 16: Block diagram of TOF distance measurement.**

**Note:** Optical techniques are available for both geometry and profile measurements. They provide high accuracy measurements (due to the use of short wavelengths) and possess a low sensitivity to environmental conditions such as pressure and temperature. However, their drawbacks are size (may not be integrated into the RHF fuel element where space is very limited, 1.8 mm nominal), alignment complications (particularly in a high vibration environment) and the random effects of debris in the optical path. Moreover, systems cannot be immersed in water.

## 2. Capacitive measurement

*This section is based on following publications [66]–[68].*

Capacitive sensors are used to make non-contact measurements with high precision and high bandwidth as well optical sensors.

Capacitive sensors consist of two parallel metal plates in which the dielectric between the plates is either air or some other medium. The capacitance  $C$  is given by  $C = \epsilon_0 \epsilon_r A / d$ , where  $\epsilon_0$  is the absolute permittivity,  $\epsilon_r$  is the relative permittivity of the dielectric medium between the plates,  $A$  is the area of the plates and  $d$  is the distance between them. There are two general types of capacitive sensing systems. One type is used to measure thicknesses of conductive materials. The other type measures thicknesses of non-conductive materials.

The thicknesses of a conductive material can be performed by a capacitive sensing system, if one electrode is a sensor plate and the other is a target plate. The distance  $d$  will be determined by measuring capacitance  $C$ . Since the area of the probe and target remain constant, and the dielectric of the material in the gap (usually air) also remains constant, "any change in capacitance is a result of a change in the distance between the probe and the target.". Therefore, the equation above can be simplified to:

$$C \propto \frac{1}{d}. \quad (5)$$

From this equation, a capacitive sensing system is able to measure changes in capacitance and translate these changes into distance measurements. There are two methods of capacitive, noncontact thickness measurement of a conductive target: Single Channel (Figure 17), and Dual-Channel (Figure 18):

- **Single-Channel Thickness Measurement Method :**

Single-channel thickness measurements measure the location of the top surface of the part under test while it rests on a reference surface. A known thickness is established as a reference point and all subsequent measurements indicate the amount of deviation from that reference. However, any deformity of the part or the reference surface will result in an error in the thickness measurement.

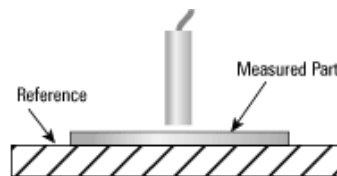


Figure 17: Single-channel system.

- **Dual-Channel Thickness Measurement Method:**

Dual-channel thickness measurements place the part to be measured between two sensors. Each side of the part is measured by a separate sensor. The sum of the measurements from the two sensors provides the final measurement of thickness. If the part moves toward one sensor, it moves away from the other; the changes in the sensors outputs will cancel each other. This eliminates the errors that would result from single-channel problems with deformity and/or contact with the reference surface. As with many noncontact applications, measurements are relative to a reference measurement. A known thickness is established as a reference point and all subsequent measurements indicate the amount of deviation from that reference.

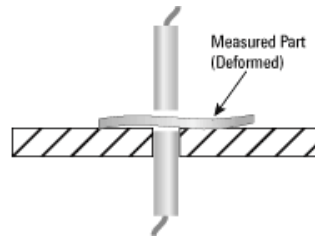


Figure 18: Dual-channel system.

Capacitive sensors are sensitive to nonconductive materials which are placed between the probe's sensing area and a grounded back target. If the gap between the sensor and the back target is stable, changes in the sensor output are indicative of changes in thickness, density, or composition of the material in the gap (see Figure 19).

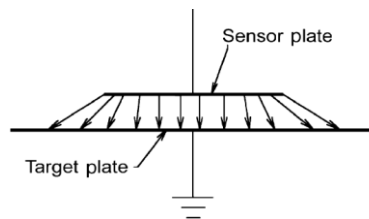


Figure 19: Measuring Non-Conductors thickness.

**Note:** By capacitive sensors, that may be compact, resolutions lower than one micron can be obtained for distances ranging from  $0.1\mu\text{m}$  to 5 mm [66]. However, environmental factors such as temperature, pressure, humidity and radiations affect the dielectric constant of a capacitor and therefore these effects severely deteriorate the precision of thickness measurement [69]. Because of their low signal-to-noise ratio, the capacitive sensors cable length is also restricted.

### 3. Magnetic measurement

Magnetic sensors utilize the magnetic phenomena of inductance, reluctance and eddy currents to indicate the value of various measurements, including displacement, distance, thickness, deformation, and so on.

- **Proximity inductive sensor**

In a simple proximity sensor the device is supplied with electrical power, which causes an alternating current to flow in a coil wrapped on a ferromagnetic body (sometimes referred to as a loop, spool or winding), creating thus a magnetic field. When a conductive or magnetically permeable target, such as a steel disk, approaches the coil, this modifies the properties of the field created by the coil and consequently the value of the coil's impedance. When a threshold is passed, this acts as a signal that the target is present. Proximity sensors are commonly used to detect the presence or absence of a metal target [70]–[73]. The inductance principle is also used in differential transformers to measure translational and rotational displacements. One example of the inductive sensor is shown in Figure 21.

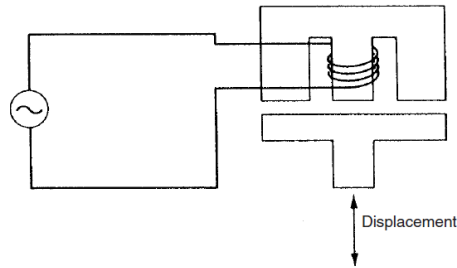


Figure 20: Inductive sensor [67].

- **Eddy-current sensor**

Eddy-Current sensors are noncontact devices capable of high-resolution measurement (up to  $0.1\ \mu\text{m}$ ) in a range of technological applications such as thickness measurement, quality inspection, coating and surface treatment [74]–[77].

The eddy-current sensor is based on the principle that, if an oscillator circuit induces an eddy current in an electrically conductive target, the circuit itself will lose energy. If a coil built into the sensor is fed with a high-frequency alternating current when the sensor is positioned close to a metal target, the electromagnetic field of the coil will create eddy currents in the target. The field created by this eddy current, in turn, opposes the electromagnetic field of the coil in the sensor. This interaction of the magnetic fields is dependent on the distance between the probe and the target. As the distance changes, the electronics sense the change in the field interaction and produce a voltage output which is proportional to the change in distance between the probe and target. The target surface must be at least three times larger than the probe diameter for normal, calibrated operation; otherwise, special calibration may be required [78].

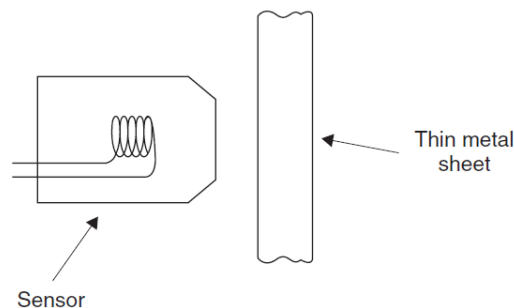


Figure 21: Eddy current sensor [67].

**Note:** In comparison to optical and capacitive technologies the biggest advantage of magnetic sensors is the immunity against oil, water and dirt. However, electrical runout (inhomogeneity) can disturb the propagation of the eddy currents and thus can affect the transducer output, which in turn results in noise and degraded resolution. Moreover, serious perturbations of these magnetic systems can happen in highly radiative environments.

#### 4. Ultrasonic measurement

The accurate estimation of distance through ultrasonic measurements is fundamental to a wide variety of engineering fields, such as medical imaging, robotic, non-destructive control system and so on [79]–[81]. Generally speaking, ultrasonic techniques, which are typically

inexpensive, yield high levels of performance and are radiation resistant. Sensors can be sealed to be immersed, and finally can be designed to reach the expected dimensions.

The most common form of ultrasonic transducers is a piezoelectric crystal. Such elements can operate interchangeably as either a transmitter or receiver. These are available with operating frequencies that vary between 20 kHz and 2 GHz (more details in the next chapter). The principles of operation, by which an alternating voltage generates an ultrasonic wave and vice versa, will be covered in the following subsection.

The basic method of ultrasonic distance sensors is using an acoustic signal, which is sent from a transmitter and travels through the propagation medium to a receiver (see Figure 23). The distance between the transmitter and receiver is obtained by counting the elapsed time from the start of the transmission to the end of the receipt, defined as the time-of-flight (TOF) [82]. Depending on the specific application, different methods of ultrasonic distance measurement can be used, among them, the phase shift method (PSM) and the pulse echo technique (more details in the following sections).

## 4.1 Time-of-flight measurement and estimation

- **Phase shift method**

In continuous phase shift method, the transmitter generates a continuous output, whose echo is detected by a separate receiver (see Figure 23). The measurements accuracy depends on the measurement of phase shift between the transmitted and reflected wave [83].

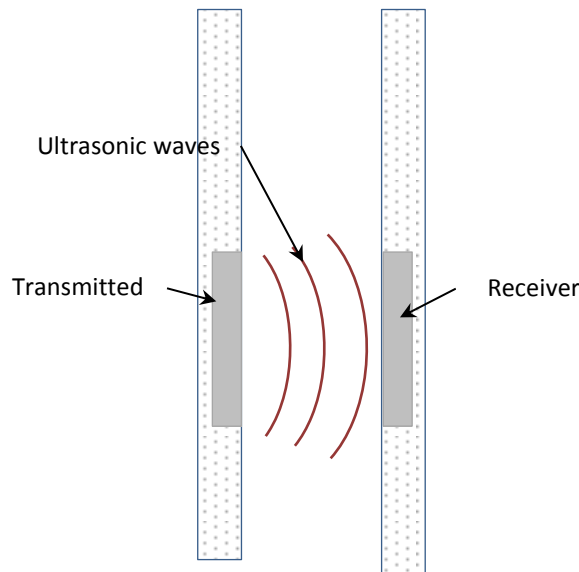


Figure 22: Block diagram of the phase shift method.

Although more accurate than the pulse-echo measurements, this technique is more expensive due to often complex hardware needed to measure the phase. Moreover, in most cases, different frequencies are needed to be used in order to determine the number of integer wavelengths in the phase shift [83]. Due to its experimental configuration (two transducers positioned face to face, one acting as a transmitter and the second as a receiver), the phase shift method cannot be implemented inside the RHF water channel to measure its width [84]–[86].

- **Pulse echo method:**

The general method for a pulsed method of ultrasonic distance measurement is as follows. An ultrasonic pulse is transmitted from one ultrasonic transducer. The pulse propagates through the medium and is reflected by a suitable reflector. The pulse returns and is received by the transducer (see Figure 24). The time ( $t$ ) taken for the pulse to propagate from its emission to its reception is proportional to the measurement distance ( $d$ ) and the speed of sound in the medium ( $c$ ) through the simple equation [83], [87], [88]:

$$d = \frac{t \times c}{2} \quad (7)$$

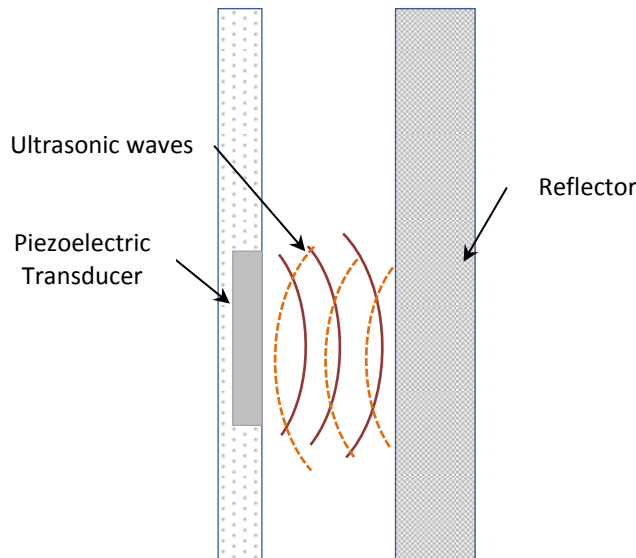


**Figure 23: Block diagram of the pulse echo method.**

There are a multitude of different methods for measuring the TOF of an acoustic signal (Threshold Detection, curve-fitting method, cross-correlation method...).

- *Threshold Detection:*

The simplest form of measurement of the TOF is the threshold method. This technique involves detecting the arrival of an acoustic signal when its amplitude exceeds a given amplitude level. Thresholding systems do not require any complex computations, but they suffer from poor resolution, low signal-to-noise ratio (SNR), and inherent bias, particularly when the received signal has been greatly attenuated. The first problem is, in fact, affected by the propagating medium, the attenuation of which increases with the frequency. Moreover, the signal-to-noise ratio (SNR) is altered by the absorption of the target, external vibrations, and water turbulence. Finally, there are two causes for an inherent bias to longer delays. First, no matter how ideal is the emitted pulse from the transducer, there will always be a rise time for the signal when it is detected. Second, and more importantly, the decision of where to set the threshold is a compromise that introduces bias [89], [90].

- *curve-fitting method*

An alternative method is the curve fitting method which produces an unbiased TOF measurement. In this technique, a nonlinear least-squares method is employed to fit a curve to the onset of the ultrasonic of the received acoustic. A parabolic curve of the form  $a_0(t - t_0)^2$  is fitted to the signal envelope around the rising edge of the echo. It has been verified in [91] and

[92] that this is a good approximation. First, initial estimates of the two parameters  $a_0$  and  $t_0$  are obtained: the initial estimate for  $t_0$  is found by simple thresholding, and  $a_0$  is estimated from the second derivative approximation around the threshold point [93].

- *Cross-correlation method*

An optimum TOF estimation technique is the cross-correlation method. By computing the cross-correlation between the transmitted and the received signal, the TOF can be estimated when the correlation result reaches its maximum. The cross-correlation is arguably more performant both in terms of random noise (theoretically zero) and time resolution than the two methods mentioned above. The method of cross-correlation takes a transmitted (transmitted signal  $x(t)$ ) and received signal (received signal  $y(t) \sim x(t-\tau)$ ) and then produces a time-domain signal whose maximum occurs at the delay time  $\tau_0$ .

The cross correlation  $R_{xy}(t)$  of the sequences  $x(t)$  and  $y(t)$  is defined by the following equation:

$$R_{xy}(t) = x(t) \otimes y(t) = \int_{-\infty}^{\infty} x(\tau) \cdot y(t + \tau) dt$$

where the symbol  $\otimes$  denotes correlation [94]–[97].

### 4.2 Measurement resolution and accuracy

The best measurement resolution that can be obtained with an ultrasonic system is equal to the wavelength of the transmitted wave. As wavelength is inversely proportional to frequency, high-frequency ultrasonic elements would seem to be preferable. For example, the resolution of measurements performed in water at room temperature (20°C), is only 10  $\mu\text{m}$  for a 150 MHz element. However, choice of element also depends on the required range of measurement. The range of higher-frequency elements is much reduced compared with low-frequency ones due to the greater attenuation of the ultrasound wave as it travels away from the transmitter. Hence, choice of element frequency has to be a compromise between measurement resolution and range.

The best measurement accuracy obtainable is equal to the measurement resolution value, but this is only achieved if the electronic counter used to measure the transmission time starts and stops at exactly the same point in the ultrasound cycle (usually the point in the cycle corresponding to peak amplitude is used) [67].

#### **Note:**

To perform distance measurements between fuel plates spaced of 1.8 mm, 5 m underwater, and in highly radiative environments, the most relevant solution was to develop a waterproof double side high-frequency ultrasonic device. This device includes transducers designed to be set on both side of a blade with the constraint of 1 mm total device thickness. Adapted to the high radiative environment and thin enough, the device make possible the measure of the fuel plates swelling, i.e. the water channel thickness variations, of High Performance Research Reactor spent fuel elements. Operating at frequencies up to 150 MHz, the measurement resolution that can be obtained with the ultrasonic device can reach 10  $\mu\text{m}$ . Based on the pulse-echo method, the ultrasonic sensor allows distance measurements through the evaluation of the ultrasonic wave time of flight (ToF). The ToF estimation is computed from the cross-correlation between the transmitted and received signal (more details in the second chapter).

### VIII. Conclusion

The Institute Laue-Langevin (ILL) committed for decades to convert its reactor, the RHF (Réacteur à Haut Flux) into a Low Enriched Uranium (LEU) high density fuel. Now deeply engaged in the conversion process, the ILL has designed an optimized LEU fuel element, which is based upon the high density LEU fuel (UMo) being qualified by the HERACLES group. In the framework of the conversion study, the ILL launched a study aiming to develop of tools allowing the assessment of the fuel plate swelling, which is one the most unwanted behavior of dispersed UMo. Post irradiation examinations (PIE) of the new fuel element will have to be carried out in order to achieve the qualification process. However, PIE techniques (destructive and non-destructive), which require an off-site remote handling facility, are expensive and can involve considerable delay.

As an alternative solution, the fuel plates swelling can be identified through the inter-plate distance measurement. This identification is difficult because of a micrometer resolution is sought due to the microscopic structure modifications of the plates while the inter-plate distance is close to two millimeters. Furthermore, the access to the involute curved fuel plates situated five meters below the surface of the moderating pool is very difficult and the measurement devices will be subjected to high-level radiations.

Several methods could be considered to perform distance measurements. Optical, magnetic, or capacitive devices might be relevant and reach the nanometer resolution even in high-temperature and/or high-pressure environments. However, they may not be inserted between the fuel plates where space is very limited or may not meet the requirement for high radiation. Some of them cannot even be immersed.

To address this issue, a high frequency ultrasonic device based on the pulse echo method was studied, designed, then developed and finally tested with success on a full size irradiated fuel element of the Institute Laue Langevin reactor, the RHF.

## List of Figures

Figure 1: ILL high flux reactor .....	17
Figure 2: Schematic overview of the fuel plate production procedure .....	18
Figure 3: The fuel element .....	19
Figure 4: The fuel plates.....	19
Figure 5: Top view of the fuel plate dimensions (in cm) .....	19
Figure 6: Monolithic fuel [19].....	20
Figure 7: UMo dispersion fuel[19].....	20
Figure 8: Interaction layer [16]. .....	22
Figure 9: Fission products [22]. .....	22
Figure 11: Scheme of HEU plates, LEU plates as studied in a first step and TOUTATIS LEU plates. The last figure illustrates the boron location which is set above the fuel plate in the outer tube of the element. ....	24
Figure 12: Schematic view of the BONAPARTE measuring bench. ....	26
Figure 13: schematic representation the acoustic microscope.....	28
Figure 14: Distance measurement utilizing triangulation. ....	30
Figure 15: Michelson interferometer. ....	31
Figure 16: Phase-shift method for distance measurement. ....	32
Figure 17: Block diagram of TOF distance measurement. ....	32
Figure 18: Single-channel system.....	33
Figure 19: Dual-channel system. ....	34
Figure 20: Measuring Non-Conductors thickness. ....	34
Figure 21: Inductive sensor [67]. ....	35
Figure 22: Eddy current sensor [67]. ....	35
Figure 23: Block diagram of the phase shift method.....	36
Figure 24: Block diagram of the pulse echo method. ....	37

### Reference

- [1] A. Travelli, « U.S. reduced enrichment research and test reactor (RERTR) program: accomplishments, plans, and schedules », 1980.
- [2] Office of Nuclear Reactor Regulation, NUREG-1313 (1988) .
- [3] A. Travelli, « Progress of the RERTR Program in 1999 », in *Proceedings of the XXII International Meeting on Reduced Enrichment for Research and Test Reactors, Budapest, Hungary*, 1999, p. 3–8.
- [4] A. Travelli, « The RERTR program: a status report », in *International Meeting on Reduced Enrichment for Research and Test Reactors*, 1998.
- [5] Ryu, H. J., Y. S. Kim, J. M. Park, H. T. Chae, C. K. and Kim, 2008, “Performance Evaluation of U-Mo/Al Dispersion Fuel by Considering a Fuel-Matrix Interaction”, *Nuclear Engineering and Design*, Vol. 40, No. 5, p. 409–418 .
- [6] K. I. M. Kihwan, L. E. E. Don Bae, K. I. M. Chang Kyu, I. H. KUK, et K. W. BAEK, « DEVELOPMENT OF URANIUM-SILICIDE AND U-Mo XA9745724 ALLOY FUELS BY CENTRIFUGAL ATOMIZATION », *Stud. Fuels Low Fission Gas Release*, p. 77, 1997.
- [7] S. Van den Berghe, W. Van Renterghem, et A. Leenaers, « Transmission electron microscopy investigation of irradiated U-7wt%Mo dispersion fuel », *J. Nucl. Mater.*, vol. 375, n° 3, p. 340-346, avr. 2008.
- [8] J. Gan, D. D. Keiser, D. M. Wachs, B. D. Miller, et T. R. Allen, « Characterization of RERTR Fuel », 2008.
- [9] A. Begeron, A. Tentner, and J.G Stevens, « Feasibility Analyses for HEU to LEU Fuel Conversion of the Laue Langevin Institute (ILL) High Flux Reactor (RHF) », Nuclear Engineering Division, Argonne National Laboratory (2010).
- [10] « HFIR | High Flux Isotope Reactor | ORNL ». [En ligne]. Disponible sur: <http://www.ornl.gov/user-facilities/hfir>. [Consulté le: 24-août-2015].
- [11] « Neutrons For Science - Annual Report 2014 ». [En ligne]. Disponible sur: [https://www.ill.eu/fileadmin/users\\_files/Annual\\_Report/AR-14/mobile/index.html](https://www.ill.eu/fileadmin/users_files/Annual_Report/AR-14/mobile/index.html). [Consulté le: 11-juin-2015].
- [12] S. Van den Berghe, A. Leenaers, E. Koonen, et L. Sannen, « From High to Low Enriched Uranium Fuel in Research Reactors », *Adv. Sci. Technol.*, vol. 73, p. 78-90, oct. 2010.
- [13] A. Leenaers, « Surface-engineered low-enriched Uranium-Molybdenum fuel for research reactors. », University of Ghent, 2014.
- [14] J. M. Beeston, R. R. Hobbins, G. W. Gibson, et W. C. Francis\*, « Development and Irradiation Performance of Uranium Aluminide Fuels in Test Reactors », *Nucl. Technol.*, vol. 49, no 1, p. 136-149, juin 1980.
- [15] U. S. C. on P. Challenges, and Opportunities for Converting U. S. and Russian Reactors from Highly Enriched to Low Enriched Uranium Fuel, N. and R. S. Board, D. on E. and L. Studies, et N. R. Council, *Progress, Challenges, and Opportunities for Converting U.S. and Russian Research Reactors:: A Workshop*. National Academies Press, 2012.
- [16] W. Dienst, S. Nazaré, et F. Thümmeler, « Irradiation behaviour of UAlx-Al dispersion fuels for thermal high flux reactors », *J. Nucl. Mater.*, vol. 64, n° 1-2, p. 1-13, janv. 1977.
- [17] K. H. Kim, D. B. Lee, C. K. Kim, G. L. Hofman, et K. W. Paik, « Thermal compatibility of centrifugally atomized U-Mo powders with aluminium in a dispersion fuel », *Nucl. Eng. Des.*, vol. 178, n° 1, p. 111-117, déc. 1997.

## Chapter I: Background

---

- [18] M. K. Meyer, J. Gan, J. F. Jue, D. D. Keiser, E. Perez, A. Robinson, D. M. Wachs, N. Woolstenhulme, G. L. Hofman, et Y. S. Kim, « IRRADIATION PERFORMANCE OF U-Mo MONOLITHIC FUEL », *Nucl. Eng. Technol.*, vol. 46, n° 2, p. 169-182, avr. 2014.
- [20] A. YACOUT « INTERNATIONAL LOW ENRICHED URANIUM FUEL DEVELOPMENT AND NNSA/M3 ROLE », PRESENTATION TO THE NATIONAL ACADEMY OF SCIENCE, PANEL APRIL 16, 2015.
- [20] J. Gan, D. D. Keiser Jr., D. M. Wachs, A. B. Robinson, B. D. Miller, et T. R. Allen, « Transmission electron microscopy characterization of irradiated U-7Mo/Al-2Si dispersion fuel », *J. Nucl. Mater.*, vol. 396, n° 2-3, p. 234-239, janv. 2010.
- [21] D. L. Porter et A. Ewh, « Interaction Layer Characteristics in U-xMo Dispersion/Monolithic Fuels », Idaho National Laboratory (United States). Funding organisation: DOE-NA (United States), 2010.
- [22] A. Leenaers, S. Van den Berghe, W. Van Renterghem, F. Charollais, P. Lemoine, C. Jarousse, A. Röhrmoser, et W. Petry, « Irradiation behavior of ground U(Mo) fuel with and without Si added to the matrix », *J. Nucl. Mater.*, vol. 412, n° 1, p. 41-52, mai 2011.
- [23] Y. S. Kim et G. L. Hofman, « Fission product induced swelling of U-Mo alloy fuel », *J. Nucl. Mater.*, vol. 419, n° 1-3, p. 291-301, déc. 2011.
- [24] Y. S. Kim, G. L. Hofman, et J. S. Cheon, « Recrystallization and fission-gas-bubble swelling of U-Mo fuel », *J. Nucl. Mater.*, vol. 436, n° 1-3, p. 14-22, mai 2013.
- [25] A. Leenaers, S. Van den Berghe, E. Koonen, C. Jarousse, F. Huet, M. Trotabas, M. Boyard, S. Guillot, L. Sannen, et M. Verwerft, « Post-irradiation examination of uranium-7 wt% molybdenum atomized dispersion fuel », *J. Nucl. Mater.*, vol. 335, n° 1, p. 39-47, oct. 2004.
- [26] L. T. Liu Xiao, « Modeling the swelling performance of UMo alloys for Al-matrix dispersion fuel », *J. Alloys Compd. - J ALLOYS Compd.*, vol. 509, n° 23, p. 6589-6594, 2011.
- [27] D. M. Dowling, R. J. White, et M. O. Tucker, « The effect of irradiation-induced resolution on fission gas release », *J. Nucl. Mater.*, vol. 110, n° 1, p. 37-46, 1982.
- [28] T. A. J. Stevens, « Feasibility analyses for HEU to LEU fuel conversion of the LAUE Langvin Institute (ILL) High Flux Reactor (RHF) », Argonne National Laboratory (ANL), 2010.
- [29] Y. Calzavara, F. Frery, F. Thomas, H. Guyon, A. Bergeron, A. Tentner, J. Stevens, et W. Haec, « TOUTATIS: ILL CONVERSION FEASIBILITY STUDY ». 32nd INTERNATIONAL MEETING ON REDUCED ENRICHMENT FOR RESEARCH AND TEST REACTORS (RERTR), Portugal, 2010.
- [31] A. TENTNER et al. « Thermal-Hydraulic safety analyses for conversion of the Laue Langevin Institute (ILL) High Flux Reactor (RHF) from HEU to LEU fuel » XXXII RERTR International meeting, 2010.
- [31] H. Breitschütz, R. Jungwirth, A. Röhrmoser, W. Petry, D. Berghe, S. Van, A. Leenaers, A. Koonen, P. Lemoine, M. Ripert, H. Palancher, M. C. Anselmet, C. Jarousse, B. Stepnik, D. Geslin, Y. Calzavara, et H. Guyon, « The development of dispersed UMO as a high performance research reactor fuel in Europe », 2013.
- [32] G. L. H. Yeon Soo Kim, « Oxidation of aluminum alloy cladding for research and test reactor fuel », *J. Nucl. Mater.*, vol. 378, n° 2, p. 220-228, 2008.
- [33] A. Leenaers, E. Koonen, Y. Parthoens, P. Lemoine, et S. Van den Berghe, « Post-irradiation examination of AlFeNi clad U3Si2 fuel plates irradiated under severe conditions », *J. Nucl. Mater.*, vol. 375, n° 2, p. 243-251, avr. 2008.
- [34] S. Van den Berghe, Y. Parthoens, G. Cornelis, A. Leenaers, E. Koonen, V. Kuzminov, et C. Detavernier, « Swelling of U(Mo) dispersion fuel under irradiation – Non-

- destructive analyses of the SELENIUM plates », *J. Nucl. Mater.*, vol. 442, n° 1-3, p. 60-68, nov. 2013.
- [35] S. Van den Berghe, Y. Parthoens, F. Charollais, Y. S. Kim, A. Leenaers, E. Koonen, V. Kuzminov, P. Lemoine, C. Jarousse, H. Guyon, D. Wachs, D. Keiser Jr, A. Robinson, J. Stevens, et G. Hofman, « Swelling of U(Mo)–Al(Si) dispersion fuel under irradiation – Non-destructive analyses of the LEONIDAS E-FUTURE plates », *J. Nucl. Mater.*, vol. 430, n° 1-3, p. 246-258, nov. 2012.
- [36] A. Alghem, M. Kadouma, et R. Benaddad, « NDT as a tool, for Post-Irradiation Examination. », in *Abstracts of 17th World Conference on Non-Destructive Testing*, 2008.
- [37] L. Sannen, L. Borms, C. de Raedt, et A. Gys, « Gamma-spectrometric determination of the fission power of fuel rods », Proceeding of a Technical Committee meeting held in Dimitrovgrad, Russian Federation, 2001.
- [38] H. Seo, J.-M. Oh, H.-S. Shin, H. Kim, S. K. Lee, H. S. Lee, et S.-H. Park, « Burnup Measurement of Spent Fuel Assembly by CZT-based Gamma-Ray Spectroscopy for Input Nuclear Material Accountability of Pyroprocessing », *IEEE Trans. Nucl. Sci.*, vol. 61, n° 4, p. 2169-2174, août 2014.
- [39] L. W. Campbell, L. E. Smith, et A. C. Misner, « High-Energy Delayed Gamma Spectroscopy for Spent Nuclear Fuel Assay », *IEEE Trans. Nucl. Sci.*, vol. 58, n° 1, p. 231-240, févr. 2011.
- [41] Reed, S. J. B., 2005, *Electron Microprobe Analysis and Scanning Electron Microscopy in Geology*, Cambridge University Press, 2005.
- [41] A. Leenaers, S. Van den Berghe, J. Van Eyken, E. Koonen, F. Charollais, P. Lemoine, Y. Calzavara, H. Guyon, C. Jarousse, D. Geslin, D. Wachs, D. Keiser, A. Robinson, G. Hofman, et Y. S. Kim, « Microstructural evolution of U(Mo)–Al(Si) dispersion fuel under irradiation – Destructive analyses of the LEONIDAS E-FUTURE plates », *J. Nucl. Mater.*, vol. 441, n° 1-3, p. 439-448, oct. 2013.
- [42] « Electron probe micro-analyzer (EPMA) », *Techniques*. [En ligne]. Disponible sur: [http://serc.carleton.edu/research\\_education/geochemsheets/techniques/EPMA.html](http://serc.carleton.edu/research_education/geochemsheets/techniques/EPMA.html). [Consulté le: 27-août-2015].
- [43] B. T. Bradbury, J. T. Demant, P. M. Martin, et D. M. Poole, « Electron probe micro-analysis of irradiated UO<sub>2</sub> », *J. Nucl. Mater.*, vol. 17, n° 3, p. 227-236, nov. 1965.
- [44] « X-ray Powder Diffraction (XRD) », *Techniques*. [En ligne]. Disponible sur: [http://serc.carleton.edu/research\\_education/geochemsheets/techniques/XRD.html](http://serc.carleton.edu/research_education/geochemsheets/techniques/XRD.html). [Consulté le: 27-août-2015].
- [45] T. Roth, C. Detlefs, I. Snigireva, et A. Snigirev, « X-ray diffraction microscopy based on refractive optics », *Opt. Commun.*, vol. 340, p. 33-38, avr. 2015.
- [46] R. James, « X-ray Diffraction », 2014.
- [47] D. F. Sears, K. T. Conlon, J. Mason, A. Davidson, et C. Buchanan, « Post-irradiation examination of uranium-molybdenum dispersion fuel irradiated to high burn-up in NRU », 2006.
- [48] Y. B. Chun, D. K. Min, G. S. Kim, K. P. Hong, J. R. Park, J. Y. Park, J. M. Seo, J. S. Lee, et J. C. Shin, « Underwater Fuel Inspection for Irradiated LWR Fuels in Korea », 2009.
- [49] B. N. E. Society, *Remote Techniques for Nuclear Plant: Proceedings of the Conference Organized by the British Nuclear Energy Society, Held at Stratford-upon-Avon on 10-13 May 1993*. Thomas Telford, 1993.
- [50] *Fuel Management and Handling: Proceedings of the International Conference Organized by the British Nuclear Energy Society and Held in Edinburgh on 20-22 March 1995*. Thomas Telford, 1995.

- [51] J. J. Serna et M. Q. J. Fernandez, « SICOM: On-site inspection systems XA0201387 », *Adv. Post-Irradiat. Exam. Tech. Water React. Fuel*, p. 33, 2002.
- [52] A. Delfin et R. Mazón, « Visual inspection system and sipping design for spent fuel at Triga Mark III Reactor of Mexico », in *2002 International Meeting on Reduced Enrichment for Research and Test Reactors, Bariloche, Argentina*, 2002.
- [53] « MCNPX home Page ». [En ligne]. Disponible sur: <https://mcnpx.lanl.gov/>. [Consulté le: 27-août-2015].
- [54] « VESTA 2.1.5, Monte Carlo depletion interface code and AURORA 1.0.0, Depletion analysis tool ». [En ligne]. Disponible sur: <http://www.oecd-neo.org/tools/abstract/detail/nea-1856/>. [Consulté le: 27-août-2015].
- [55] R. J. da Fonseca, L. Ferdj-Allah, G. Despaux, A. Boudour, L. Robert, et J. Attal, « Scanning Acoustic Microscopy—recent applications in materials science », *Adv. Mater.*, vol. 5, n° 7-8, p. 508–519, 1993.
- [56] A. Briggs, *Acoustic microscopy*, 2nd ed. Oxford ; New York: Oxford University Press, 2010.
- [57] D. Laux, B. Cros, G. Despaux, et D. Baron, « Ultrasonic study of UO<sub>2</sub>: effects of porosity and grain size on ultrasonic attenuation and velocities », *J. Nucl. Mater.*, vol. 300, n° 2-3, p. 192-197, févr. 2002.
- [58] T. Bosch et M. Lescure, *Selected papers on laser distance measurements*. SPIE Optical Engineering Press, 1995.
- [59] C. C. Liebe et K. Coste, « Distance Measurement Utilizing Image-Based Triangulation », *IEEE Sens. J.*, vol. 13, n° 1, p. 234-244, janv. 2013.
- [60] D. S. Pierce, T. S. Ng, et B. R. Morrison, « A novel laser triangulation technique for high precision distance measurement », in , *Conference Record of the 1992 IEEE Industry Applications Society Annual Meeting, 1992*, 1992, p. 1762-1769 vol.2.
- [61] M. Technologies Course of the International School of Quantum Electronics on Optical Sensors and Microsystems: New Concepts, S. Martellucci, A. N. Chester, et A. G. Mignani, *Optical sensors and microsystems new concepts, materials, technologies*. New York: Kluwer Academic/Plenum Publishers, 2000.
- [62] Y. Kuramoto et H. Okuda, « High-accuracy absolute distance measurement by two-wavelength double heterodyne interferometry with variable synthetic wavelengths », *ArXiv14025575 Phys.*, févr. 2014.
- [63] T. Kubota, M. Nara, et T. Yoshino, « Interferometer for measuring displacement and distance », *Opt. Lett.*, vol. 12, n° 5, p. 310-312, mai 1987.
- [64] K.-E. Peiponen, *Optical measurement techniques: innovations for industry and the life sciences*. Berlin: Springer, 2009.
- [65] M.-C. Amann, T. Bosch, M. Lescure, R. Myllyla, et M. Rioux, « Laser ranging: a critical review of usual techniques for distance measurement », *Opt. Eng.*, vol. 40, n° 1, p. 10–19, 2001.
- [66] M. Sakai, « Capacitive Sensors », in *Handbook of Signal Processing in Acoustics*, D. Havelock, S. Kuwano, et M. Vorländer, Éd. Springer New York, 2008, p. 1339-1345.
- [67] A. S. Morris, *Measurement and instrumentation principles*. Oxford [England] ; Boston: Butterworth-Heinemann, 2001.
- [66] Capacitive Sensor Operation and Optimization How Capacitive Sensors Work and How to Use Them Effectively, An in depth discussion of capacitive sensor theory from Lion Precision. .
- [69] E. Terzic, J. Terzic, R. Nagarajah, et M. Alamgir, « Capacitive Sensing Technology », in *A Neural Network Approach to Fluid Quantity Measurement in Dynamic Environments*, London: Springer London, 2012, p. 11-37.

- [70] M. Howard, « The new generation of inductive sensors », *World Pumps*, vol. 2013, n° 2, p. 10–11, 2013.
- [71] J. Bayard, « Measurement of micromovements with the help of a nonlinear sinusoidal oscillator and an inductive sensor », *Rev. Sci. Instrum.*, vol. 76, n° 3, p. 035101, mars 2005.
- [72] M. Jagiella et S. Fericean, « Miniaturized inductive sensors for industrial applications », in *Proceedings of IEEE Sensors, 2002*, 2002, vol. 2, p. 771-778 vol.2.
- [73] S. M. Djuric, M. S. Damnjanovic, L. F. Nagy, L. D. Zivanov, et N. M. Djuric, « Displacement inductive sensor: Simulation tool algorithm », in *IEEE EUROCON 2009, EUROCON '09*, 2009, p. 671-676.
- [74] J. C. Moulder, E. Uzal, et J. H. Rose, « Thickness and conductivity of metallic layers from eddy current measurements », *Rev. Sci. Instrum.*, vol. 63, n° 6, p. 3455–3465, 1992.
- [75] A. Sethuraman et J. H. Rose, « Rapid inversion of eddy current data for conductivity and thickness of metal coatings », *J. Nondestruct. Eval.*, vol. 14, n° 1, p. 39-46, mars 1995.
- [76] D. Placko, H. Clergeot, et E. Santander, « Physical modeling of an eddy current sensor designed for real time distance and thickness measurement in galvanization industry », *IEEE Trans. Magn.*, vol. 25, n° 4, p. 2861-2863, juill. 1989.
- [77] W. Yin et A. J. Peyton, « Thickness measurement of non-magnetic plates using multi-frequency eddy current sensors », *NDT E Int.*, vol. 40, n° 1, p. 43-48, janv. 2007.
- [78] G. Y. Tian, Z. X. Zhao, R. W. Baines, et P. Corcoran, « Blind sensing [eddy current sensor] », *Manuf. Eng.*, vol. 76, n° 4, p. 179-182, août 1997.
- [79] A. Escolà, S. Planas, J. R. Rosell, J. Pomar, F. Camp, F. Solanelles, F. Gracia, J. Llorens, et E. Gil, « Performance of an ultrasonic ranging sensor in apple tree canopies », *Sensors*, vol. 11, n° 3, p. 2459-2477, 2011.
- [80] D. Andújar, M. Weis, et R. Gerhards, « An Ultrasonic System for Weed Detection in Cereal Crops », *Sensors*, vol. 12, n° 12, p. 17343-17357, déc. 2012.
- [81] M. Friedrich, G. Dobie, Chung Chee Chan, S. G. Pierce, W. Galbraith, S. Marshall, et G. Hayward, « Miniature Mobile Sensor Platforms for Condition Monitoring of Structures », *IEEE Sens. J.*, vol. 9, n° 11, p. 1439-1448, nov. 2009.
- [82] H. Dai, S. Zhao, Z. Jia, et T. Chen, « Low-Cost Ultrasonic Distance Sensor Arrays with Networked Error Correction », *Sensors*, vol. 13, n° 9, p. 11818-11841, sept. 2013.
- [83] D. Marioli, C. Narduzzi, C. Offelli, D. Petri, E. Sardini, et A. Taroni, « Digital time-of-flight measurement for ultrasonic sensors », *IEEE Trans. Instrum. Meas.*, vol. 41, n° 1, p. 93-97, févr. 1992.
- [84] F. E. Gueuning, M. Varlan, C. E. Eugne, et P. Dupuis, « Accurate distance measurement by an autonomous ultrasonic system combining time-of-flight and phase-shift methods », *IEEE Trans. Instrum. Meas.*, vol. 46, n° 6, p. 1236-1240, déc. 1997.
- [85] K.-N. Huang et Y.-P. Huang, « Multiple-frequency ultrasonic distance measurement using direct digital frequency synthesizers », *Sens. Actuators Phys.*, vol. 149, n° 1, p. 42-50, janv. 2009.
- [84] T. Ono, M. Kohata, T. Niyamoto, Ultrasonic phase-sensitive rangefinder with double modulation doppler-free method for shallow seafloor survey, Proc. IEEE 1984 Ultrasonic Symp., 14-16 November 1984, Dallas, TX, USA., pp. 480-483.
- [87] D. Webster, « A pulsed ultrasonic distance measurement system based upon phase digitizing », *IEEE Trans. Instrum. Meas.*, vol. 43, n° 4, p. 578-582, août 1994.

- [88] D. Marioli, E. Sardini, et A. Taroni, « Ultrasonic distance measurement for linear and angular position control », *IEEE Trans. Instrum. Meas.*, vol. 37, n° 4, p. 578-581, déc. 1988.
- [89] T. M. Frederiksen et W. M. Howard, « A single-chip monolithic sonar system », *IEEE J. Solid-State Circuits*, vol. 9, n° 6, p. 394-403, déc. 1974.
- [90] J. C. Jackson, R. Summan, G. I. Dobie, S. M. Whiteley, S. G. Pierce, et G. Hayward, « Time-of-flight measurement techniques for airborne ultrasonic ranging », *IEEE Trans. Ultrason. Ferroelectr. Freq. Control*, vol. 60, n° 2, p. 343-355, févr. 2013.
- [90] Barshan B. and Roman K., "ROBAT: A sonar-based mobile robot for bat-like prey capture" Proceeding of the 1992 IEEE International Conference on Robotics and Automatics. Nice, France - May 1992.
- [92] W. G. MaMullen, B. A. Delaughe, et J. S. Bird, « A simple rising-edge detector for time-of-arrival estimation », *Instrum. Meas. IEEE Trans. On*, vol. 45, n° 4, p. 823-827, 1996.
- [93] B. Barshan, « Fast processing techniques for accurate ultrasonic range measurements », *Meas. Sci. Technol.*, vol. 11, n° 1, p. 45, janv. 2000.
- [94] A. Ş. Sekmen et B. Barshan, « Estimation of object location and radius of curvature using ultrasonic sonar », *Appl. Acoust.*, vol. 62, n° 7, p. 841-865, juill. 2001.
- [95] C. Knapp et G. C. Carter, « The generalized correlation method for estimation of time delay », *IEEE Trans. Acoust. Speech Signal Process.*, vol. 24, n° 4, p. 320-327, août 1976.
- [96] W. Jinjin, Y. Dong, et C. Ping, « Range resolution of ultrasonic distance measurement using single bit cross correlation for robots », in *2010 IEEE International Conference on Information and Automation (ICIA)*, 2010, p. 917-923.
- [97] Y. XU, Y. LI, Z. QU, S. JIN, et C. JIANG, « A TOF Estimation Method for Underwater Acoustic Signal in Confined Underwater Space\* », *J. Comput. Inf. Syst.*, vol. 8, n° 4, p. 1689-1696, 2012.



---

---

## Chapter II

### The high frequency ultrasonic device

---

### *Summary*

I.	Introduction.....	50
II.	Measurement principles .....	51
III.	Transduction elements design .....	52
IV.	Model of the ultrasonic transducer.....	55
1.	Principle .....	55
2.	Application.....	56
3.	Results .....	60
V.	Manufacturing of the ultrasonic transducer .....	61
VI.	Structure control .....	63
VII.	Mechanical holder: Blade and support .....	64
VIII.	Electronic system.....	65
IX.	The high frequency ultrasonic signal.....	67
X.	Processing signal.....	69
XI.	Conclusion .....	72
	List of Figures .....	73
	Reference.....	74

### I. Introduction

Examination of irradiated fuel elements of the High Flux Reactor (French translation Réacteur à Haut Flux) is crucial for assessing the LEU fuel plate behavior. A device using two ultrasound transducers, radiation resistant, has been developed, during this thesis, for such applications. The consequences of this solution are obvious: increase of feedback on irradiated fuel plates, shortening of the cooling time needed before usual Non-Destructive Post irradiation Examination (ND PIE) and cost reduction.

The device is perfectly suited to bended full-size plates. Indeed, thanks to its small size, it could be easily inserted into the water channel and thus could provide useful information on plates swelling. Such device could potentially replace the usual non-destructive PIE for the RHF fuel element. Based on the pulse-echo method, the ultrasonic transducers allow distance measurements through the time of flight (TOF) of the signal reflected on the fuel plate surfaces.

To achieve the microscopic resolution, the system is integrated into a set of high frequency acquisition instruments and excited with frequencies up to 120 MHz. At these frequencies, the ultrasonic wavelengths are sensitive to the device layers and the structure of the transducers plays a central role in the shape of transmitted and received signals. Therefore, these latter have been simulated to theoretically predict the transducers behavior.

The primary goal of this thesis is the development of an ultrasonic device in a collaboration between The Institute Laue-Langevin (ILL) and the Institute of Electronic and Systems (French translation: Institut d'électronique et Systèmes- IES) of University of Montpellier (France). The IES is internationally renowned in the field of ultrasound systems and nuclear environment.

This chapter is divided into seven sections, the first dealing with the general principle of the ultrasonic system. Section 2 gives a detailed description of the ultrasonic device, including the mechanical holding and the transduction element. Section 3 provides the computer simulation of the transducer element to predict its behavior. The designed transducer element is then manufactured. Therefore, the fourth section describes the manufacturing process of the transducers whose structures have been controlled by an acoustic microscope. Finally, sections 5, 6 and 7 describe, respectively, the high frequency electronic system, the high frequency ultrasonic signal and the accurate signal processing developed for distance measurement.

### II. Measurement principles

The inter-plate distance, i.e. water channel thickness, is measured by a waterproof dual piezoelectric transducer (both emitter / receiver) included in the thickness of a stainless steel blade (see Figure 1). This device was designed to be moved inside the water channels this latter having a nominal thickness of 1.8 mm. The water flows between fuel plates whose dimensions are 1.27 mm width and 903 mm long with an involute shape to keep constant the inter-plate distance.

Successful operation of the ultrasonic device relies on accurate time-of-flight (TOF) measurements. A pulse is transmitted and an echo is produced when the transmitted pulse encounters the plate surface. Therefore, the TOF is the time elapsed between the transmission of a pulse and its reception, from which the distance between the transducer and the facing plate can be calculated as  $d_{trans} = \frac{t \times v}{2}$ . Here,  $t$  is the TOF and  $v$  is the speed of sound in water. The total inter-plate distance can be obtained by adding distances measured by each transducer ( $d_{trans1}$  and  $d_{trans2}$ ), to the blade thickness ( $d_{blade}$ ), as:

$$d_{total} = d_{blade} + d_{trans1} + d_{trans2}. \quad (1)$$

Correct distance measurement using ultrasounds depends on how accurately TOF can be measured and how well the speed of sound in the medium is known. The dependence of sound velocity on temperature is detailed in the next chapter.

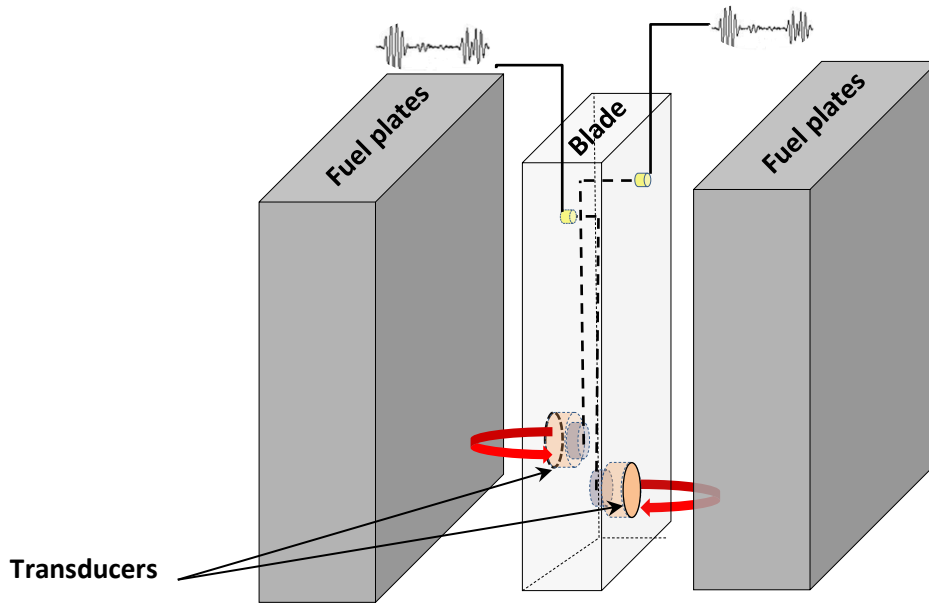


Figure 1: General principle of inter-plate distance measurement

Accurate TOF measurement can be obtained when the two transducers are perfectly parallel to the plates. Indeed, the ultrasonic element emits an acoustic wave whose magnitude in any direction is a function of the angle made with respect to the direction that is normal to the face of the ultrasonic element. The peak emission always occurs along a line that is normal to the transmitting face of the ultrasonic element. At any angle other than the ‘normal’ one, the magnitude of transmitted energy is less than the peak value. Figure 2 shows a numerical simulation of the characteristics of the emission for the ultrasonic element. This is shown in terms of the magnitude of the transmitted ultrasonic wave (measured in dB) in the normal direction of propagation [1].

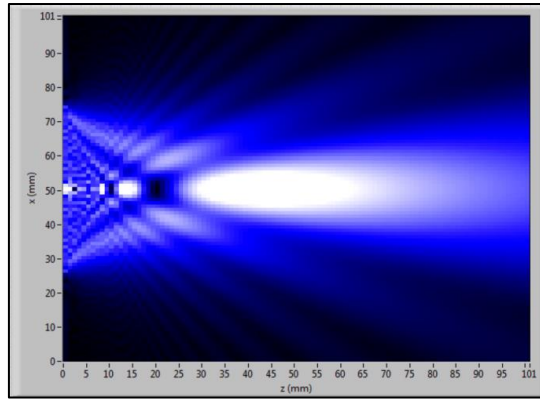


Figure 2: Ultrasonic emission characteristics

### III. Transduction elements design

Conventional ultrasonic transducers generally consist of multiple layers of material: An active element (piezoelectric disc), a backing element and a delay line, all acoustically coupled together. In our case, the two transducers included onto the blade possess the same multilayered structures composed of piezoelectric elements welded on one surface to a golden electrode. An aluminum layer is deposited on the second surface as an electric input and output electrode. Then, a thin glue layer welds the whole system to a delay line, which is a cylindrical rod in silica (6 mm in diameter and 500  $\mu\text{m}$  in height). At the end, an epoxy resin plays the role of a backing medium.

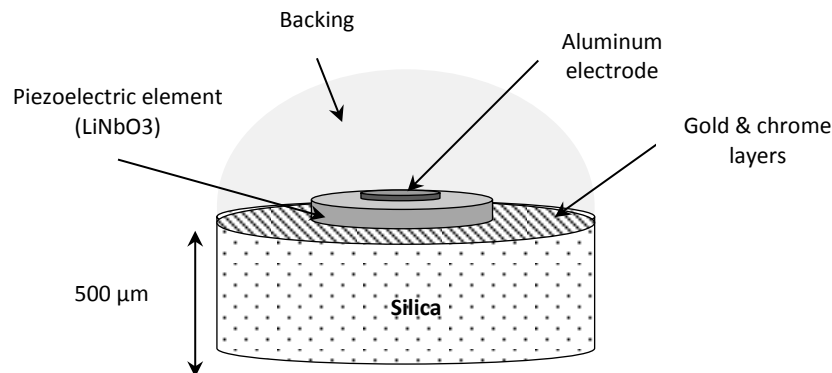


Figure 3: Ultrasonic transducer.

- **Piezoelectric element:**

Piezoelectric transducers produce an output voltage when a force is applied to them. In ultrasonic receivers, the sinusoidal amplitude variations in the ultrasound wave received are translated into sinusoidal changes in the amplitude of the force electric applied to the piezoelectric transducer. Piezoelectric transducers are made from piezoelectric materials. These have an asymmetrical lattice of molecules that distorts when a mechanical force is applied to it. This distortion causes a reorientation of electric charges within the material, resulting in a relative displacement of positive and negative charges. The charge displacement induces surface charges on the material of opposite polarity between the two sides. By implanting electrodes onto the surface of the material, these surface charges can be measured as an output voltage.

## Chapter II: The high frequency ultrasonic device

---

The piezoelectric principle is invertible, and therefore distortion in a piezoelectric material can be caused by applying a voltage to it. This is commonly used in ultrasonic transmitters, where the application of a sinusoidal voltage at a frequency in the ultrasonic range causes a sinusoidal variation in the thickness of the material and results in a sound wave being emitted at the chosen frequency.

Materials exhibiting piezoelectric behavior include natural ones such as quartz, synthetic ones such as lithium niobate, lithium sulphate and ferroelectric ceramics such as barium titanate and Lead Zirconate Titanate [1]. In our case, the lithium niobate ( $\text{LiNbO}_3$ ) has been used as the active element.

The thickness of this active element is determined by the desired frequency of the transducer. Indeed, a thin piezoelectric element vibrates with a fundamental wavelength  $\lambda$  that is twice its thickness  $d$  ( $d=\lambda/2$ ). The frequency and wavelength of ultrasound waves are related according to:

$$f = v/\lambda \quad (2)$$

where  $v$  is the speed of sound in the medium. Therefore, the higher the frequency  $f$  of the transducer, the thinner is the active element. However, smaller is the penetration due to the signal attenuation at high frequencies.

To provide transducers with high resolution, higher-frequency elements are needed. Indeed, high frequency transducers, when used with the proper instrumentation, can improve resolution and the thickness measurement capabilities.

The fuel plate swelling must be characterized with the highest available resolution. To ensure the expected resolution, transducers have been polished to have a thickness around 25  $\mu\text{m}$ , which corresponds to frequency bandwidth extending beyond 120 MHz. Therefore, measurements resolution can reach 12  $\mu\text{m}$ .

- **Delay line :**

For immersed ultrasonic transducers, the delay line is made from material that has acoustical impedance between the active element and water. The most common materials now used for these delay lines are quartz [2] and mercury [3], [4]. The fused silica ( $\text{SiO}_2$ ) is undoubtedly the suitable delay medium for the designed transducers due to its low attenuation at high frequencies [5]. The fused silica is a non-crystalline (glass) form of silicon dioxide (quartz).

Generally, the delay line is a mean for delaying a signal for a predetermined short period to be accurately reproduced at an appropriate later instant. It can also be a mean to protect the active element from scratching. In particular, the delay line plays an important role in the shape of transmitted and received signals. In fact, as the ultrasonic attenuation is small in the delay line, multiple reflections of the ultrasonic waves in the delay line are possible leading to the existence of many ultrasonic echoes. When the delay line is in contact with air, the reflection coefficient is a real number. But, when the transducer is immersed in water, the reflection coefficient becomes a complex number. Hence, for each reflection of an ultrasonic wave at the interface (DL/water), the wave undergoes a reduction of its amplitude and a phase shift [6]. This complex reflection coefficient  $R^* = r_0 e^{j\theta}$ , is calculated with the following

## Chapter II: The high frequency ultrasonic device

relationships (see Figure 4 & 5):  $r_0 = \left(\frac{A_0}{A_I}\right)^{-i}$  and  $\phi = i2\pi ft$ , where  $A_0$  and  $A_I$  are, respectively, the output and input signal strengths, and  $f$  is the operating frequency [7].

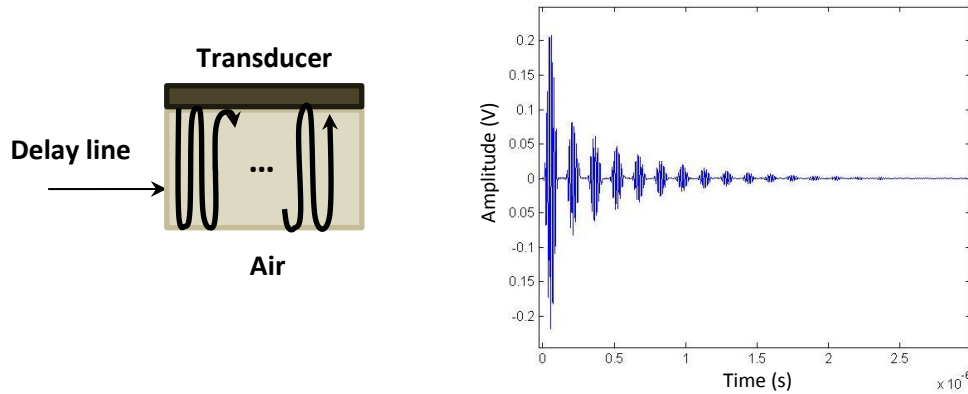


Figure 4: Schematic representation of the Multiple Ultrasonic Reflection in the interface delay line/air

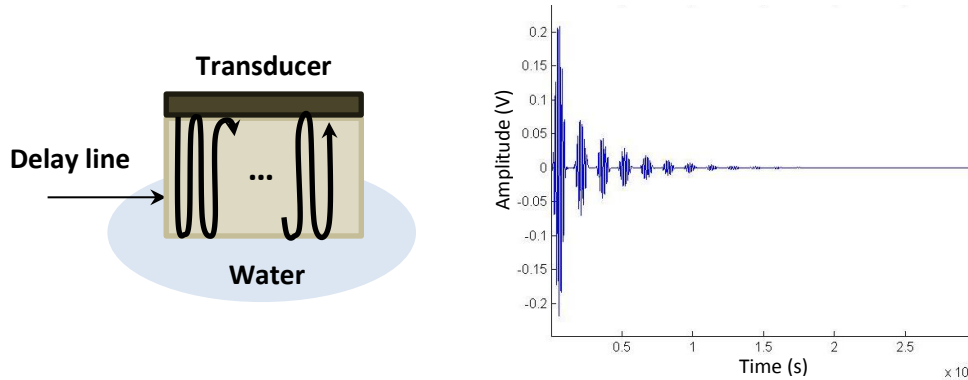


Figure 5: Schematic representation of the Multiple Ultrasonic Reflection in the interface delay line/water

The efficiency of transmission of the sound wave from the piezoelectric element into the delay line, or vice versa, is determined by the intimacy of contact between the active element and line and by the degree of matching of the acoustic impedances of the piezoelectric element and delay line materials. For purposes to be discussed later, the side of the piezoelectric element opposite the delay line is held by golden/chrome/glue layers; the acoustic impedance of such materials will likewise affect the transmission efficiency of the sound wave between the active element and the delay line [2], [7]–[9].

Although the delay line causes signal attenuation, it has also a number of advantages. The delay line improves significantly the accuracy of distance measurement. Indeed, the multiple reflections in the delay line allow TOF measurement not only of a transmitted echo and a reflected one, but of transmitted series of echoes and reflected ones.

- **Backing:**

*This section is based on [10].*

If no backing element were present, the piezoelectric element would typically show a relatively long ringdown response if excited with an impulse voltage, given its low ultrasonic attenuation coefficient. This would lead to poor timing resolution in the reflected echo signals,

and a relatively narrow bandwidth that is poorly suited to most forms of frequency-domain analysis. To overcome this problem, the back surface of the piezoelectric element is usually bonded to a backing element made of attenuation material that dampens the ringdown response and broadens the characteristic resonance by absorbing a portion of the ultrasound energy.

Two properties of the backing element material are key: the acoustic impedance and the attenuation coefficient. The acoustic impedance mismatch between the backing material and piezoelectric element determines the portion of the pulse excitation energy transmitted from the piezoelectric element into the backing. It is highly desirable to prevent any of the ultrasound energy that has been transmitted to the backing material from being returned to the piezoelectric element, where it could contribute to noise or ghost pulses in the received echo pulses. This can be accomplished by incorporating a large value of attenuation coefficient  $\alpha$  times backing thickness  $h$ . Additionally, the boundaries of the backing element can be roughened or angled such that incoming wave energy is not reflected back toward the piezoelectric element.

Backing elements in the designed ultrasonic transducers are made from high-performance composites having good thermal stability, environmental resistance and good mechanical properties. These composites are epoxy resins which serve as polymeric matrix. The good bonding strength to the piezoelectric element and high acoustic attenuation values of such epoxies ensure that the backing elements will keep their integrity over the long term, as the transducers are used at moderate temperatures, while fulfilling the attenuation function [11]–[13]. To provide high acoustic impedance, the epoxy matrices are loaded with metallic filler such as tungsten, iron, copper, magnesium, or aluminum [11]–[15].

The behavior of the transducers, which are multilayered systems, has been simulated from the given transducer design. The main purposes of computer simulations are:

- Deeper insight into the wave propagation in the designed piezoelectric transducers,
- Identification of the ultrasonic wave time of flight by different methods,
- Optimization of transducer design without time-consuming experiments,
- Evaluation of new materials in device design.

## IV. Model of the ultrasonic transducer

### 1. Principle

Manufacturing the piezoelectric transducers as a complex multilayered structure is carried out in conjunction with the development of accurate numerical tools allowing the modeling of such devices. Indeed, studies of acoustic response and wave propagation through transducer layers are of paramount importance for the optimum design and optimization of the acoustical properties of multilayer materials. The behavior of these combinations of materials depends more or less on the dimensions and the boundary conditions at the edges. Nevertheless, interesting results can be obtained by modeling the samples as infinite plates subjected to

incident plane waves. Using the transfer matrix related to each layer considerably simplifies the modeling [16]–[22].

The Transfer Matrix Method is based on a theory, which says that the relation between the pressure and bulk flow of two ends of a sound propagating route can be expressed by a matrix. The transfer matrix can be looked upon as an inherent property of a material because of its invariance. If the transfer matrix of a material is known, most of the acoustical properties of the material can be obtained. Because of the continuity of sound pressure and velocity, the matrices of all the component layers can be combined together into a total matrix which can be used to predict the acoustical properties of multilayer materials. The type of transfer matrix is determined by such factors as physical properties of the material, boundary conditions, selected state variables and so on [22].

The Transfer Matrix Method (TMM) was developed first by Thomson [19]. In his paper, Thompson stated correctly that the proper boundary conditions to be used at the interfaces between layers were continuity of stresses and particle velocities. However, due to his particular formulation of the problem his final equations are valid only for certain special cases such as multiple fluid layers, or multiple solid layers with identical shear moduli sandwiched between fluid layers. Brekhovskikh's treatment parallels that of Thompson and yields equations whose validity is limited to the same special cases as are those of Thompson. Haskell was the first to correct the formulation of the problem so that the resulting equations were applicable to the general multiple layer case [20]. D. L. Folds and C. D. Loggins propose an analysis parallel to the Brekhovskikh's treatment (since Brekhovskikh is widely available as a standard reference work), by determining the transmission and reflection coefficients with appropriate corrections [21]. Then, a number of recent papers have been aimed at derivation of transfer matrices for the cases of stacks of fluid and solid layers [23] one-dimensional pressure excitation due to oblique incidence [24], heterogeneous plane waves [25], and two-dimensional pressure excitation due to oblique incident wave propagating through a multilayer stack [17].

Much of our model follows D. L. Folds and C. D. Loggins, with some minor changes in notation. In this model, a plane wave originates in layer  $n + 1$  and proceeds through the  $n-1$  intervening layers to emerge into layer 1, which is of semi-infinite extent in the  $z$  direction. The layers are of assumed infinite extent in the  $x$  and  $y$  directions, and the plane wave incident upon layer  $n$  is assumed to lie in the  $xz$  plane, making the problem two dimensional (see Figure 10).

When a plane wave is incident on a layer at an angle, it induces a normal stress  $\sigma_y$ , and a shear stress  $\tau_{xy}$  in the layer and these two stresses are accompanied by normal particle velocity  $v_y$  and tangential particle velocity  $v_x$ . The boundary conditions require continuity of normal and shear stresses, and normal and tangential displacements at the interfaces between layers. For a time harmonic wave (where time dependencies  $\exp(i\omega t)$ ), the particle velocity is given by  $v = i\omega u$ , where  $u$  is the particle displacement and thus continuity of displacement is the same as continuity of particle velocities.

## 2. Application

*This section is based on [21].*

In the model, a plane wave with an oblique incidence ( $\theta \approx 0$ ), is transmitted through a multilayer structure. This structure includes the transducer layers (piezoelectric element, the

## Chapter II: The high frequency ultrasonic device

golden electrode, and the delay line of silica), the water channel, and the fuel plate (see Figure 6). The thicknesses of these three parts of the modeled structure are, respectively, 500  $\mu\text{m}$ , 1.6 mm and 1.27 mm. All these layers are taken in the semi-infinite plane (XY), and the positive z-axis is directed upwards.

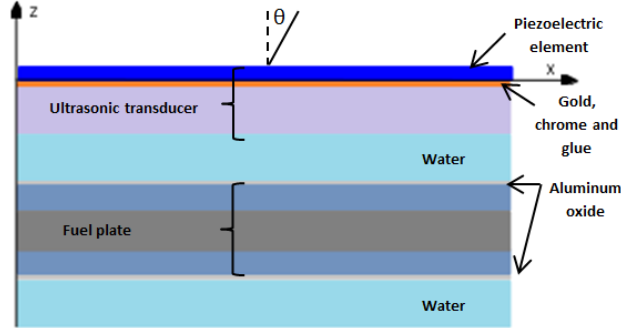


Figure 6: The modeled multilayer structure.

To take into account physical and dimensional parameters of each plate, the model require numerical input data like the longitudinal and transverse velocities, the volume density and the thickness (the values of these parameters, for each layer, are shown in Appendix 1). Then based on [21], the model calculates the reflection and transmission coefficients from the velocities and stresses in layers. In any layer, the velocities and stresses can be expressed in terms of the following potential functions:

$$\phi_1 = [A_1 * \exp(i\alpha_1 z) + B_1 * \exp(-i\alpha_1 z)] \exp[i(\omega x - \omega t)] \quad (3)$$

$$\psi_1 = [C_1 * \exp(i\beta_1 z) + D_1 * \exp(-i\beta_1 z)] \exp[i(\omega x - \omega t)] \quad (4)$$

$\phi_1$  and  $\psi_1$  are respectively the compressional waves potential and shear wave potential. With  $\beta_1 = (K_1^2 - \sigma^2)^{1/2}$ ,  $\alpha_1 = (k_1^2 - \sigma^2)^{1/2}$  and  $\sigma = k_1 \sin \theta_1$ .

At any point in the system, we have: 
$$v_x^{(1)} = \frac{\partial \phi_1}{\partial x} - \frac{\partial \psi_1}{\partial z} \quad (5)$$

$$v_z^{(1)} = \frac{\partial \phi_1}{\partial z} + \frac{\partial \psi_1}{\partial x} \quad (6)$$

$$Z_z^{(1)} = \frac{i \left[ \lambda \left( \frac{\partial v_x^{(1)}}{\partial x} + \frac{\partial v_z^{(1)}}{\partial z} \right) + 2\mu \frac{\partial v_z^{(1)}}{\partial z} \right]}{\omega} \quad (7)$$

and 
$$Z_x^{(1)} = \frac{i\mu \left[ \lambda \left( \frac{\partial v_x^{(1)}}{\partial z} + \frac{\partial v_z^{(1)}}{\partial x} \right) \right]}{\omega} \quad (8)$$

By calculating these derivatives, at the uppermost interface (at  $z = d_n - \varepsilon$ , where  $\varepsilon$  is infinitesimal and  $d_n$  is the thickness of the layer  $n$ ), the following result is obtained:

$$\begin{bmatrix} v_x^n \\ v_z^n \\ Z_x^n \\ Z_z^n \end{bmatrix} = L_1 * \begin{bmatrix} A_n + B_n \\ A_n - B_n \\ C_n + D_n \\ C_n - D_n \end{bmatrix} \quad (9)$$

where  $L_n$  matrix depends on the thickness, the density, and the sound velocities of each layer.

$$\text{At the beginning (interface) of the second layer (} z = -\varepsilon \text{):} \quad \begin{bmatrix} v_x^{n-1} \\ v_z^{n-1} \\ Z_x^{n-1} \\ Z_z^{n-1} \end{bmatrix} = L_2 * \begin{bmatrix} A_n + B_n \\ A_n - B_n \\ C_n + D_n \\ C_n - D_n \end{bmatrix} \quad (10)$$

$$\text{From (9) and (10):} \quad \begin{bmatrix} v_x^n \\ v_z^n \\ Z_x^n \\ Z_z^n \end{bmatrix} = L_1 * L_2^{-1} \begin{bmatrix} v_x^{n-1} \\ v_z^{n-1} \\ Z_x^{n-1} \\ Z_z^{n-1} \end{bmatrix} = \begin{bmatrix} a_{11}^{(n)} & a_{12}^{(n)} & a_{13}^{(n)} & a_{14}^{(n)} \\ a_{21}^{(n)} & a_{22}^{(n)} & a_{23}^{(n)} & a_{24}^{(n)} \\ a_{31}^{(n)} & a_{32}^{(n)} & a_{33}^{(n)} & a_{34}^{(n)} \\ a_{41}^{(n)} & a_{42}^{(n)} & a_{43}^{(n)} & a_{44}^{(n)} \end{bmatrix} \begin{bmatrix} v_x^{n-1} \\ v_z^{n-1} \\ Z_x^{n-1} \\ Z_z^{n-1} \end{bmatrix} = C_n \begin{bmatrix} v_x^{n-1} \\ v_z^{n-1} \\ Z_x^{n-1} \\ Z_z^{n-1} \end{bmatrix} \quad (11)$$

where  $C_n = [a_{ij}^{(n)}]$ . The values for the quantities  $a_{ij}^{(n)}$  are given in the appendix 1.

Application of the boundary condition at  $z=0$  equates the velocities and stresses in layer  $n$  with those in layer  $n-1$  at the interface. By repeating the same process for each  $n-1$  layers between layers  $n+1$  and  $1$ , the global transfer matrix  $[C]$  of the structure can be obtained from the product of all elementary transfer matrices  $[C_i]$  of each layer:

$$\begin{bmatrix} v_x^n \\ v_z^n \\ Z_x^n \\ Z_z^n \end{bmatrix} = C_n * C_{n-1} * \dots * C_2 \begin{bmatrix} v_x^1 \\ v_z^1 \\ Z_x^1 \\ Z_z^1 \end{bmatrix} = \begin{bmatrix} A_{11} & A_{12} & A_{13} & A_{14} \\ A_{21} & A_{22} & A_{23} & A_{24} \\ A_{31} & A_{32} & A_{33} & A_{34} \\ A_{41} & A_{42} & A_{43} & A_{44} \end{bmatrix} * \begin{bmatrix} v_x^1 \\ v_z^1 \\ Z_x^1 \\ Z_z^1 \end{bmatrix} \quad (12)$$

$$\text{From (12), the shear stress } Z_x^n \text{ is equal to } Z_x^n = A_{41}v_x^1 + A_{42}v_z^1 + A_{43}Z_x^1 + A_{44}Z_z^1 \quad (13)$$

As the media in contact with layers  $0$  and  $n$  are assumed to be water, the shear stresses on both exposed surfaces of the multi-layer system will be zero:  $Z_x^n = Z_x^1 = 0$ , which yields to:

$$v_x^1 = -(A_{44}/A_{42})v_z^1 - (A_{43}/A_{41})Z_z^1 \quad (14)$$

Substituting this into Eq. (12) and remembering that  $Z_x^n = Z_x^1 = 0$ ,  $v_z^n$  and  $Z_z^n$  can be written solely according to  $v_z^1$  and  $Z_z^1$ .

$$v_z^n = M_{22}v_z^1 + M_{23}Z_z^1 \quad \text{and} \quad Z_z^n = M_{32}v_z^1 + M_{33}Z_z^1 \quad (15)$$

where  $M_{kl} = f(A_{ij})$ . The values for the quantities  $M_{kl}$  are given in the appendix 1.

Reflection and transmission coefficients are expressed according to:

$$T = \rho_1 \times B_1 / (\rho_{n+1} \times B_{n+1}) \quad \text{and} \quad R = A_{n+1} / B_{n+1} \quad (16)$$

## Chapter II: The high frequency ultrasonic device

where  $A$  and  $B$  are the incident and reflected wave amplitudes. Knowing that,  $\psi_{n+1} = \psi_1 = 0$  we deduce that:

$$v_z^n = i\alpha_{n+1}(A_{n+1} + B_{n+1}) \quad \text{and} \quad Z_z^n = -i\rho_{n+1}\omega(A_{n+1} + B_{n+1}) \quad (17)$$

$$\text{with } v_z^1 = i\alpha_1 B_1 \quad \text{and} \quad Z_z^1 = -i\rho_1\omega B_1 \quad (18)$$

Substitution of these values, (18) into (15) yields:

$$T = \frac{\rho_1 \times B_1}{\rho_{n+1} \times B_{n+1}} = \frac{2Z_1}{(M_{22} + Z_1 M_{23})Z_{n+1} + M_{32} + Z_1 M_{33}} \quad (19)$$

$$R = \frac{A_{n+1}}{B_{n+1}} = \frac{M_{32} + Z_1 M_{33} - (M_{22} + Z_1 M_{23})Z_{n+1}}{M_{32} + Z_1 M_{33} + (M_{22} + Z_1 M_{23})Z_{n+1}} \quad (20)$$

where  $Z_1 = \rho_1 \omega / \alpha_1$  and  $Z_{n+1} = \rho_{n+1} \omega / \alpha_{n+1}$ , are the impedances of layers  $1$  and  $n+1$ , respectively.

At the end, the computer program used (19) and (20) to predict the transmission and the reflection of a plane wave incident on the multilayer system.

In the experimental measurements, the piezoelectric element is excited by an electrical pulse. An acoustic echo is thus produced and then propagates through the multilayer system. The generated echo consists of a few cycles of oscillations at the nominal frequency of the wave, as illustrated in Figure 7.

This pulsed wave can be described as being constructed from a range of frequencies centered on the nominal frequency. Interference between the components at the different frequencies effectively results in the formation of the pulse. The graph of amplitude versus frequency for the experimental pulse shows a distribution of frequency components centered on the nominal frequency (see Figure 7).

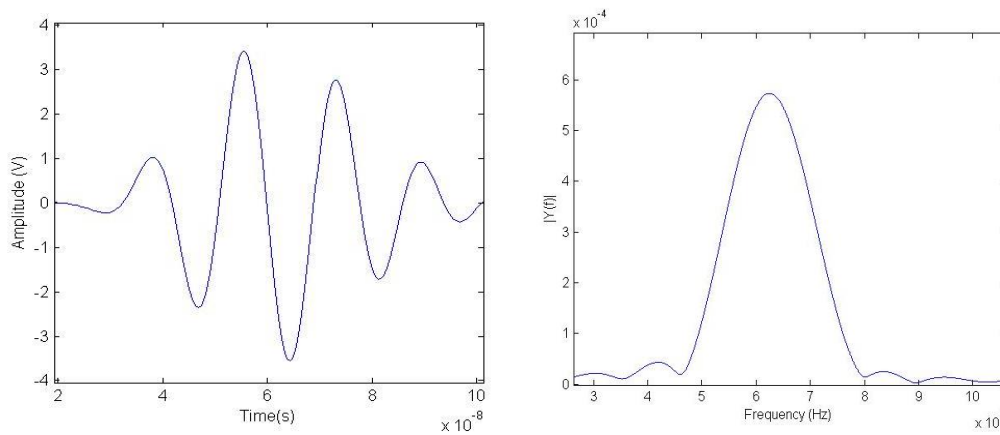


**Figure 7: An ultrasound pulse: (a) the temporal signal; (b) the spectrum pulse.**

In the computer simulation, the initial echo is based on the experimental one (see Figure 7). Then, for each frequency present in the signal spectrum the reflection and transmission coefficients are computed and are multiplied by the respective spectrum amplitude. The multiplication results are then assembled and an inverse transform is calculated leading with

the formation of the transmitted and reflected ultrasonic echoes. The same processes are then repeated for the two generated echoes (transmitted and reflected signal) and in the different layers (see Figure 8).

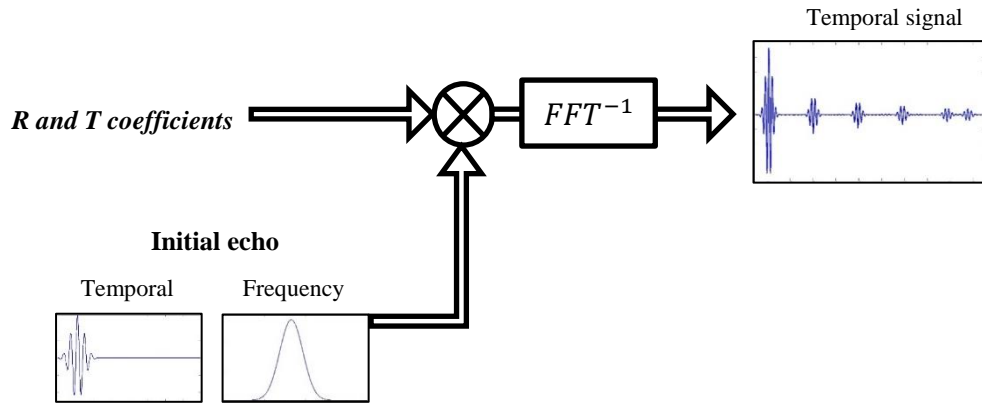


**Figure 8: Simulation of the temporal signal**

### 3. Results

Through the model, a deeper insight of the designed transducer behavior is performed. Indeed, at high frequencies, the structure of the multilayered transducer plays a crucial role in the shape of transmitted and received signals. In fact, when an electrical pulse excites the piezoelectric element, an ultrasonic echo is produced. The frequency content of the generated echo depends on the fine structure of the transducer, namely, the piezoelectric element and the contact layer (chromium, gold and glue layers). This echo propagates then through the layers, producing thus series of acoustic echoes. Multiple reflections occur in the silica delay line leading to echoes reflected to the sensor (a) and to series of complementary transmitted signals in water. The successive reflections of the latter in the water layer between the silica and the plate interface then lead to series of signals with decreasing amplitudes one of which is presented in (b). Due to reciprocity, the same piezoelectric element is used to acquire these reflected signals that are then processed by an electronic system (see Figure 9).

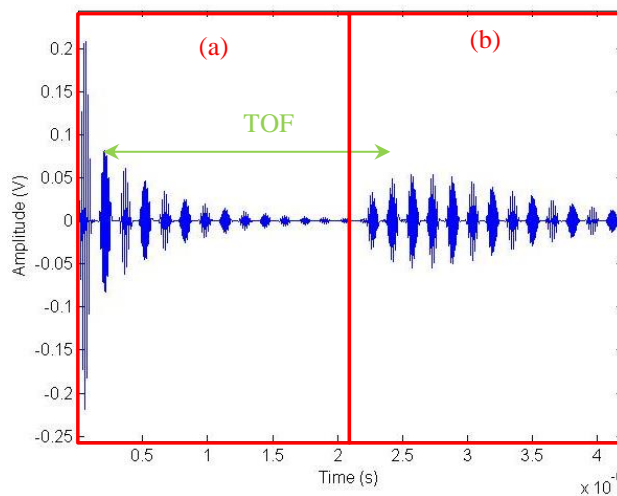


**Figure 9: The transducer simulation shows two series of echoes: (a) reflection of the signals within the multilayer structure of the transducer; (b) the receipt of the dual series after propagation in the water channel and reflection on the fuel plate; TOF is the time elapsed between the two series of echoes.**

## Chapter II: The high frequency ultrasonic device

For the first series of echoes (radiations in the delay line), the first echo corresponds to the piezoelectric excitation. Then, for each reflection of the acoustic echo at the interface (Delay line/water), the wave undergoes a reduction of its amplitude (about 0.04 V) and a phase shift (of  $\pi/2$ ). The time interval between echoes corresponds to the delay line thickness.

The second series of echo is a reflection of the first series of echoes on the plate surface. A primary cause of the first echo attenuation is mainly related to the contact (gold/chrome/glue layers) between the piezoelectric element and the delay line. From the time interval between the two series of echoes in the water channel thickness can be deduced.

### V. Manufacturing of the ultrasonic transducer

This section describes briefly the manufacturing process of the high frequency ultrasonic transducer performed within the Institute of Electronics and Systems (IES). Manufacturing process:

As mentioned above, the principal components of the designed transducer are the piezoelectric element, electrodes, the delay line, and the backing. The manufacturing steps are as following:

- **The delay line:**

The manufacture of the ultrasonic transducer begins from with a silica rod with a regular diameter and two ends perfectly parallels. To achieve the desired thickness, the delay line has been polished.

- **The golden electrode:**

The golden electrode is performed by vacuum metallizing. This technique involves heating the coating metal to its boiling point in a vacuum chamber (see Figure 10), then letting condensation deposit the metal on the substrate surface. Resistance heating is used to vaporize the coating metal (see Figure 11). This technique involves the conversion of the electricity into heat through the process of Joule heating. Indeed, electric current passing through the coating element encounters resistance, resulting in heating of the element.



Figure 10: The vacuum chamber.

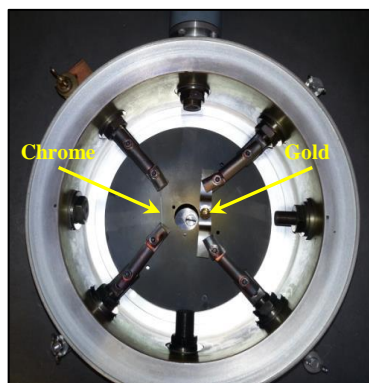


Figure 11: The coating metals

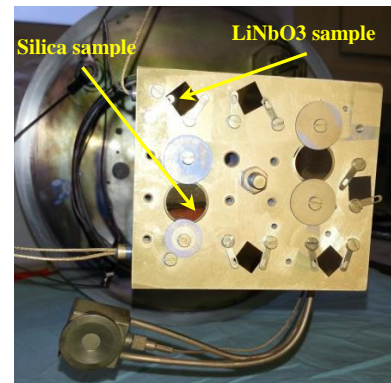


Figure 12: the delay line and piezoelectric element samples.

The coating metals were the chrome and gold. These metals were successively projected by metallization on the surfaces of the delay line and the piezoelectric element. At first, the chromium layer is filed to improve the corrosion resistance, and then the gold layer to ensure

## Chapter II: The high frequency ultrasonic device

electric conductivity. Obtaining a regular deposition assumes a regular initial surface (see figure 12).

- **Contact (delay line / piezoelectric element):**

The coated side (with the golden layer) of the piezoelectric element is held by a thin adhesive layer to the coated side (with the golden layer) of the delay line. We use for this purpose the glue mono-component CYANOLIT. It dries rapidly at room temperature by absorption of moisture in the air.

- **The piezoelectric element:**

Polishing the piezoelectric element is a key step in the manufacture of the ultrasonic transducer. This step yields the desired piezoelectric element thickness that is directly related to its frequency. The piezoelectric element was polished manually by maintaining the whole system in a cylindrical support, and by using a high speed rotating disk (see Figure 13). The alumina was used as polishing paste.



Figure 13: Polishing of the piezoelectric element.

During the polishing, the thickness of the piezoelectric element is measured to control the flatness and especially the final thickness of the piezoelectric element.

- **The aluminum electrode:**

On the polished side of the piezoelectric element, an aluminum electrode is deposited by vacuum metallizing. This electrode is an electric input and output of the transducer; it can apply an electric signal to excite the piezoelectric element. Reciprocally, an electric potential can be generated at the reception of an ultrasonic wave.

The aluminum layer is performed by placing the transducer within a cylindrical mold in which the shape of the electrode was hollowed. Then, in the vacuum chamber, a nanometer layer of the aluminum is deposited on the piezoelectric element surface (see Figure 14).

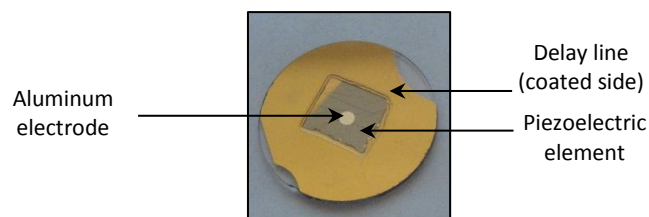


Figure 14: Piezoelectric element bonded to the delay line

- **Electrical contact:**

The transducer elements are now integrated in the two cavities (of 6 mm of external diameter) formed on the blade. To excite the piezoelectric element at the transmission, and to detect the acquired signal, two semi-rigid coax cables (of 0.6 mm diameter) are set in the grooves made in both faces of the blade. The ends of the cables are bonded by charged glue to the aluminum electrode. The mass is taken on the gold layer of silica delay line. The epoxy resin is then placed on the back side of the transducer as a backing (see Figure 15). The second ends of cables are connected to the coax cables of 10 m length.

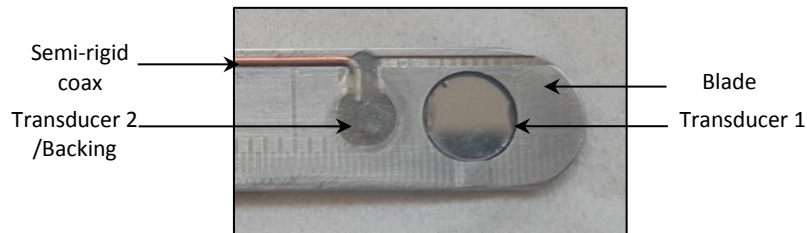


Figure 15: One end of the high frequency ultrasonic device

## VI. Structure control

To check the quality of the transducers structures, acoustic images have been performed to make visible transducers external and internal features, including defects such as cracks, non-flatness, delaminations, and voids.

- *Surface imaging:*

Surface imaging is used for observing microstructures beneath the sample surface within a range of one wavelength of the incoming signal. High resolution is therefore required and the operating frequency is typically above 500 MHz and often reaches the gigahertz range [26]. This technique has been used to illustrate the transducer surface image. Figure 16, clearly distinguishes the two mediums (silica/ blade) with the contrast being related to the reflective conditions in the focusing plane during the scanning. The image contrast improves noticeably when the transducer is slightly defocused. The circle of approximately 1 mm in diameter is used to locate the active piezoelectric element part. The crack shown on the left of the image is a consequence of thinning the piezoelectric element performed on the fragile delay line (500 $\mu$ m). This crack doesn't affect the transducer operation because it is away from the transducer active part. The dark lines in the form of circles correspond to the surface of the support on which is placed the transducer.

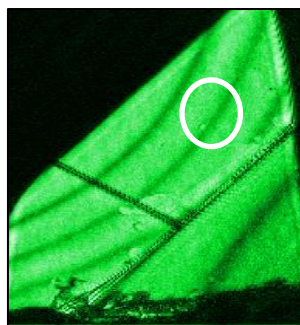


Figure 16: Acoustic microscopy image of the interface support - piezoelectric element

- *Phase contrast images:*

The phase has always offered the possibility of increasing the experimental precision in many fields of science. In acoustics, the phase makes its contribution: Firstly, it offers a direct indication of material properties as in the measurement of Rayleigh-wave velocity. Also, the results of the phase measurement can be used to infer the width and the height of surface features. Finally, the combination of amplitude and phase measurements can be used in the reconstruction processes in which complete information about the interaction between acoustic field and material is required, as in the inversion of  $V(z)$  data to find the reflection coefficient as a function of angle [27]. Moreover, the quantitative data obtained by the phase technique can lead to image acquisition. Phase contrast acoustic images are obtained by displaying the phase difference between the reflected wave and a reference one, instead of the wave amplitude. In Figure 17, the image of the interface support-transducer is presented. It certifies that thinning and polishing was performed with good quality due to the low phase variation identified in the active region.

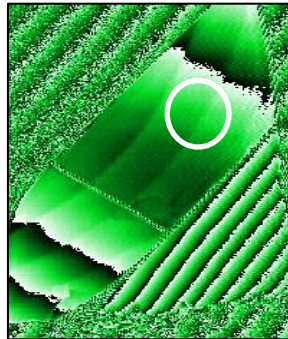


Figure 17: Acoustic microscopy image of the interface support - piezoelectric element

### VII. Mechanical holder: Blade and support

To easily introduce the transducers in the water channel, these latter were mounted on one end of a stainless steel blade (see figure 18). Manufactured with nuclear QA (materials, cleanness, dimensional control...), the blade has the following dimensions: a thickness of 1 mm, a width of 10 mm and a length of 1500 mm. To set up the cables, a groove was drilled on both faces of the blade. The inner diameter of each transducer hosting hole was 6 mm with a spot facing (see Figure 20). The blade material was 316L stainless steel.

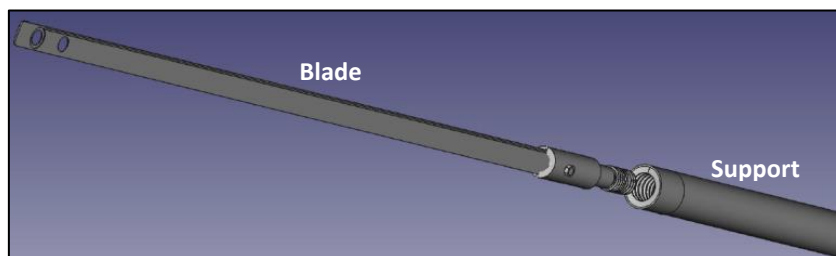


Figure 18: the ultrasonic sensor.

The blade is then connected to a supporting system (a 22 mm diameter and 5 m long tube) handled manually from above by an operator (figure 18). The connection is made possible thanks to screws positioned on the blade side and to a thread on the pole side (Figure 19).

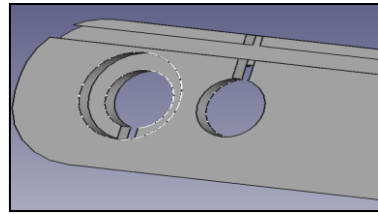
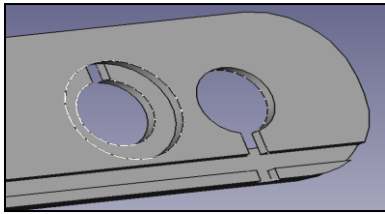


Figure 19: Upper end of the Measurement saber (both sides)



Figure 20: Connection system.

### VIII. Electronic system

The implementation of distance measurement system requires the use of the described high frequency ultrasonic device which is integrated to an electronic chain of signal acquisition and processing. The essential elements of the electronic system are shown schematically in Figure 21.

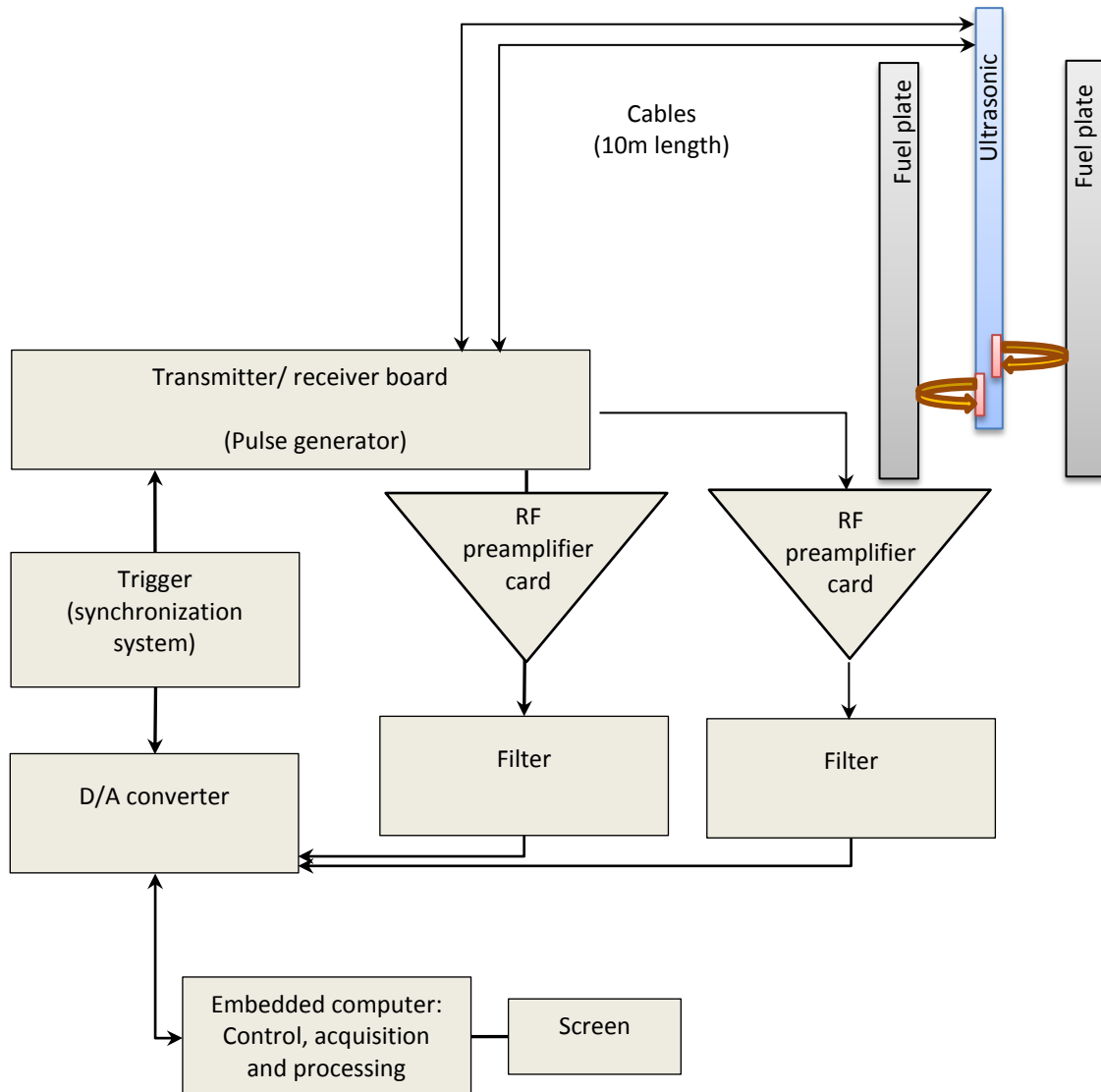


Figure 21: block diagram of the distance measurement system

## Chapter II: The high frequency ultrasonic device

---

The electronic system, representing the interface between the computer and the high frequency ultrasonic device includes:

- **Pulse generator:**

A dual transmitter/ receiver board was designed and developed by IES institute to excite the piezoelectric transducer and then receive its response. This board creates an electrical signal of high energy (a few watts maximum) to generate an ultrasound pulse. Indeed, to produce distinct echo that corresponds to a reflection from a particular interface, the ultrasound must be transmitted in the form of burst or pulse. To allow echoes from closely spaced interfaces to be resolved separately, the pulse must be short.

To excite the transducers operating at frequencies up to 120 MHz, a pulse (about 8.3 ns) is generated. Its echoes contain information at a wide range of frequencies. The information contained in an echo from a long pulse is concentrated near the nominal frequency and gives a stronger signal at that frequency. However, a long pulse results in poor distance resolution [28].

To summarize, the transmitter/receiver board initiates a pulse to activate the piezoelectric transducer. The ultrasound wave propagates through mediums, resulting in echoes reflected from interfaces. Then, the board receives the reflected signal and before being transmitted to the amplifier, the board limits the signal amplitude to protect the amplifier from high tension. Consequently, the first echoes are saturated (see Figure 22 in the next section).

- **PXI platform:**

In order to have a compact system, easy to carry, the electronic acquisition system was integrated in the PXI platform. The PXI (PCI extension for Instrumentation) is a modular instrumentation platform originally developed by National Instruments. PXI uses PCI-based technology and it adds a rugged CompactPCI mechanical form-factor, an industry consortium that defines hardware, electrical, software, power and cooling requirements. Then PXI adds integrated timing and synchronization that is used to route synchronization clocks, and triggers internally [29]. Our PXI platform includes two amplifiers, one digitizer/oscilloscope and one controller board.

- **Amplifier:**

Amplifying the received signal is carried out by NI PXI-5690, which is a 100 kHz to 3 GHz, two-channel programmable amplifier and attenuator with one fixed gain path (30 dB) and one programmable gain/attenuation path (-10 to +20 dB). The combined paths offer up to 37 dB of total signal gain at 2.5 GHz when signal paths are cascaded.

- **A/D converter:**

The amplified signal is then converted into a numerical data to be displayed and then processed. The analog/digital converter consists of the NI PXIe-5162 digitizer/oscilloscope. Each of its two analog input channels has a vertical resolution of 10 bits. These channels can acquire up to 5 GS/s with 1.5 GHz of bandwidth on the 50  $\Omega$  path and 300 MHz on the 1 M $\Omega$  path.

- **The controller system:**

Most PXIe instrument modules (amplifier, D/A converter...) are register-based products, which use software drivers hosted on a controller system to configure them. In our case, the controller consists of the NI PXIe-8135.

- **Acquisition software:**

To set up an acquisition, a program based on the NI-SCOPE software was developed. The software integrates the full functionality of the digitizer hardware into NI LabVIEW. Its configuration functions allow setting triggers, input impedance, DC offset, vertical range, sampling rate, and much more. The diagram illustrating the essential elements of the acquisition software is shown in the Appendix 2.

### IX. The high frequency ultrasonic signal

After describing the material aspects of the high frequency ultrasonic device (mechanical holder, acoustic transducer, electronic system), it is largely time to see the result of all these aspects that is the acoustic signal. This experimental signal is then compared to the simulated one.

Figures 22 and 24 show the experimental signal acquired by placing the transducer into a quartz tank of 2.5 mm width. The coupling medium was pure water. The same configuration was modeled through the transfer matrix method described above.

The principal signal transmitted into the delay line is divided in two portions. The first portion is reflected on the line ends, which gives the first series of echoes (see Figure 22). While the remaining acoustic signal propagates through the water channel and then it reflects on the plate surface, giving thus the second series of echoes (see Figure 24).

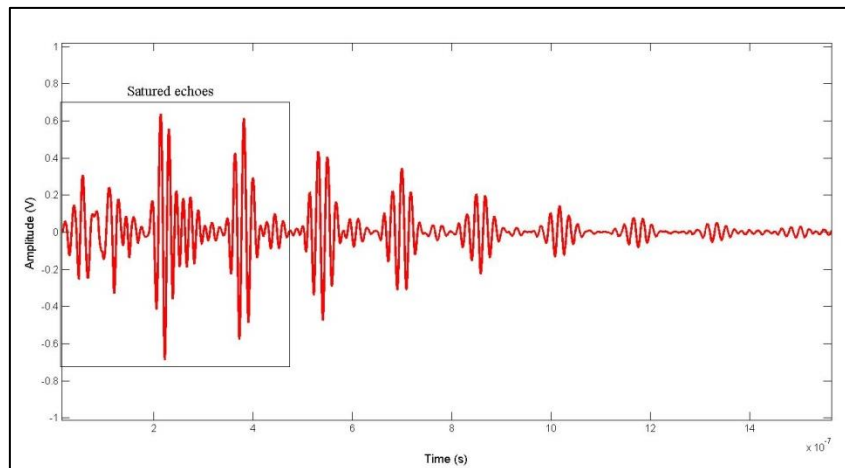


**Figure 22: The first series of echoes. The time interval between echoes is related to the delay line thickness.**

Several observations can be made from Figure 22. On one hand, the diminution and the attenuation of the echoes amplitude can be explained by the loss in signal strength in passing through the delay line. A  $\pi/2$  phase shift is also observed when the signal is reflected at the silica/water interface. That is mainly due to the high refractive index of water relative to that

## Chapter II: The high frequency ultrasonic device

of silica. On the other hand, we notice a saturation of the three first echoes. That is mainly due to the pulse generator that is very powerful, and thus limits the level of the received signal in order to protect the amplifier.

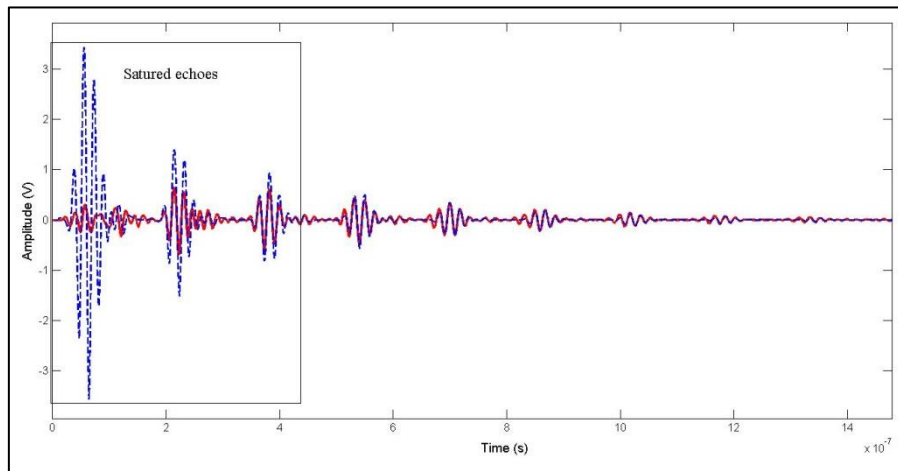


**Figure 23: First series of echoes. Dash line (blue) corresponds to the simulated signal. Continuous line (red) corresponds to the experimental signal**

Except for the saturation of the three first echoes, the experimental signal is similar to that previously simulated from the designed transducer. Indeed, both signals have almost the same phase and the same amplitude with a slight difference. This similarity confirms the quality of the manufactured transducers which respects the parameters defined in the conception study. To measure the ultrasonic wave time of flight, the simulated first series of echoes is used instead of the experimental one due to the saturation effect.

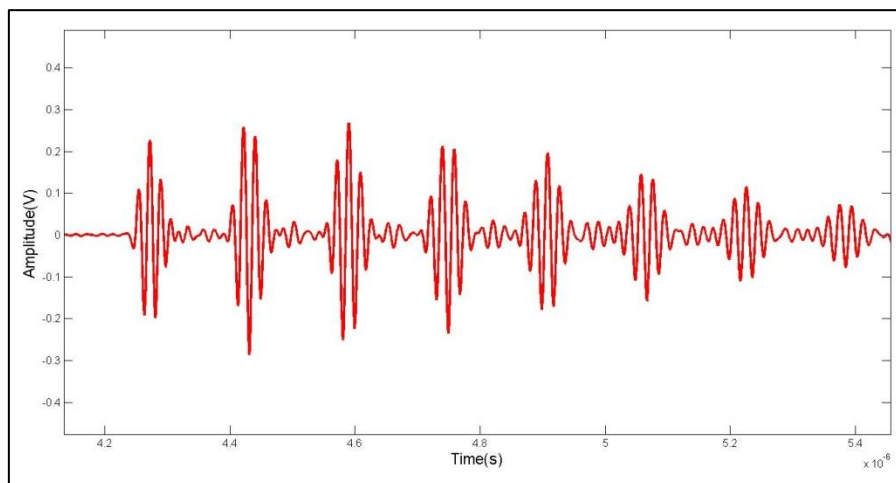


**Figure 24: The second series of echoes. The time interval between echoes is related to the delay line thickness.**

Figure 24 shows reflections of the ultrasonic signals on the inner edges of the tank. The time interval between this series of echoes and the first one is proportional to distance between the transducer and the facing edge.

The reflected echoes are not only attenuated but are also slightly distorted. A primary cause of pulses distortion is the superposition upon weak echoes of the first series due the closely spaced interfaces. Other causes may be attributed to the layers (gold, glue, chrome)

between the piezoelectric element and the delay line. The same attenuation and distortion of echoes is shown also in the simulated signal (see figure 25). Except the enlargement of the experimental echoes, both the simulated and experimental signals have almost the same phase and amplitude. The echoes enlargement is mainly due to frequency dispersion which is being integrated to the model.

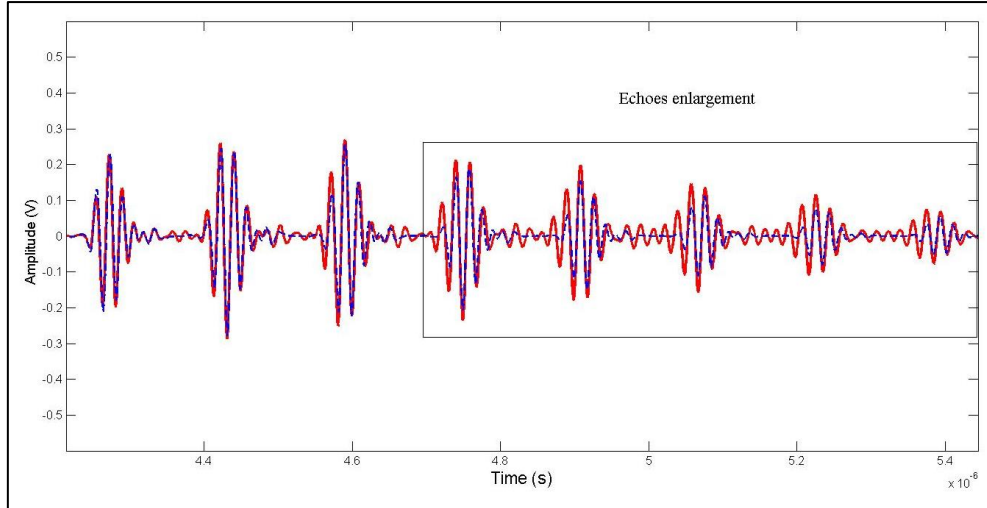


Figure 25: Second series of echoes. Dash line (blue) corresponds to the simulated signal. Continuous line (red) corresponds to the experimental signal.

## X. Signal processing

To extract the inter-plate distance measurement from the high frequency ultrasonic signals, a specific signal processing enabling measurement with high accuracy and high resolution was developed. The method of ultrasonic distance measurement is based on the pulse-echo method, which determines the time-of-flight (TOF) of the ultrasonic wave. As previously mentioned, the TOF is the time interval from the transmission of the ultrasonic pulse to the reception of the echoes reflected from the facing plate. The distance is estimated from the product of the TOF and the propagation velocity of the ultrasonic wave. The most frequently employed methods for TOF measurements are threshold method [30], [31], curve-fitting method [32] and cross-correlation method [44]–[48].

- **Threshold method:**

The simplest form of measuring the TOF is the threshold method. This technique involves detecting the arrival of an acoustic signal when its amplitude exceeds a given amplitude level. Thresholding systems do not require any complex computations, but they suffer from low sampling frequency, low signal-to-noise ratio (SNR), and inherent bias, particularly when the received signal has been greatly attenuated (see Figure 26).

Noise can increase the likelihood of false positives and threshold mechanisms are particularly susceptible to this type of error. In low-SNR environments, it is necessary to perform some form of amplification or, equivalently, reduce the threshold for detection, making it more likely that false positives occur as the threshold level and noise level become comparable. The effect of low sampling frequency is subtler and is implicated in all time-domain methods: low sampling frequency decreases the resolution with which one can determine the time at which an event (such as a threshold being crossed) occurred. In the case

of a threshold system, a low sampling frequency will always introduce a bias that can increase the measured delay. Finally, there are two causes for an inherent bias to longer delays, independent of those mentioned, in a simple threshold system. First, no matter how ideal is the emitted pulse from the transducer, there will always be a rise time for the signal when it is detected. Second, and more importantly, the decision of where to set the threshold is a compromise that introduces bias [30]–[32].

- **Curve-fitting method**

An alternative method is the curve fitting method that produces an unbiased TOF measurement. In this technique, a nonlinear least-squares method is employed to fit a curve to the onset of the received echo. A parabolic curve of the form  $a_0(t - t_0)^2$  is fitted to the signal envelope around the rising edge of the echo [38]–[40]. First, initial estimates of the two parameters  $a_0$  and  $t_0$  are obtained: the initial estimate for  $t_0$  is found by simple thresholding, and  $a_0$  is estimated from the second derivative approximation around the threshold point. These are used to initialize an iterative numerical procedure: the Levenberg–Marquardt nonlinear least-squares method [41].

The authors of [40] have employed a simpler but less robust version of curve-fitting that does not require the nonlinear interactive fitting procedure: Two different threshold levels  $\tau_1$  and  $\tau_2$  ( $\tau_2 > \tau_1$ ) are set, and the vertex of the parabola passing through the two signal samples at which  $\tau_1$  and  $\tau_2$  are exceeded is found as:

$$t_0 = \frac{\sqrt{\tau_2/\tau_1} t_1 - t_2}{\sqrt{\tau_2/\tau_1} - 1} \quad (19)$$

$$\text{Such as: } \tau_1 = a_0(t_1 - t_0)^2 \quad \text{and} \quad \tau_2 = a_0(t_2 - t_0)^2 \quad (20)$$

Here,  $t_1$  and  $t_2$  are the time samples at which  $\tau_1$  and  $\tau_2$  are exceeded. The curve-fitting estimation reduces/eliminates the bias inherent to threshold method by using of a larger portion of the signal [32].

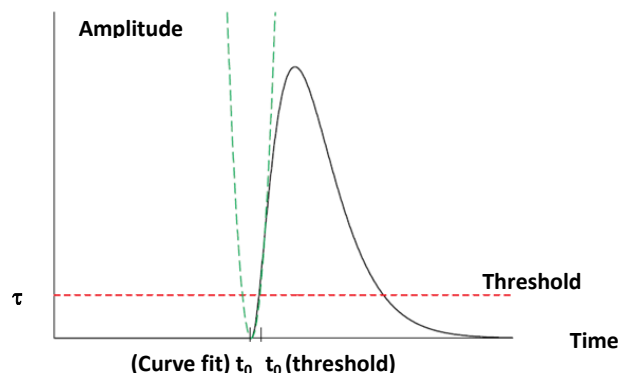


Figure 26: Envelope of an ultrasonic echo and TOF measurement by thresholding and curve fitting [32].

- **Cross-correlation method**

A more suitable TOF estimation technique is the cross-correlation [30], [33]–[37]. Here, the transmitted and received signals are cross-correlated. The TOF can be estimated when the correlation result reaches its maximum. Comparing with the threshold and the curve fitting techniques, the cross correlation works well with low SNR signals, and it is less affected by low-sampling rate problems [42]. It uses all the information contained in the signals; therefore, it is considered [43] as an optimum TOF estimator technique. The accuracy here depends mainly on the sampling rate.

In this study, the signal's TOF is evaluated using the cross correlation method. This technique takes the first series of echoes reflected inside the delay line (transmitted signal  $x(t)$ ) and the second series of echoes reflected on the plate surface (received signal  $y(t) \sim x(t - \tau_0)$ ) and then produces a time-domain signal whose maximum occurs at the delay time  $\tau_0$  (see Figure 30). The time resolution and accuracy of the received signal's TOF is particularly improved by calculating the cross-correlation function of two series of echoes (see figure 25 & 27) instead of two echoes (transmitted and received echoes) and by improving the sampling frequency of signal processing.

The cross correlation  $R_{xy}(t)$  of the sequences  $x(t)$  and  $y(t)$  is defined by the following equation:

$$R_{xy}(t) = x(t) \otimes y(t) = \int_{-\infty}^{\infty} x(\tau) \cdot y(t + \tau) d\tau \quad (16)$$

where the symbol  $\otimes$  denotes correlation.

Due to the level saturation of the transmitted signal, the experimental first series of echoes was replaced by the simulated one (the blue curve in Figure 23). The cross correlation result is shown in Figure 27.

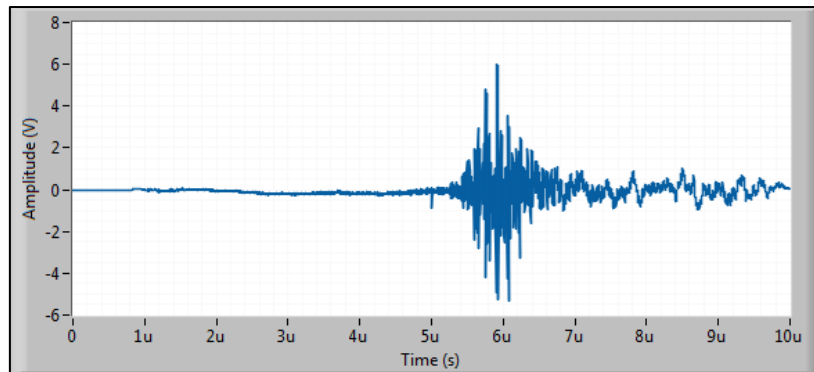


**Figure 27: The experimental cross-correlation pulse. The TOF is estimated when the correlation result reaches its maximum.**

The cross correlation measures the similarity between the first and the second series of echoes as a function of the lag of one relative to the other. The wave amplitude of the cross correlation result increases according to the degree of similarity between the two series, and then reaches the peak matching the point in time where the signals are best aligned. Then the wave amplitude decreases when the series are less similar. The wave peaks depend on the transducers structure, such as the time interval between these peaks corresponds to the delay line thickness. After calculating the cross-correlation, the time delay between the two signals is determined by the argument of the maximum with a time resolution of 10 ns.

### **XI. Conclusion**

This chapter presents a specific high frequency ultrasonic device, radiation resistant, allowing the measurement of fuel plates' swelling, i.e. the water channel thickness variations, inside a High Flux Reactor. It contains two ultrasonic transducers inserted at the end of a blade. With a total thickness of 1 mm, the device is further attached to a cylindrical holder to be manipulated from a distance of the order of 5 meters below the water surface. To allow a precise monitoring of the fuel element evolution, a resolution of a micron is searched while the dimension between the plates is close to the millimeter. To achieve this expected resolution, the system is excited with frequencies up to 120 MHz and integrated into a set of high frequency acquisition instruments. At these high frequencies, the multilayer structure of the transducers plays a central role in the shape of transmitted and received signals, hence the need to model the wave propagation inside these structures. The developed model is based on the transfer matrix method.

After manufacturing the high frequency transducers, their structures have been controlled by the acoustic microscopy to make visible images of their internal features, including the flatness of layers and defects such as cracks, delaminations and voids.

Based on the pulse-echo method, this device allows distance measurements through the signal's time of flight  $t$  (TOF) estimation. Several methods are available. The method most frequently used by sonar ranging systems is threshold detection. It is simple, but produces a biased estimate. To eliminate this bias, a parabolic fit method, which provides a parabolic fit to the leading edge of the echo envelope, was proposed. It has zero bias, but large variance. The optimum method for estimating time-of-flight is the correlation detection, since this makes use of all information in the signals. Therefore, to estimate the signal's TOF ( $t$ ), a signal processing using the cross-correlation method has been developed. It relates the distance  $d$  between fuel plates to the speed of sound  $v$  in the medium (water), through the simple equation  $d=c \times t/2$ . An obvious difficulty in applying this equation is the variability of  $v$  with temperature. In order to achieve accurate temperature measurement of the water channel, we introduce a new technique which is based on the resonance frequency change of transducers. This technique, described in the next chapter, has the advantage to use the same transducers for both measuring the thickness and the temperature of the water channel.

### List of Figures

Figure 1: General principle of inter-plate distance measurement. ....	51
Figure 2: Ultrasonic emission characteristics.....	52
Figure 3: Ultrasonic transducer.....	52
Figure 4: Schematic representation of the Multiple Ultrasonic Reflection in the interface delay line/ air.....	54
Figure 5: Schematic representation of the Multiple Ultrasonic Reflection in the interface delay line/ water .....	54
Figure 6: The modeled multilayer structure. ....	57
Figure 7: An ultrasound pulse: (a) the temporal signal; (b) the spectrum pulse. ....	59
Figure 8: Simulation of the temporal signal.....	60
Figure 9: The transducer simulation shows two series of echoes: (a) reflection of the signals within the multilayer structure of the transducer; (b) the receipt of the dual series after propagation in the water channel and reflection on the fuel plate; TOF is the time elapsed between the two series of echoes.....	60
Figure 10: The vacuum chamber.....	61
Figure 11: The coating metals. ....	61
Figure 12: the delay line and piezoelectric element samples.....	61
Figure 13: Polishing of the piezoelectric element.....	62
Figure 14: Piezoelectric element bonded to the delay line .....	62
Figure 15: One end of the high frequency ultrasonic device.....	63
Figure 16: Acoustic microscopy image of the interface support - piezoelectric element .	63
Figure 17: Acoustic microscopy image of the interface support - piezoelectric element .	64
Figure 18: the ultrasonic sensor.....	64
Figure 19: Connection system.....	65
Figure 20: Upper end of the Measurement saber (both sides) .....	65
Figure 21: block diagram of the distance measurement system.....	65
Figure 22: The first series of echoes. The time interval between echoes is related to the delay line thickness. ....	67
Figure 23: First series of echoes. Dash line (blue) corresponds to the simulated signal. Continuous line (red) corresponds to the experimental signal .....	68
Figure 24: The second series of echoes. The time interval between echoes is related to the delay line thickness. ....	68
Figure 25: Second series of echoes. Dash line (blue) corresponds to the simulated signal. Continuous line (red) corresponds to the experimental signal. ....	69
Figure 26: Envelope of an ultrasonic echo and TOF measurement by thresholding and curve fitting [32].....	70
Figure 27: The experimental cross-correlation pulse. The TOF is estimated when the correlation result reaches its maximum. ....	71

### Reference

- [1] A. S. Morris, *Measurement and instrumentation principles*. Oxford [England] ; Boston: Butterworth-Heinemann, 2001.
- [2] D. L. Arenberg, « Ultrasonic Solid Delay Lines », *J. Acoust. Soc. Am.*, vol. 20, n° 1, p. 1-26, janv. 1948.
- [3] I. L. Auerbach, J. P. Eckert, R. F. Shaw, et C. B. Sheppard, « Mercury Delay Line Memory Using a Pulse Rate of Several Megacycles », *Proc. IRE*, vol. 37, n° 8, p. 855-861, août 1949.
- [4] A. E. Benfield, A. G. Emslie, H. B. Huntington, Massachusetts Institute of Technology, et Radiation Laboratory, *On the theory and performance of liquid delay lines*. Cambridge, Mass.: Radiation Laboratory, Massachusetts Institute of Technology, 1945.
- [8] A. L. Zijlstra and C. M. van der Burgt, « ISOPAUSTIC GLASSES FOR ULTRASONIC DELAY LINES IN COLOUR TELEVISION RECEIVERS AND IN DIGITAL APPLICATIONS », *Ultrasonics* January 1967.
- [6] V. Cereser Camara et D. Laux, « Moisture content in honey determination with a shear ultrasonic reflectometer », *J. Food Eng.*, vol. 96, n° 1, p. 93-96, janv. 2010.
- [5] Russell W. Mebs, John H. Darr, and John D. Grimsley, "Metal Ultrasonic Delay Lines", *Journal of research of the National Bureau of Standards*. Vol. 51, No.5, November 1953.
- [8] H. B. Huntington, A. G. Emslie, et V. W. Hughes, « Ultrasonic delay lines. I. », *J. Frankl. Inst.*, vol. 245, n° 1, p. 1-23, janv. 1948.
- [4] A. G. Emslie and R. L. McConnell, *Radar system engineering*, 1, chap. 16 (McGraw-Hill Book Co., Inc., New York, N. Y., 1947).
- [10] M. Amini, T. Coyle, et T. Sinclair, « Porous ceramics as backing element for high-temperature transducers », *IEEE Trans. Ultrason. Ferroelectr. Freq. Control*, vol. 62, n° 2, p. 360-372, févr. 2015.
- [11] F. El-Tantawy et Y. K. Sung, « A novel ultrasonic transducer backing from porous epoxy resin-titanium-silane coupling agent and plasticizer composites », *Mater. Lett.*, vol. 58, n° 1-2, p. 154-158, janv. 2004.
- [12] S. K. Jain, R. Gupta, et S. Chandra, « Evaluation of acoustical characteristics of ultrasonic transducer backing materials at high hydrostatic pressures », *Ultrasonics*, vol. 36, n° 1-5, p. 37-40, févr. 1998.
- [13] N. T. Nguyen, M. Lethiecq, B. Karlsson, et F. Patat, « Highly attenuative rubber modified epoxy for ultrasonic transducer backing applications », *Ultrasonics*, vol. 34, n° 6, p. 669-675, août 1996.
- [14] R. W. King, *Transducer backing material*. Google Patents, 1997.
- [15] C. R. Trzaskos, "Ultrasonic transducer and process to obtain high acoustic attenuation in the backing," U.S. Patent 4382201 A, May 3, 1983.
- [16] M. J. S. Lowe, « Matrix techniques for modeling ultrasonic waves in multilayered media », *IEEE Trans. Ultrason. Ferroelectr. Freq. Control*, vol. 42, n° 4, p. 525-542, juill. 1995.
- [17] J. S. Sastry et M. L. Munjal, « A transfer matrix approach for evaluation of the response of a multi-layer infinite plate to a two-dimensional pressure excitation », *J. Sound Vib.*, vol. 182, n° 1, p. 109-128, 1995.
- [18] M. Lam, E. Le Clézio, H. Amorín, M. Algueró, J. Holc, M. Kosec, A. C. Hladky-Hennion, et G. Feuillard, « Acoustic wave transmission through piezoelectric structured materials », *Ultrasonics*, vol. 49, n° 4-5, p. 424-431, mai 2009.
- [19] W. T. Thomson, « Transmission of Elastic Waves through a Stratified Solid Medium », *J. Appl. Phys.*, vol. 21, n° 2, p. 89-93, févr. 1950.

## Chapter II: The high frequency ultrasonic device

---

- [20] N. A. Haskell, « The dispersion of surface waves on multilayered media », *Bull. Seismol. Soc. Am.*, vol. 43, n° 1, p. 17-34, janv. 1953.
- [21] D. L. Folds et C. D. Loggins, « Transmission and reflection of ultrasonic waves in layered media », *J. Acoust. Soc. Am.*, vol. 62, n° 5, p. 1102-1109, nov. 1977.
- [22] C.-M. Lee et Y. Xu, « A modified transfer matrix method for prediction of transmission loss of multilayer acoustic materials », *J. Sound Vib.*, vol. 326, n° 1-2, p. 290-301, sept. 2009.
- [23] P. Cervenka et P. Challande, « A new efficient algorithm to compute the exact reflection and transmission factors for plane waves in layered absorbing media (liquids and solids) », *J. Acoust. Soc. Am.*, vol. 89, n° 4, p. 1579-1589, avr. 1991.
- [24] M. L. Munjal, « Response Of A Multi-layered Infinite Plate To An Oblique Plane Wave By Means Of Transfer Matrices », *J. Sound Vib.*, vol. 162, n° 2, p. 333-343, avr. 1993.
- [25] B. Hosten, « Bulk heterogeneous plane waves propagation through viscoelastic plates and stratified media with large values of frequency domain », *Ultrasonics*, vol. 29, n° 6, p. 445-450, nov. 1991.
- [26] R. J. da Fonseca, L. Ferdj-Allah, G. Despaux, A. Boudour, L. Robert, et J. Attal, « Scanning Acoustic Microscopy—recent applications in materials science », *Adv. Mater.*, vol. 5, n° 7-8, p. 508-519, 1993.
- [27] K. K. Liang, S. D. Bennett, B. T. Khuri-Yakub, et G. S. Kino, « Precise Phase Measurements with the Acoustic Microscope », *IEEE Trans. Sonics Ultrason.*, vol. 32, n° 2, p. 266-273, mars 1985.
- [28] P. R. Hoskins, K. Martin, et A. Thrush, « *Diagnostic Ultrasound: Physics and Equipment* ». Book, Cambridge University Press, 2010.
- [29] « PXI Platform - National Instruments ». [En ligne]. Disponible sur: <http://www.ni.com/pxi/>. [Consulté le: 17-sept-2015].
- [30] J. C. Jackson, R. Summan, G. I. Dobie, S. M. Whiteley, S. G. Pierce, et G. Hayward, « Time-of-flight measurement techniques for airborne ultrasonic ranging », *IEEE Trans. Ultrason. Ferroelectr. Freq. Control*, vol. 60, n° 2, p. 343-355, févr. 2013.
- [31] T. M. Frederiksen et W. M. Howard, « A single-chip monolithic sonar system », *IEEE J. Solid-State Circuits*, vol. 9, n° 6, p. 394-403, déc. 1974.
- [32] B. Barshan, « Fast processing techniques for accurate ultrasonic range measurements », *Meas. Sci. Technol.*, vol. 11, n° 1, p. 45, janv. 2000.
- [33] A. Ş. Sekmen et B. Barshan, « Estimation of object location and radius of curvature using ultrasonic sonar », *Appl. Acoust.*, vol. 62, n° 7, p. 841-865, juill. 2001.
- [34] C. Knapp et G. C. Carter, « The generalized correlation method for estimation of time delay », *IEEE Trans. Acoust. Speech Signal Process.*, vol. 24, n° 4, p. 320-327, août 1976.
- [35] W. Jinjin, Y. Dong, et C. Ping, « Range resolution of ultrasonic distance measurement using single bit cross correlation for robots », in *2010 IEEE International Conference on Information and Automation (ICIA)*, 2010, p. 917-923.
- [36] Y. XU, Y. LI, Z. QU, S. JIN, et C. JIANG, « A TOF Estimation Method for Underwater Acoustic Signal in Confined Underwater Space\* », *J. Comput. Inf. Syst.*, vol. 8, n° 4, p. 1689-1696, 2012.
- [37] R. Queiros, F. C. Alegria, P. S. Girao, et A. C. Serra, « Cross-Correlation and Sine-Fitting Techniques for High-Resolution Ultrasonic Ranging », *IEEE Trans. Instrum. Meas.*, vol. 59, n° 12, p. 3227-3236, déc. 2010.

## Chapter II: The high frequency ultrasonic device

---

- [38] B. Barshan et R. Kuc, « A bat-like sonar system for obstacle localization », *Syst. Man Cybern. IEEE Trans. On*, vol. 22, n° 4, p. 636–646, 1992.
- [39] B. Barshan et R. Kuc, « ROBAT: A sonar-based mobile robot for bat-like prey capture », in *Robotics and Automation, 1992. Proceedings., 1992 IEEE International Conference on*, 1992, p. 274–279.
- [40] W. G. MaMullen, B. A. Delaughe, et J. S. Bird, « A simple rising-edge detector for time-of-arrival estimation », *Instrum. Meas. IEEE Trans. On*, vol. 45, n° 4, p. 823–827, 1996.
- [41] W. H. Press, Éd., *Numerical recipes in C: the art of scientific computing*, 2nd ed. Cambridge ; New York: Cambridge University Press, 1992.
- [42] M. Parrilla, J. J. Anaya, et C. Fritsch, « Digital signal processing techniques for high accuracy ultrasonic range measurements », *IEEE Trans. Instrum. Meas.*, vol. 40, n° 4, p. 759-763, août 1991.
- [43] K. Nakahira, T. Kodama, S. Morita, et S. Okuma, « Distance measurement by an ultrasonic system based on a digital polarity correlator », *IEEE Trans. Instrum. Meas.*, vol. 50, n° 6, p. 1748-1752, déc. 2001.



---

---

## Chapter III

### Temperature & velocity measurements

---

## *Summary*

I.	Introduction.....	80
II.	Temperature measurement.....	80
1.	Techniques of temperature measurement.....	80
2.	Resonant frequency change: the most relevant technique.....	81
3.	The experimental set-up.....	84
4.	Results.....	85
III.	Velocity measurement.....	87
1.	Principle.....	87
2.	The experimental set-up.....	88
3.	Results.....	88
IV.	Estimation of the experimental uncertainty.....	89
V.	Conclusion.....	92
	List of Figures.....	93
	Reference.....	94

## I. Introduction

The high frequency ultrasonic device described in the previous chapter allows distance evaluation through the ultrasonic wave time of flight (TOF) measurements. An obvious difficulty in applying this measurement is the variability of the speed of sound in the propagation medium with temperature. Therefore, to ensure the reliability of the distance measurement, the present chapter deals with the development of a technique allowing the measurement of the water channel temperature. While contact [1] or optical [2], [3] methods can be found in the literature, we propose a new technique based upon the analysis of the spectral components of an acoustic signal that propagates inside the developed transducer structure, the dimensions of this latter varying with thermal expansion [4].

An experimental set-up measuring the propagation velocity of the ultrasonic wave in water according to the temperature was developed in order to evaluate the performance of the high frequency ultrasonic device. Various methods have already been successfully proposed to determine the ultrasonic velocity dependence to the temperature [5]–[9]. They require the knowledge of the thickness of the tested solid or liquid or other information from which the thickness can be derived. Then, from the time-of-flight measurements, the sound-speed can be deduced at a given temperature. Based on a similar principle, the experimental set-up allows the evaluation of the speed of sound in water contained in a tank, whose width is previously defined. Results are then compared to the literature [10], demonstrating thus the accuracy of the ultrasonic device.

This chapter has been divided into two sections, the first one dealing with the temperature measurement system. In this section, a brief state-of-the-art of the temperature measurement techniques is reported. Then the principle, the computer simulation, and the experimental results of our technique for measuring the water channel temperature are presented. Section 2 gives a detailed description of the experimental set-up that allows the identification of the ultrasonic velocity in water dependence to the temperature.

## II. Temperature measurement

### 1. Techniques of temperature measurement

Temperature measurement in today's industrial environment encompasses a wide variety of needs and applications. To meet this wide array of needs, the industry has developed a large number of sensors and devices. Devices to measure temperature can be divided into two separate categories: contact and non-contact probes. The frequently used devices allowing a contact are thermocouples [11]–[14], and thermal resistances [16],[15]. The non-contact temperature sensor category includes a wide variety of primarily optical devices.

- **Thermocouples:**

The thermocouples principle is as follow: When two conductors made from dissimilar metals are connected forming two common junctions and the two junctions are exposed to two different temperatures, an electric current is produced [11]–[14].

- **Thermal resistance:**

Metallic conductor's resistance increases with temperature, while that of semiconductors generally decreases with temperature. Resistance thermometers employing metallic conductors for temperature measurement are called *Resistance Temperature Detector (RTD)*, and those employing semiconductors are termed as *Thermistors* [16],[15].

- **Optical devices**

Optical measurements involve the detection of light. Any parameter that changes with temperature, for example, changes in emission intensity, lifetime, optical path length or phase of an electromagnetic wave can be used to estimate the sample temperature. Optical techniques commonly used for temperature measurements are infrared thermography [17]–[19], fluorescence thermography [20], [21] and optical interferometry [22]–[24].

To summarize, each technique previously listed for measuring temperatures has its own advantages and disadvantages. Indeed, the RDT advantages include high accuracy, low drift, wide operating range (from  $-200$  to  $650$  °C), and suitability for precision applications. Moreover, RTDs are more rugged and have more or less linear characteristics over a wide temperature range. However, a standard RTD sheath is 3.175 to 6.35 mm in diameter [25]. Therefore, it cannot be immersed between fuel plates, spaced of 1.8 mm.

The advantages of thermistors are similar to or the same as those for RDTs, except that the RDTs are less sensitive to small temperature changes and have a slower response time. However, thermistors have a smaller temperature range and stability with nonlinear characteristics. Another drawback is that thermistors are fragile and therefore require delicate handling and mounting [11].

The thermocouples can measure temperatures over wide ranges from  $-180$  to  $2,320$  °C. They are very rugged, with diameters less than 1.6 mm, but they are somewhat less accurate than RTDs and thermistors. Indeed, if a tolerance of  $2$  °C is acceptable and the highest level of repeatability is not required, a thermocouple will can be used [26].

Optical methods provide far-field non-contact temperature mapping and they are capable to map temperature distributions over relatively large areas. However, they can be cumbersome; therefore they cannot be inserted between fuel plates where space is very limited to perform temperature measurement along the water channel.

In order to achieve the water channel temperature measurements, with a high spatial resolution, a new technique is developed. Instead of using a contact probe or an optical probe, this new technique is based upon the resonance frequency change of the transducers (presented in the previous chapter) according to the temperature. The most advantage of this technique is to make possible simultaneous measurements of the water channel's distance and temperature.

### **2. Resonant frequency change: the most relevant technique**

No standard systems can be used to perform temperature measurements along the water channel between two high-irradiated fuel plates with difficult access constraints. The developed device (presented in the previous chapter) has been used to address this issue. This device enables temperature changes to be translated into frequency changes. Indeed, the

## Chapter III: Temperature and Velocity measurements

---

spectral components of the acoustic signal that propagates inside the transducer structure changes according to the temperature.

When immersed into the water channel, the sensor temperature variation leads to a thermal expansion of its multi-layered structure, yielding in particular modifications of the layers dimensions. Among these layers the piezoelectric element, whose thermal expansion greatly influences the acoustic signal. The other transducer layers have either negligible thicknesses or negligible thermal expansion coefficient compared to the one of the piezoelectric element. Indeed, thicknesses of the glue, the chrome and the gold layers are less than 5 $\mu$ m. Moreover, the thermal expansion coefficient of the silica layer is equal to 4.1 10<sup>-7</sup>/C° [3], [27] while that of the piezoelectric element is equal to 14.10<sup>-4</sup>/C°[28]. As a result, the transducer resonance frequency is mainly related to the piezoelectric element thermal expansion. This expansion induces a thermal variation of the piezoelectric element thickness and variation of the sound speed. These two parameters are related to the resonance frequency of the transducer according to:

$$f = \frac{v}{2d}. \quad (6)$$

where  $v$  is the ultrasonic velocity of the piezoelectric element. Therefore, the frequency variation  $\Delta f/f$  can be expressed as:

$$\frac{\Delta f}{f} = \frac{\Delta v}{v} - \frac{\Delta d}{d}. \quad (7)$$

The sound velocity in solids is equal to  $v = \sqrt{\frac{E}{\rho}}$  where,  $E$  is the young modulus and  $\rho$  is the piezoelectric element density. Thus, the velocity variation  $\Delta v/v$  can be written as:

$$\frac{\Delta v}{v} = \frac{1}{2} \left( \frac{\Delta E}{E} - \frac{\Delta \rho}{\rho} \right). \quad (8)$$

Therefore the frequency variation  $\Delta f/f$  is equal to:  $\frac{\Delta f}{f} = \frac{1}{2} \left( \frac{\Delta E}{E} - \frac{\Delta \rho}{\rho} \right) - \frac{\Delta d}{d}$ . (9)

The young modulus can be expressed in terms of the compliance constants (or elastic moduli)  $S_{11}$ , as follows:  $E = \frac{1}{S_{11}}$  [29]. This means that:  $\frac{\Delta E}{E} = -\frac{\Delta S_{11}}{S_{11}}$ . (10)

Equation (10) indicates that  $\Delta f/f$  depends on the expansion  $\Delta d/d$ , on the density variation  $d\rho/\rho$ , and on the elastic constant variation  $\Delta S_{11}/S_{11}$ .

The piezoelectric element thickness  $d$  increases when it is heated at constant pressure, according to the thermal expansion law [30]:

$$\Delta d = \alpha \times \Delta T \times d(T_0). \quad (11)$$

where  $\alpha$  is the linear thermal expansion coefficient. Therefore, the expansion  $\Delta d/d$  can be written as:

$$\frac{\Delta d}{d} = \frac{\alpha \Delta T}{1 + \alpha \Delta T} \quad (12)$$

## Chapter III: Temperature and Velocity measurements

In the case of lithium niobate, the elastic constant temperature derivative is expressed as follows [31]:

$$\frac{\Delta S_{11}}{S_{11}} = a \Delta T \quad (13)$$

where  $a = 1.66 \cdot 10^{-4}/^{\circ}\text{K}$ .

It is well known that the density is defined by the ratio:  $\rho = \frac{m}{V}$  measured in  $\text{kg}/\text{m}^3$ . At the temperature  $T_0$ , the density is equal to:  $\rho_0 = \frac{m}{V_0}$ .

At a given temperature  $T$ , the volume of solid materials is expressed as [32]:

$$V = V_0(1 + \gamma\Delta T) \quad (14)$$

where  $\gamma$ , measured in  $^{\circ}\text{C}^{-1}$  or  $\text{K}^{-1}$ , is the volume expansion coefficient [33].

$$\text{So: } \rho = \frac{m}{V_0(1+\gamma\Delta T)} = \frac{\rho_0}{1+\gamma\Delta T} \quad (15)$$

Therefore the density variation  $d\rho/\rho$  can be written as:

$$\frac{\Delta\rho}{\rho} = -\gamma\Delta T \quad (16)$$

From (12), (13) and (16) equations, the frequency variation  $\Delta f/f$  is expressed as:

$$\frac{\Delta f}{f} = -\frac{a \Delta T}{2} + \frac{\gamma\Delta T}{2} - \frac{\alpha\Delta T}{1+\alpha\Delta T} \quad (17)$$

A simulation based on the last equation was developed to observe the effect of the temperature change on the transducer's resonance frequency (see Figure 1).

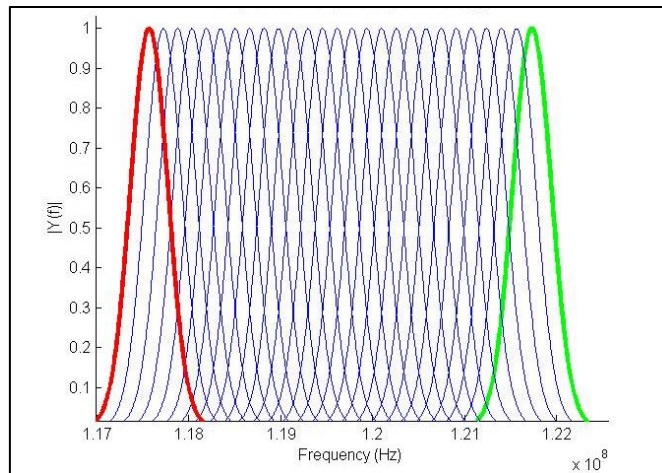


**Figure 1: Frequency spectrum of the ultrasonic sensor immersed in water at temperatures ranging from 10 °C to 40 °C. The green curve corresponds to the frequency spectrum at 10 °C and the red one represents the spectrum frequency at 40°C.**

As most research reactors, the High Flux Reactor operates at low temperatures ( $<100^{\circ}\text{C}$ ) and during in-situ measurements, the water pool temperature doesn't exceed  $35^{\circ}\text{C}$ . For this

## Chapter III: Temperature and Velocity measurements

reason, computer simulations and experiments presented later in this report have been performed in temperature range from 10 °C to 40 °C.

The Figure 1 shows that when the transducer is heated, its resonance frequency decreases. This frequency decrease is about 4.2 MHz when the temperature ranges from 10 °C to 40 °C. Therefore, the frequency evolution is 3.54% over 30 °C which corresponds to a frequency variation of 0.11%/°C.

As well known, the measurement resolution is proportional to the transducer resonance frequency which is temperature dependent. Therefore, when temperature ranges from 10 °C to 40 °C, the measurement resolution varies of 0.3%/°C, this value being computed from the estimation of the wavelength variation with the temperature.

The transducer resonance frequency change was then evaluated experimentally. Values were determined after the settling time of the transducer temperature estimated of one second.

### 3. The experimental set-up

The experimental set-up requires the use of an electronic chain of instruments (see Figure 2). It includes the high frequency ultrasonic device, the PXI platform described in the previous chapter (including the pulse generator, the controller system, amplifiers and the acquisition board), a thermostatic bath (HUBER CC-K12), and a signal acquisition and processing software.

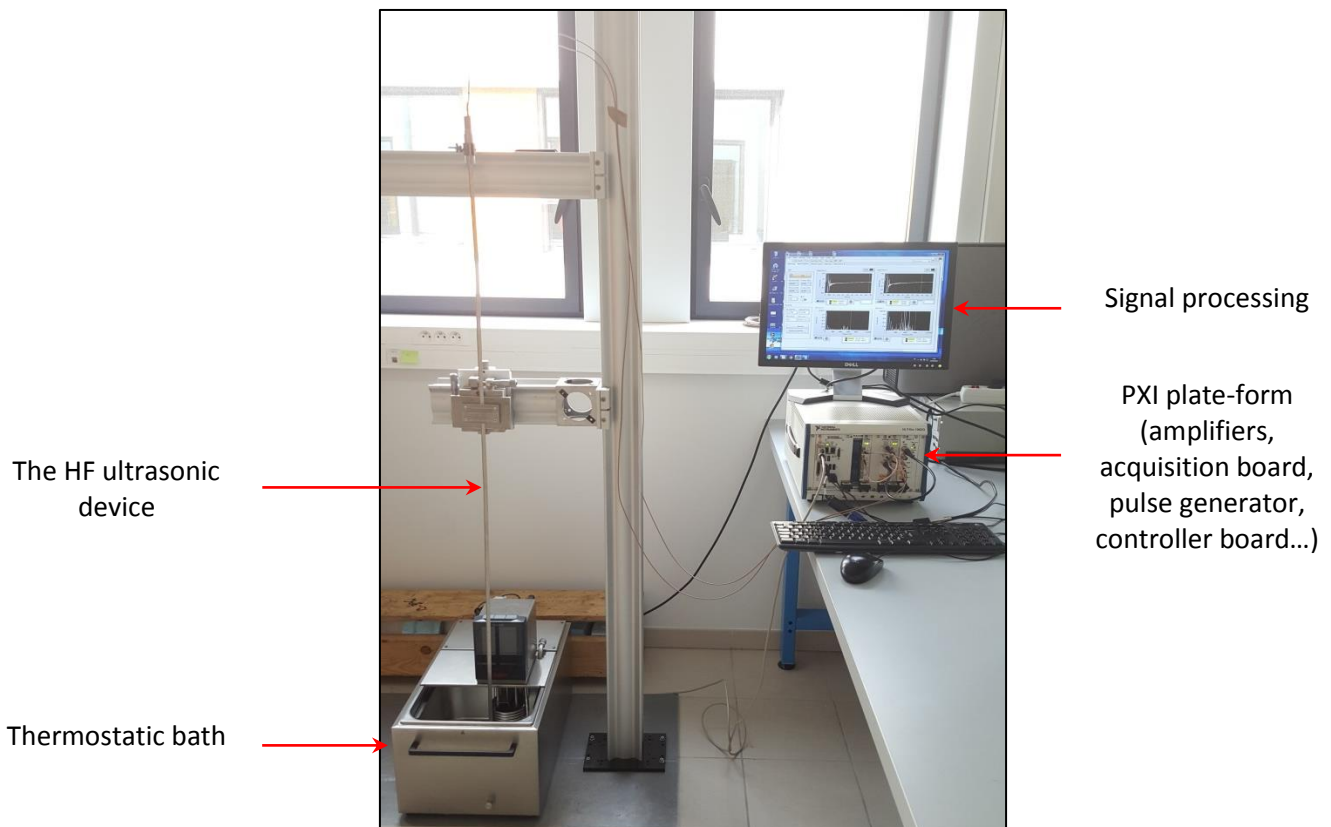


Figure 2: The experimental set-up for temperature measurement.

The temperature was controlled via a refrigerated-heating bath with air-cooled refrigeration unit. The temperature control bath performs typical heating and cooling tasks at

## Chapter III: Temperature and Velocity measurements

temperatures ranging from  $-20$  to  $200^{\circ}\text{C}$  with a stability of  $\pm 0.02^{\circ}\text{C}$  which induces an ultrasonic velocity uncertainty of  $\pm 0.05$  m/s and thus an uncertainty on distance measurement of  $\pm 0.12$   $\mu\text{m}$ . The thermostatic bath has a circulating pump that guarantees an optimum stirring of the bath and the temperature homogeneity. It was controlled by a program developed on the NI LabVIEW software (see Appendix 4).

The proposed measurement system operates as follows: First the ultrasonic device was immersed in deionized water contained in the thermostatic bath. Then it was excited by the pulse generator. The generated ultrasound wave propagates through the sensor multilayered structure, resulting in echoes reflected from interfaces. These echoes are then amplified, filtered, sampled at a 2.5 GS/s frequency and displayed to be processed.

To perform temperature measurements, the thermostatic bath regulates the water temperature at the initial value ( $T_0 \approx 10^{\circ}\text{C}$ ). Once the temperature is stabilized, an echo (non-saturated and non-overlapped) is selected from the received signal. The peak of its frequency spectrum corresponds to the transducer resonance frequency. The peak value is then stored at the temperature  $T_0$ . Knowing that the transducer response time is about one second, the same process is then repeated by heating water up to  $40^{\circ}\text{C}$  by steps of  $0.2^{\circ}\text{C}$ . At each step an average of 10 acquisitions is calculated. At the end, the measurement system displays the resonance frequency variations at temperatures ranging from  $10^{\circ}\text{C}$  to  $37^{\circ}\text{C}$  (see Figures 3).

### 4. Results

The results of the experimental set-up are shown in Figure 3. Here, the frequency variation for both transducers included in the blade sensor is evaluated in the temperature range [ $10^{\circ}\text{C}$  -  $37^{\circ}\text{C}$ ]. The experimental results were compared with simulated values to evaluate the accuracy of the measurement system.

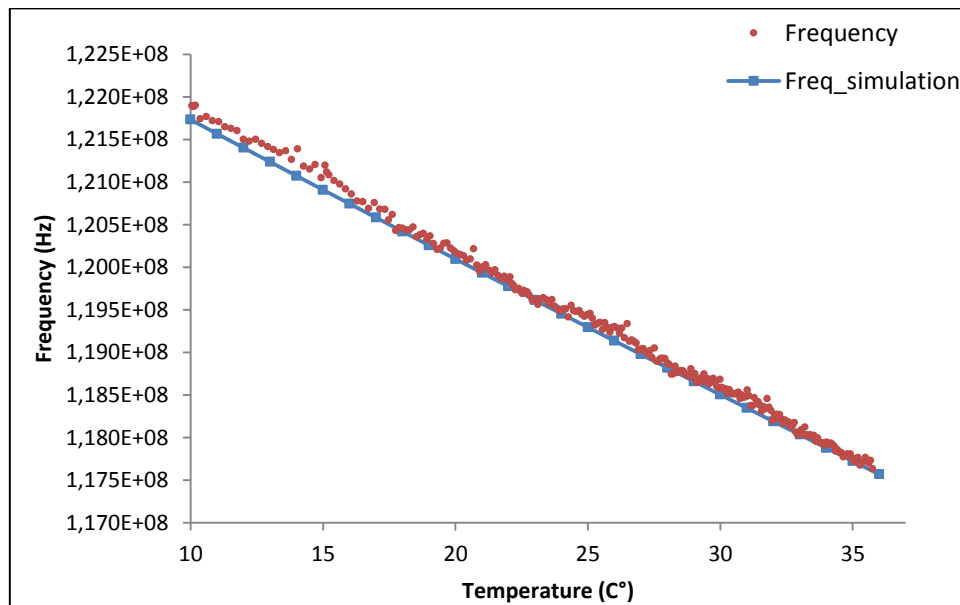


Figure 3: Transducer 1 frequency variation according to the temperature. Blue squares correspond to the simulated values and red points to the experimental values.

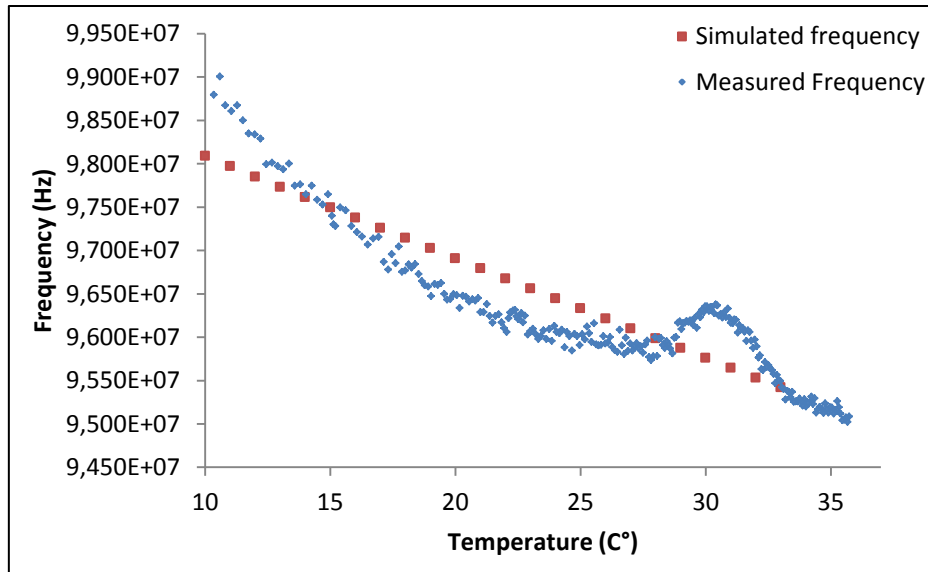


Figure 4: Transducer 2 frequency variation according to the temperature. Red squares correspond to the simulated values and blue points to the experimental values.

The resonance frequency of the first transducer (Figure 3) presents a stable behavior with decreasing values from 121.9 MHz at 10 °C to 117.7 MHz at 36 °C. A maximum difference with the simulated values of 0.2 MHz is observed around 15 °C.

The second transducer has, however, an unstable behavior (Figure 4). A decrease of 3.7 MHz in the transducer resonance frequency was observed, when water was heated from 10 °C to 37 °C. A large difference between the experimental and the simulated values was observed between 15 °C and 28 °C, and then around 30 °C, such as the maximum difference was about 0.6 MHz. The cause of this large variation is being studied but is not yet understood. Therefore, the water channel temperature measurement is based, in the following, upon the simulated resonance frequency change (red square in Figure 3).

To check the feasibility and perform quantitative measurements of the water channel temperature, series of measurements were carried out on ILL spent fuel elements. During this experiment, the sensor has been positioned between two fuel plates, and then it slid along the water channel to perform continuous measurements. From the measured transducer frequency and by referring to the frequency variation law  $f(T)$  presented in Figure 8, the water temperature was deduced.

The feasibility of such challenging temperature measurement has already been proved, and thermal information of two water channels has been deduced. The results and the experiment feedbacks are presented and discussed in the next chapter.

### III. Velocity measurement

#### 1. Principle

The evaluation of the high frequency ultrasonic device, developed for distance and temperature measurements, was performed under laboratory conditions (without radiative flux) to check the device accuracy as well as its possible error sources during measurements. The proposed system deals with the determination of the ultrasonic velocity in water according to the temperature.

Traditionally, the measurement of ultrasonic wave propagation velocity is carried out by measuring the time necessary for the wave to complete a known path; or by the "sing around" technique, in which the ultrasonic pulse, after having completed the known path, is utilized to re-trigger the transmitter [34]. Thus, the system has an ultrasonic pulse digit period dependent on the velocity and the length of the path that the wave must cover inside the medium. To achieve high accuracy in velocity measurements it is necessary to know precisely the length of the ultrasonic path. The percentage error committed on measurements of the path length recurs in the same percentage in the estimation of velocity [35].

The method proposed here is based on the classical technique where time of flight measurements is performed along known reference distances [4]. During the calibration process, home-made tanks with controlled thicknesses were used as reflectors (Figure 5). First the device was positioned inside a tank which is filled with pure water. Then, transducers which are set on the opposite sides of device send a high frequency ultrasonic wave that radiates in their silica delay line. These radiations generate echoes that propagate in water before being reflected on the tank walls. Reciprocally, the transducers receive the acoustic signal. The time-of-flight (TOF) is then estimated from the maximum peak time in the cross-correlation function of the first series of echoes (radiation in the delay line) and the second one (reflection on the tank walls). The ultrasonic velocity is, thus, deduced from the TOF of the acoustic signal according to:

$$v = 2 \times \frac{d_{\text{tank}} - d_{\text{sensor}}}{TOF_{\text{transducer1}} + TOF_{\text{transducer2}}} \quad (18)$$

Where  $d_{\text{tank}}$  is the known tank thickness,  $d_{\text{sensor}}$  is the sensor thickness of about 1mm and  $TOF_{\text{transducer}}$  is the time of flight of the acoustic wave measured by each transducer.

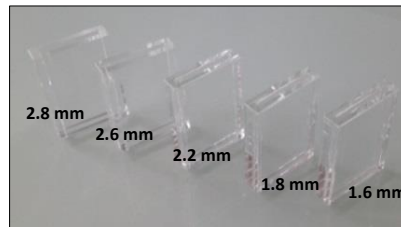
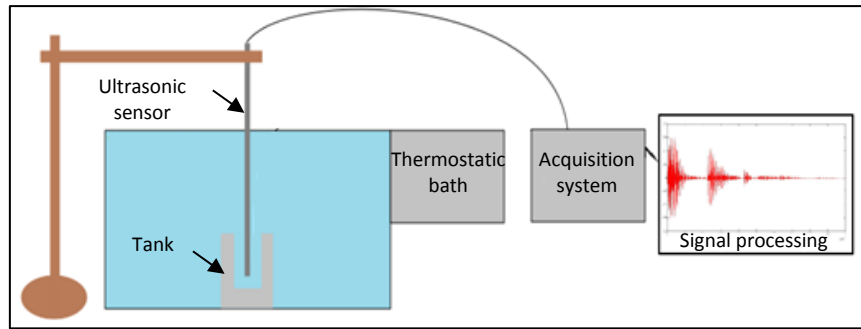


Figure 5: Quartz reflectors with different thicknesses.

Measurements were performed in tanks having different widths from (1.8 mm and 2.5 mm) and by heating water from 10°C to 40 °C. At the end, experimental results, presented in the following section, are compared to the literature [10] to evaluate the accuracy of the ultrasonic device and to identify the different sources of errors.

## 2. The experimental set-up

The proposed system is basically the same as that used for temperature measurement (see Figure 6). In this case, the ultrasonic sensor was placed inside the quartz tank by using a position control system. The tank was immersed in the thermostatic bath (HBER CC-K12) which is capable of regulating the temperature with a 0.02 °C resolution. It regulates and maintains the temperature via the thermostatic bath pump which stirs the water to ensure a uniform temperature in the medium. The bath was filled by deionized water similar to that of the reactor.



**Figure 6: Platform of sound speed measurement**

First, the transducer is immersed in a tank to save acoustic signals at temperatures ranging from 10 °C to 40 °C. Signals were acquired each 50 ms and they were used to find the ultrasonic propagation speed in water from the time-of-flight measurements. The propagation speed results were averaged for each 10 measurements and the standard deviation was calculated. The same experiment is then repeated in a larger tank.

## 3. Results

The experimental results of the sound velocity variation according to the temperature are shown in Figure 7. Measurements performed in the first tank ( $d_1=1.8 \pm 0.01$  mm) are marked with red square and those performed in the second tank ( $d_2=2.5 \pm 0.01$  mm) are marked with green triangles. The experimental results were then compared to the literature [10]. Theoretically, the sound speed in water was calculated according the following law:

$$C = a_0 + a_1T + a_2T^2 + a_3T^3 + a_4T^4 + a_5T^5 \quad (19)$$

Such as:

Coefficients ( $a_i$ )	Values
$a_0$	+ 1.40238689E + 3
$a_1$	+ 5.03686088E + 0
$a_2$	- 5.80858499E- 2
$a_3$	- 3.34817140E- 4
$a_4$	- 1.49252527E- 6
$a_5$	+ 3.23913472E-9
<b>Max error m/s</b>	<b>0.002</b>
<b>Temp range °C</b>	<b>0–100</b>

**Table 1: The coefficients of the fifth-order polynomial used to calculate  $v(m/s)$  in water according to the temperature [10].**

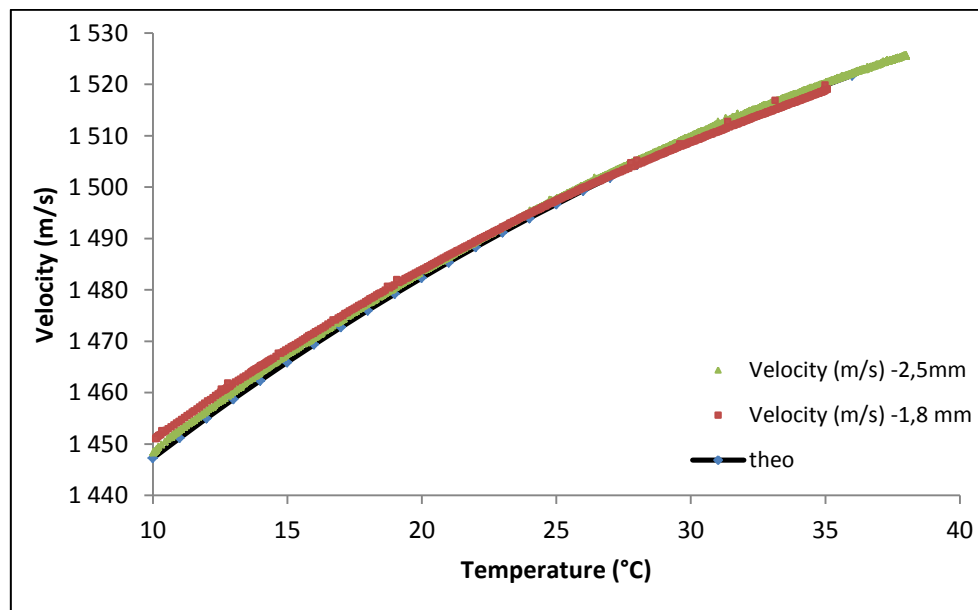


Figure 7: ultrasonic velocity in water as a function of the temperature. Theoretical values are marked with black line.

As mentioned above, the propagation speed results were averaged each 10 measurements and the maximum standard deviation was 0.73 m/s at 25 °C with the first tank (1.8 mm width) and 0.71 m/s at 25 °C with the second tank (2.5 mm width).

The Figure 7 shows that the measurement system produced appropriate values compared to the data reported by [10]. Indeed, the experimental results present an upward behavior with values from 1450 m/s at 10 °C to 1530 m/s at 38 °C having a maximum difference of 4m/s at 11 °C with the theoretical values. The average difference between both states of the experimental results (for  $d_1=1.8$  mm and  $d_2=2.5$  mm) was 1.55 m/s with a maximum difference value of 2.2 m/s at 10 °C.

#### IV. Estimation of the experimental uncertainty

In the previous experiments, several parameters have been identified as possible causes of uncertainty on the final estimation of the measured distance. Error sources can be summarized in the following points:

- **Influence of the transducer resonance frequency change according to the temperature:**

As mentioned in the previous section of this chapter, by heating the water from 10 °C to 40 °C, a decrease of 0.11%/°C of the transducer resonance frequency was observed. This variation has, however, an effect on the measurement resolution which varies also of 0.3%/°C.

The variation of the resonance frequency according to the temperature has also an effect on the ultrasonic wave time of flight estimation. Indeed, a ToF error of 0.1% was observed when the temperature ranges from 10 °C to 40 °C (see Figure 8). This calculus has been

## Chapter III: Temperature and Velocity measurements

made only by varying the frequency from 121.9MHz ( $T = 10^\circ\text{C}$ ) to 117.7 MHz ( $T = 40^\circ\text{C}$ ). The ultrasonic velocity and distance were kept constants.

- **Error due to tanks' tolerance:**

The ultrasonic velocity measurement errors can also be related to tanks' tolerance of about  $\pm 10\mu\text{m}$ . These two sources of errors (tank's tolerance error and ToF error) may cause a maximum error of the ultrasonic velocity measurement of 0.65% in the temperature range [ $10^\circ\text{C}$ ;  $40^\circ\text{C}$ ].

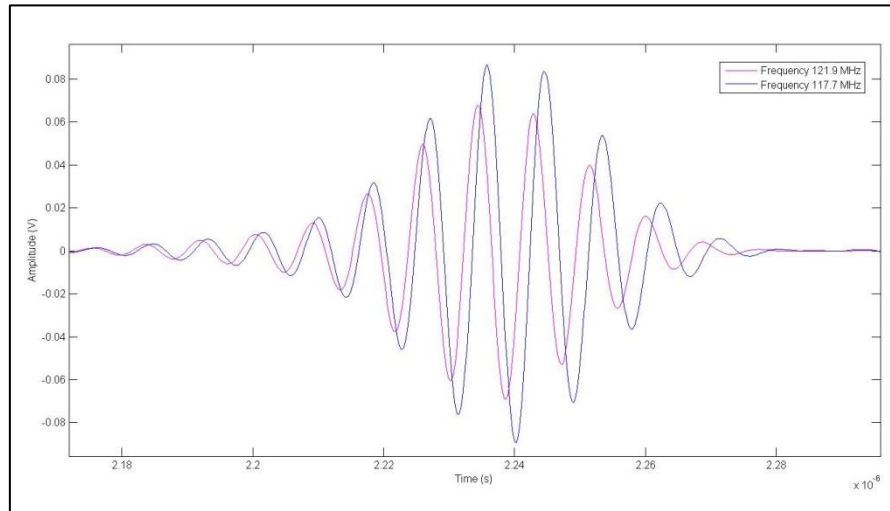


**Figure 8: the ToF variation according to the temperature. The blue curve corresponds to the echo waveform at frequency equal to 121.7 MHz ( $T = 10^\circ\text{C}$ ) and the purple curve corresponds to the echo waveform at frequency equal to 117.9 MHz ( $T = 40^\circ\text{C}$ ).**

Errors related to the ultrasonic wave time of flight estimation and the ultrasonic velocity measurements lead to an error in distance measurement of 0.74% (which corresponds to  $\Delta d = 13.5\mu\text{m}$  for  $d = 1.8\text{mm}$ ).

- **Error related to the thermostatic bath:**

The thermostatic bath performs typical heating and cooling tasks with a stability of  $\pm 0.02^\circ\text{C}$  which induces an ultrasonic velocity uncertainty of  $\pm 0.05\text{m/s}$  and thus an uncertainty on distance measurement of  $\pm 0.12\mu\text{m}$ .

Moreover, due to the thermostatic bath pump, vibrations of the tanks and movement in the water can be induced. That can affect the ultrasonic signals used for the speed of sound calculus. To eliminate this effect, speed of sound measurements can be performed with the thermostatic bath off. Indeed, due to the thermostatic bath inertia, temperature does not change as the shutdown time is short.

- **Error related to the non-parallelism of the ultrasonic device to the tank walls:**

The measurement error can also occur when transducers are not perfectly parallel to the tank walls. To quantify the influence of this non-parallelism on the ultrasonic signal, a simulation based on the transfer matrix method is developed to understand wave propagation in non-plane structures. When transducers are perfectly parallel to the plates, the receipt signal is maximal, i.e. multiple reflections on the plates can be acquired (see Figure 10). By increasing the inclination, the echoes reflected on the plates arrive with a delay and low amplitude (see Figure 9). Therefore, this causes inter-plate distance measurement errors (see Figure 11).

## Chapter III: Temperature and Velocity measurements

In the case of the fuel plates, knowing the radius of the fuel plate curvature, the inter-plate distance, and the blade thickness (1 mm), the maximum inclination possible of the transducer has been estimated to be less than  $3^\circ$ . This inclination can cause an error of distance measurement of  $4\ \mu\text{m}$  (see Figure 11).

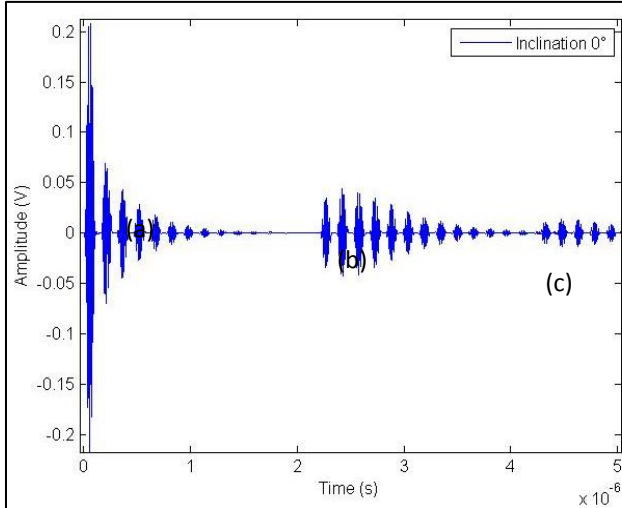


**Figure 9:** The second series of echoes with inclination of  $5^\circ$  in the delay line, (b) and (c) are, reciprocally, the first and second reflections in the facing plate.

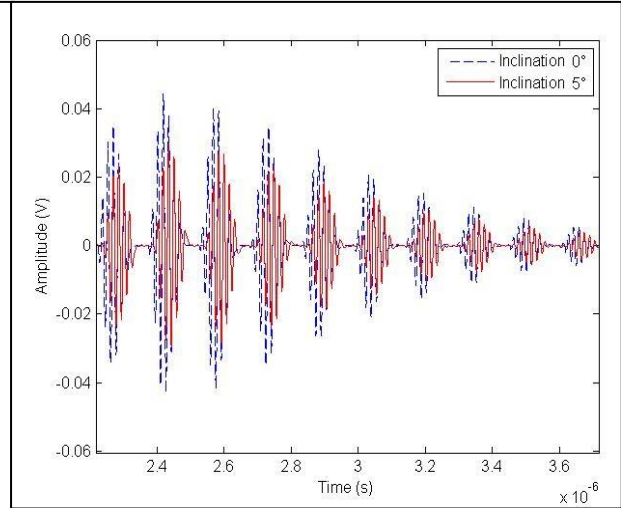


**Figure 10:** The second series of echoes with inclination of  $5^\circ$ .

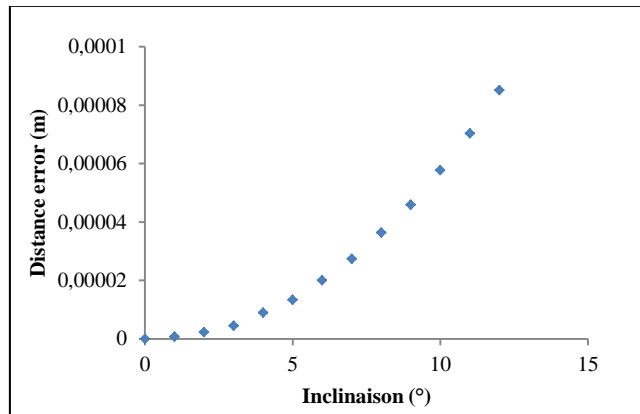


**Figure 11:** Distance error depending on the inclination of the transducer relative to the plate.

To address this issue, measurements must be performed only when the receipt signal is maximal for both transducers at the same time. A second solution, which is being studied, consists on drilling a small hole on the delay line of silica in order to create an acoustic lens. This solution aims to focus the acoustic waves in order to compensate the possible angular discrepancy between the silica glass surface and the fuel plates.

To conclude, the main errors sources and their influences on distance measurements are shown in Table 2.

Error sources	Distance measurement error
Frequency variation according to the temperature + tank tolerance ( $\pm 10 \mu\text{m}$ )	$\pm 13.5 \mu\text{m}$
The thermostatic bath stability ( $\pm 0.02 \text{ }^\circ\text{C}$ )	$\pm 0.12 \mu\text{m}$
Error related to the non-parallelism of the ultrasonic device to the tank walls (max $3^\circ$ )	$\pm 4 \mu\text{m}$
<b>Total error estimation</b>	<b><math>\pm 18 \mu\text{m}</math></b>

Table 2: Errors sources and theirs influences on distance measurements.

The above table summarizes the identified sources of errors on the distance measurements. They lead to an ill-estimation of less than 0.8%, rounded to 1% in the table. This means that, in our experiments, the total error on the inter-plate distance estimation is less than  $20 \mu\text{m}$ .

## V. Conclusion

The distance measurement accuracy depends upon the ultrasonic wave's time of flight and velocity in the water channel. The ultrasonic velocity is temperature dependent. Therefore, measuring the water channel temperature was necessary to perform accurate measurements. Nowadays no standard technique is yet available to measure water temperature flowing between two close fuel plates, highly irradiated and immersed 5 m underwater.

To address this issue, a system allowing thermal monitoring from the analysis of the spectral components of our ultrasonic transducer was designed (presented in the second chapter). Indeed, the water temperature variation induces a thermal expansion of the transducer layers, yielding in particular modifications of piezoelectric element dimensions. As a result, the transducer resonance frequency is related to the piezoelectric element thermal expansion. Therefore, it was proved through the proposed measurement system that the transducers resonance frequency decreases by approximately 4 MHz when water is heated from  $10 \text{ }^\circ\text{C}$  to  $40 \text{ }^\circ\text{C}$ . The experimental results and the simulated data were compared and they underwent the same behavior, with a slight difference of 0.2 MHz at  $15 \text{ }^\circ\text{C}$ , except for the second transducer having an unstable behavior. This behavior is being studied.

To check the performance of the developed ultrasonic device, the second section of this chapter deals with the identification of the temperature dependence of the ultrasonic velocity of waves propagating in water. To this aim, an experimental set-up was developed to perform speed of sound measurements in home-made tanks with controlled thicknesses. From the time-of-flight measurements, the speed of sound was deduced at temperature ranging from  $10 \text{ }^\circ\text{C}$  to  $38 \text{ }^\circ\text{C}$ . While being close to values proposed previously in the literature, the developed system indicates that the high frequency ultrasonic device is ready to perform distance and temperature measurements in the HFR fuel element.

The distance and temperature measurements techniques were then tested on a full size irradiated fuel element of the French High Flux Reactor (HFR). The feasibility of such challenging measurement has already been proved and the experimental constraints attached to measurement procedure have been identified.

### List of Figures

Figure 1: Frequency spectrum of the ultrasonic sensor immersed in water at temperatures ranging from 10 °C to 40 °C. The green curve corresponds to the frequency spectrum at 10 °C and the red one represents the spectrum frequency at 40C°. .....	83
Figure 2: The experimental set-up for temperature measurement. ....	84
Figure 3: Transducer 1 frequency variation according to the temperature. Blue squares correspond to the simulated values and red points to the experimental values.....	85
Figure 4: Transducer 2 frequency variation according to the temperature. Red squares correspond to the simulated values and blue points to the experimental values.....	86
Figure 5: Quartz reflectors with different thicknesses. ....	87
Figure 6: Platform of sound speed measurement .....	88
Figure 7: ultrasonic velocity in water as a function of the temperature. Theoretical values are marked with black line. ....	89
Figure 8: the ToF variation according to the temperature. The blue curve corresponds to the echo waveform at frequency equal to 121.7 MHz (T = 10 ° C) and the purple curve corresponds to the echo waveform at frequency equal to 117.9 MHz (T = 40 ° C). ....	90
Figure 9: The second series of echoes with inclination of 5°.....	91
Figure 9: The second series of echoes with inclination of 5°.ons in the delay line, (b) and (c) are, reciprocally, the first and second reflections in the facing plate.....	91
Figure 11: Distance error depending on the inclination of the transducer relative to the plate. ....	91

### Reference

- [1] Matthias Nau, "Mesure électrique de la température", Fulda, février 2003.
- [2] A. J. Crandall, B. D. Cook, et E. A. Hiedemann, « Measurement of the Velocity of Sound in Water by Optical Methods », *J. Acoust. Soc. Am.*, vol. 44, n° 1, p. 387-387, juill. 1968.
- [3] Xuefeng Li, Shuo Lin, Jinxing Liang, Yupeng Zhang, H. Oigawa, et T. Ueda, « Fiber-Optic Temperature Sensor Based on Difference of Thermal Expansion Coefficient Between Fused Silica and Metallic Materials », *IEEE Photonics J.*, vol. 4, n° 1, p. 155-162, févr. 2012.
- [4] G. Zaz, Y. Calzavara, E. Le Clézio, et G. Despau, « Adaptation of a High Frequency Ultrasonic Transducer to the Measurement of Water Temperature in a Nuclear Reactor », *Phys. Procedia*, vol. 70, p. 195-198, 2015.
- [5] I. Y. Kuo, B. Hete, et K. K. Shung, « A novel method for the measurement of acoustic speed », *J. Acoust. Soc. Am.*, vol. 88, n° 4, p. 1679-1682, oct. 1990.
- [6] P. Labes, J. L. Daridon, B. Lagourette, et H. Saint-Guirons, « Measurement and prediction of ultrasonic speed under high pressure in natural gases », *Int. J. Thermophys.*, vol. 15, n° 5, p. 803-819, sept. 1994.
- [7] P. Stanislav Mayevskyy, « Precise measurement of ultrasonic velocity », in *AIP Conference Proceedings*, 2001, vol. 557, p. 1587-1591.
- [8] S. C. Rogers et G. N. Miller, « Ultrasonic Level, Temperature, and Density Sensor », *IEEE Trans. Nucl. Sci.*, vol. 29, n° 1, p. 665-668, févr. 1982.
- [9] A. Briggs, *Acoustic microscopy*, 2nd ed. Oxford ; New York: Oxford University Press, 2010.
- [10] N. Bilaniuk et G. S. K. Wong, « Speed of sound in pure water as a function of temperature », *J. Acoust. Soc. Am.*, vol. 93, n° 3, p. 1609-1612, mars 1993.
- [11] J. A. Capp et L. T. Robinson, « Thermocouples and resistance coils for the determination of local temperatures in electrical machines », *Am. Inst. Electr. Eng. Proc. Of*, vol. 32, n° 3, p. 701-708, mars 1913.
- [12] J. Liu, L. Ma, et J. Yang, « Methods and techniques of temperature measurement », in *2011 International Conference on Electrical and Control Engineering (ICECE)*, 2011, p. 5332-5334.
- [13] C. Canali, G. De Cicco, B. Morten, M. Prudenziati, et A. Taroni, « A Temperature Compensated Ultrasonic Sensor Operating in Air for Distance and Proximity Measurements », *IEEE Trans. Ind. Electron.*, vol. IE-29, n° 4, p. 336-341, nov. 1982.
- [14] A. S. Morris, *Measurement and instrumentation principles*. Oxford [England] ; Boston: Butterworth-Heinemann, 2001.
- [15] S. Basu et A. Debnath, "Power Plant Instrumentation and Control Handbook: A Guide to Thermal Power Plants". Academic Press, 2014.
- [16] Lesson 4: Temperature Measurement, Version 2 EE IIT, Kharagpur.
- [17] R. Usamentiaga, P. Venegas, J. Guerediaga, L. Vega, J. Molleda, et F. Bulnes, « Infrared Thermography for Temperature Measurement and Non-Destructive Testing », *Sensors*, vol. 14, n° 7, p. 12305-12348, juill. 2014.
- [18] J. H. L. Ling, A. A. O. Tay, K. F. Choo, W. Chen, et D. Kendig, « Measurement of MMIC gate temperature using infrared and Thermorefectance thermography », in *Electronics Packaging Technology Conference (EPTC), 2012 IEEE 14th*, 2012, p. 515-518.
- [19] F. F. Farkhani et F. A. Mohammadi, « Temperature and power measurement of modern dual core processor by infrared thermography », in *Proceedings of 2010 IEEE International Symposium on Circuits and Systems (ISCAS)*, 2010, p. 1603-1606.

## Chapter III: Temperature and Velocity measurements

---

- [20] M. Harker, P. O'Leary, M. S. Kharicha, et S. Eck, « Calibration, Measurement and Error Analysis of Optical Temperature Measurement via Laser Induced Fluorescence », in *IEEE Instrumentation and Measurement Technology Conference Proceedings, 2007. IMTC 2007*, 2007, p. 1-6.
- [21] J. Sakakibara et R. J. Adrian, « Whole field measurement of temperature in water using two-color laser induced fluorescence », *Exp. Fluids*, vol. 26, n° 1-2, p. 7-15, 1999.
- [22] T. Kubota, M. Nara, et T. Yoshino, « Interferometer for measuring displacement and distance », *Opt. Lett.*, vol. 12, n° 5, p. 310-312, mai 1987.
- [23] R. Bommareddi, « Applications of Optical Interferometer Techniques for Precision Measurements of Changes in Temperature, Growth and Refractive Index of Materials », *Technologies*, vol. 2, n° 2, p. 54-75, mai 2014.
- [24] Geoff Jakins, "Fiber-optic temperature and positioning sensors", Mississippi State University.
- [25] « Resistance thermometer », *Wikipedia, the free encyclopedia*. 25-sept-2015.
- [26] P. Thermocouple, « The purpose of this application note is to explore the more common temperature measurement techniques, and introduce procedures for improving their accuracy. »
- [27] C. J. Bell, S. Reid, J. Faller, G. D. Hammond, J. Hough, I. W. Martin, S. Rowan, et K. V. Tokmakov, « Experimental results for nulling the effective thermal expansion coefficient of fused silica fibres under a static stress », *Class. Quantum Gravity*, vol. 31, n° 6, p. 065010, mars 2014.
- [28] A. Grisard, « Lasers guides d'onde dans le niobate de lithium dopé erbium », Université Nice Sophia Antipolis, 1997.
- [29] U. Rössler, *Solid State Theory: An Introduction*. Springer Science & Business Media, 2013.
- [30] F. Pignatiello, M. De Rosa, P. Ferraro, S. Grilli, P. De Natale, A. Arie, et S. De Nicola, « Measurement of the thermal expansion coefficients of ferroelectric crystals by a moiré interferometer », *Opt. Commun.*, vol. 277, n° 1, p. 14-18, sept. 2007.
- [31] R. T. Smith et F. S. Welsh, « Temperature Dependence of the Elastic, Piezoelectric, and Dielectric Constants of Lithium Tantalate and Lithium Niobate », *J. Appl. Phys.*, vol. 42, n° 6, p. 2219-2230, mai 1971.
- [32] J. D. James, J. A. Spittle, S. G. R. Brown, et R. W. Evans, « A review of measurement techniques for the thermal expansion coefficient of metals and alloys at elevated temperatures », *Meas. Sci. Technol.*, vol. 12, n° 3, p. R1, 2001.
- [33] S. C. Abrahams, H. J. Levinstein, et J. M. Reddy, « Ferroelectric lithium niobate. 5. Polycrystal X-ray diffraction study between 24° and 1200°C », *J. Phys. Chem. Solids*, vol. 27, n° 6-7, p. 1019-1026, juin 1966.
- [34] J. (Ed. . SZILARD, *Ultrasonic testing non-conventional testing techniques*. Chichester: John Wiley & Sons, 1982.
- [35] M. Sgalla et D. Vangi, « A device for measuring the velocity of ultrasonic waves: An application to stress analysis », *Exp. Mech.*, vol. 44, n° 1, p. 85-90, févr. 2004.

---

---

## Chapter IV

### Experiments on a real RHF spent fuel element

---

### Summary

I.	Introduction.....	98
II.	The first experiment on a full size irradiated fuel element of the RHF.....	98
1.	The experimental set-up .....	98
2.	Results and discussions .....	99
3.	Experimental feedback.....	100
III.	The second experiment on a full size irradiated fuel element of the RHF.....	101
1.	The experimental set-up .....	101
2.	Water pool temperature measurements.....	102
3.	Water channels temperature measurements.....	103
3.1	Temperature measurements of the first water channel.....	103
3.2	Temperature measurements of the second water channel.....	105
4.	Distance measurements before irradiations.....	107
5.	Water channel distance measurements post-irradiations.....	108
5.1	The first water channel thickness measurements post-irradiations.....	108
5.2	The second water channel thickness measurements post-irradiations.....	109
6.	Experimental feedbacks .....	111
IV.	Conclusion .....	114
	List of Figures .....	115
	Reference.....	116

### I. Introduction

Deeply engaged in the conversion process, the ILL has designed an optimized LEU fuel element, which is based upon the high density LEU fuel (UMo). Nevertheless, the UMo fuel is not yet experimentally validated [1]. Prior experiments have shown that dispersion UMo fuel can swell under irradiation [2]. Therefore, post irradiation examinations (PIE) of the new fuel element must be carried out in order to achieve the qualification process. One of the most relevant ways to examine the fuel plate swelling is to carry out inter-plate distance measurement using the high frequency ultrasonic device. However, these measurements were very difficult. Indeed, the fuel element was placed 4 m below the water surface. Therefore, to allow the access to the inter-plate space of 1.8 mm, a 5 m long stainless steel support was manufactured. The support dimensions make it heavy and thus difficult to handle by an operator which is held in a cradle. Moreover, all systems were under high radiations.

During this research project, the inter-plate distance measurements have already been assessed through two experiments carried out on fuel elements based upon the current HEU fuel UA1x. The experimental constraints were deducted at each experiment to improve the accuracy in the future works.

The first experiment where the fuel element was not totally spent proved the feasibility of such challenging measurement in a highly radioactive environment. It was demonstrated that the different components of the ultrasonic transducers showed good resistance to radiations. Moreover, the quality of the signal to noise ratio was clearly sufficient to get a very stable assessment of the inter-plate distance. Experimental constraints were also identified and the temperature dependence of the measure has been considered as an important parameter.

To improve the measurement reliability, these constraints have been considered in the second experiment performed within the RHF spent fuel element, more radioactive than the one used in the feasibility experiment. During this experiment, the first series of quantitative distance measurements were performed with an updated blade and the feasibility of the temperature measurements was proved. Measurements were carried out, for a long time, in higher radioactive environment. Some flaws may still have to be corrected to perform an absolute measurement in future works.

These two experiments will be detailed in this chapter. In the first section, the experimental set-up, the results and the feedbacks of the first experiments will be presented. In the second section, the water channel temperature measurements are presented, then the inter-plate distance evaluation, before and after radiation, is shown and discussed. At the end, the experimental constraints are identified.

## II. The first experiment on a full size irradiated fuel element of the RHF

### 1. The experimental set-up

To study the behavior of the fuel elements after irradiation, an in-situ experiment leading to a first measurement of the inter-plate distance within a fuel element of the RHF reactor was performed. This measurement should enable characterization of the plates swelling, inherent in the irradiation, as well as structural changes (corrosion, delamination ...). The objective of

## Chapter IV: Experiments on the real RHF spent fuel element

this experiment was to study the feasibility of the distance measurement technique. Therefore, the blade was introduced only for few centimeters between the fuel plates.

During measurements the fuel element was placed 4 meters under water. Distance measurements were made with a blade with the following dimensions: a thickness of 1 mm, a width of 16 mm and a length of 620 mm. This blade was handled by an operator with a 5 m long stainless steel support (see chapter II). The cable connecting the blade to the electronics had a length of 15 m. A camera under water, radiation resistant, was also used to get a picture of the working area.

First the transducers, operating at frequencies up to 70 MHz, were calibrated in the water pool. Then, the blade was slit to perform measures in the upper central portion of the element (see Figure 2). Signals were recorded every 50 ms and distances were calculated by a post-processing.

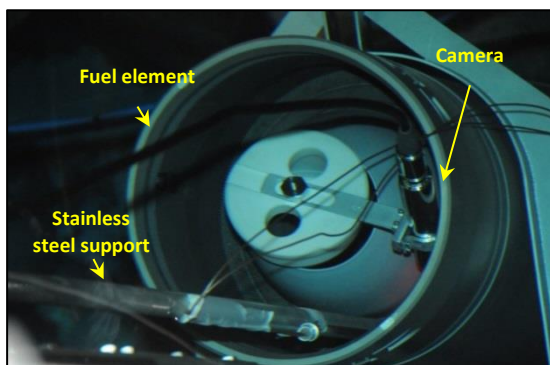


Figure 1: Positioning of the blade in the fuel element.

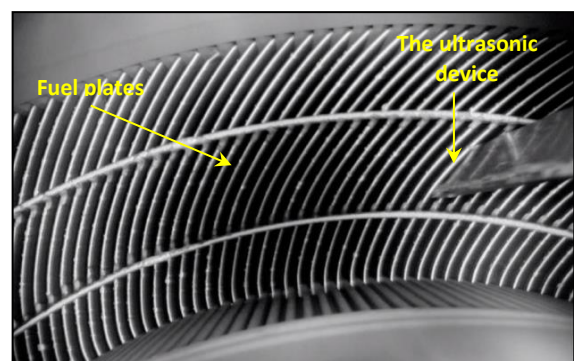


Figure 2: Positioning of the blade between two fuel plates.

## 2. Results and discussions

Once acquired, the acoustic signal is filtered to be used for inter-plate distance measurements (see Figure 3).

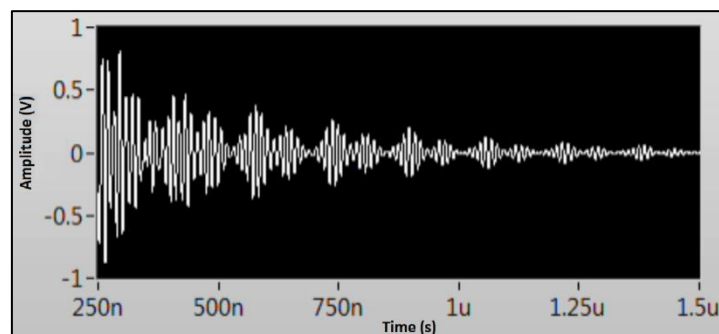


Figure 3: The first series of echoes of the acquired acoustic signal.

The Figure 3 clearly shows that despite the highly radioactive nature of the environment the quality of the ultrasonic signals was enough to ensure a stable identification of the inter-plate distances. However, due to the cable length, noise echoes appear in the signal. Moreover, the saturation of the first echoes is mainly due to the pulse generator that limits the received signal amplitude to protect the electronic system from high tension.

## Chapter IV: Experiments on the real RHF spent fuel element

The inter-correlation of the first series of echoes (radiations in the delay line) without saturated ones with the second series (reflection on the plate surface) leads to the ultrasonic wave's time of flight evaluation. Then, by knowing the sound speed in water and the blade thickness, the inter-plate distance was deduced. Figure 4 shows the results of this first experiment of distance measurement.

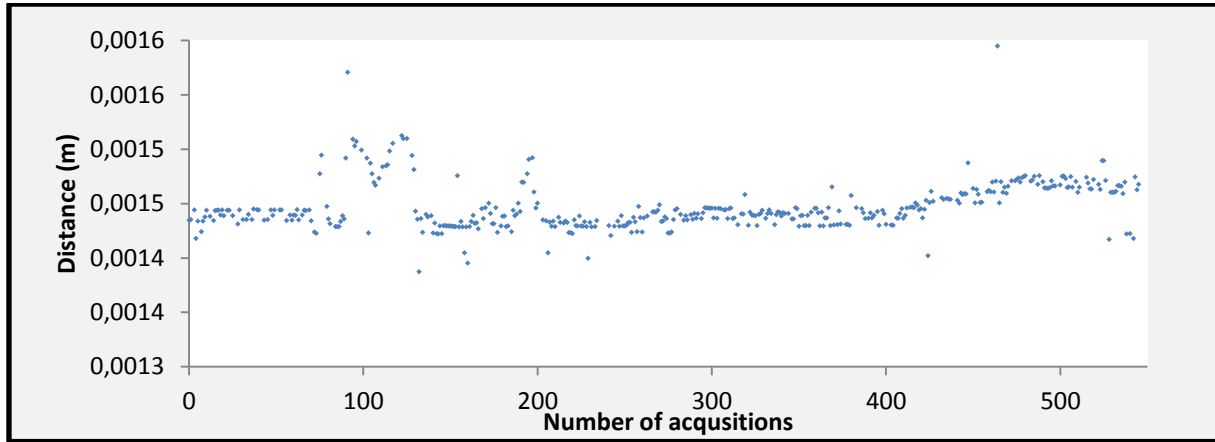


Figure 4: Experimental results of the first experiment in the RHF fuel element.

Several observations can be made from Figure 4. For the first 400 acquisitions, the relative distance was equal to  $1.44 \pm 0.005$  mm with a high stability. The difference between this value and the initially expected 1.8 mm can be related to the no-calibration of the ultrasonic device. In particular, some measurement errors can be related to an error of the blade thickness estimation that can yield a hundred micron ill-estimation. These parameters will be taken into account in the second experiment presented below. The large variations observable between the 80<sup>th</sup> and the 120<sup>th</sup> acquisition as well as around the 200<sup>th</sup> correspond to withdrawals of the sensors from the measurement areas and should not be considered as relevant. A slight increase of the distance ( $1.47 \pm 0.001$  mm) can be observed beyond acquisition 400 indicating a change in the thickness of the water channel.

### 3. Experimental feedback

The feasibility of the inter-plate distance measurement has been proved and relative values were obtained. Such measurements were, however, a real challenge due to the difficult access constraints to the space inter-plate and due to the highly radioactive environment. Measurements were performed in the middle radii of the fuel element and the blade was introduced only for few centimeters between fuel plates. Knowing that the transducers were subjected to 1000 gray/hour, this latter have resisted to radiation more than 4 hours. Moreover, the quality of the acoustic signal was very stable. At the end, the experimental constraints have been identified.

In order to introduce the blade along the water channel and into the three different radii (inner ring side, outer ring and the middle) of the fuel element, the blade dimensions were optimized. The thickness was kept at 1 mm while the width was reduced until 1 cm and the length was extended to 1.5 m (see Figure 5). The inner diameter of each transducer hosting hole was reduced to 6 mm with a spot facing, while the grooves were kept at the same dimensions. The blade material was 316L stainless steel.

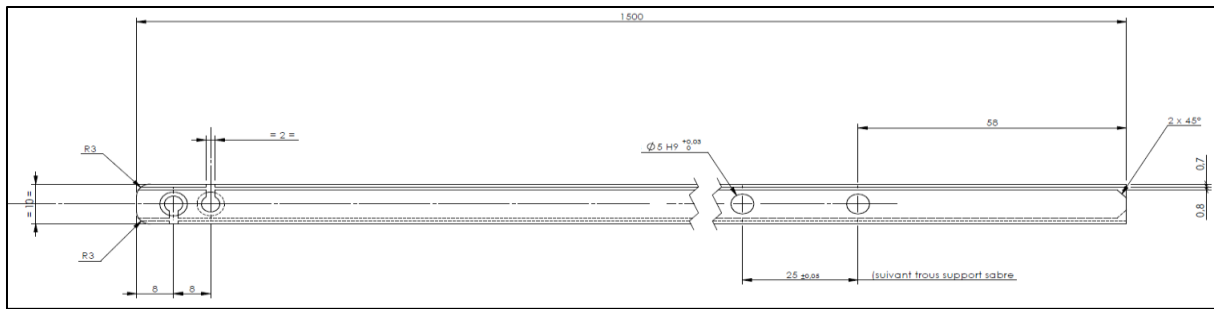


Figure 5: The updated drawing of the blade.

Both accuracy and resolution of distance measurement depend upon the water temperature variation. Indeed, in the previous chapter, it was proved that the measurement resolution can vary of  $0.3\%/^{\circ}\text{C}$  according to the temperature. Moreover, the accuracy of distance measurement is related to the ultrasonic wave time of flight estimation and the ultrasonic velocity in water. These two parameters are temperature dependent. Indeed, it was observed that the ultrasonic wave ToF can vary of  $0.1\%$  while the ultrasonic velocity varies of  $0.7\%$  when the temperature ranges from  $10^{\circ}\text{C}$  to  $40^{\circ}\text{C}$ . This variation is small, but as we are looking for the microscopic resolution ( $10\ \mu\text{m}$ ), these errors become significant. To this aim, a new technique was developed to measure the water channel temperature. This technique, which is based on the spectral components of ultrasonic transducers, is presented in the previous chapter.

To get quantitative measurements, a second series of experiments was performed by considering the experimental feedbacks. These new experiments were carried out on a real RHF spent fuel element and have led to a first series of quantitative measurements.

### III. The second experiment on a full size irradiated fuel element of the RHF

#### 1. The experimental set-up

A second in-situ experiment was carried out on a real RHF spent fuel element. The experimental set-up is basically the same as that of the first experiment (presented in previous section). The fuel element was set-up 4 m under water, and measurements were performed with the updated blade handled by an operator with a 5 m long stainless steel support. The cable connecting the blade to the electronics had a length of 15 m. Unlike the feasibility experiment where the blade was introduced for few centimeters between fuel plates, in the second experiment, measurements were performed in different water channels and the blade was introduced until almost half of the water channel.

At first the water pool temperature was measured. Then, series of distance and temperature measurements have been performed in three different water channels to check the repeatability of measurements, the radiation resistance of transducers (for a long time), the feasibility of temperature measurements and to get quantitative distance measurements. In this section distance and temperature measurements performed in two different water channels will be presented.

## Chapter IV: Experiments on the real RHF spent fuel element

In the first water channel (N° 75), the blade was introduced at a depth of 4 cm and by recording the acoustic signal, the blade was ascent progressively (see Figure 6, diagram at the right). While within the second water channel (N° 2), the blade was introduced at a depth of 30 cm. Then, by recording the acoustic signal every 50 ms, the operator brought out the blade in two stages (see Figure 6, diagram at the left):

- **Stage 1 (for the first 14 centimeters):** the operator brought out the blade by steps of 1 cm. At each step, the blade is stabilized to be perfectly parallel to the plates (by getting a maximum signal with both transducers) before performing measurements.
- **Stage 2 (for the last 16 centimeters):** the operator brought out the blade continuously.

The aim is to compare the two ways of measuring distance and to deduce the advantages and disadvantages of both methods. In both water channels (N° 75 and N° 2), the blade have been ascent manually. Therefore, we haven't any information about the speed of the ascent.

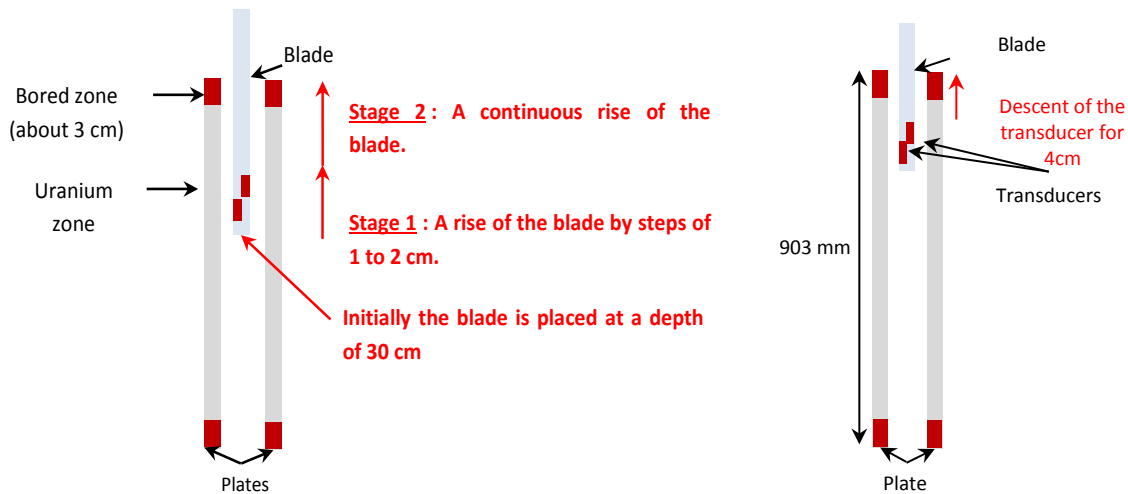


Figure 6: Left the blade positions within the first water channel and right the blade positions within the second water channel.

### 2. Water pool temperature measurements

Before introducing the blade between fuel plates, transducers were calibrated in the water-pool. The water pool temperature was deduced from the transducers resonance frequency (see Figure 8 & 10) and by referring to the frequency variation law presented in the previous chapter. The transducer resonance frequency is derived from the frequency spectrum of an echo (unsaturated, non-noisy and non-overlapped echo) selected from the first series of echoes (radiations in the delay line) see Figures 7 and 9.

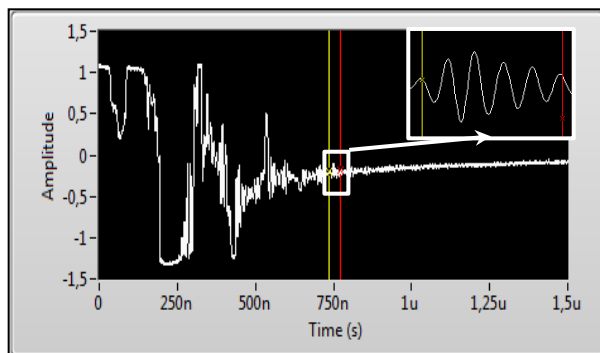


Figure 7: Transducer 1 temporal signal in the water pool of the reactor.

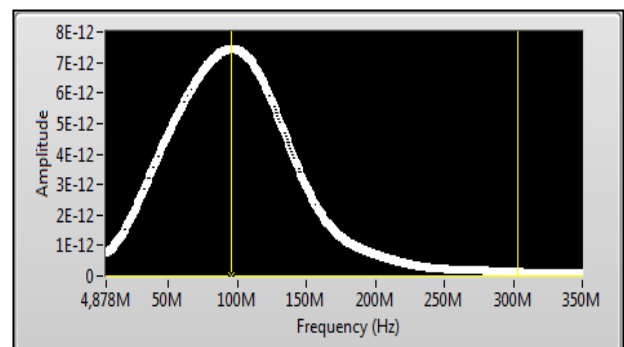
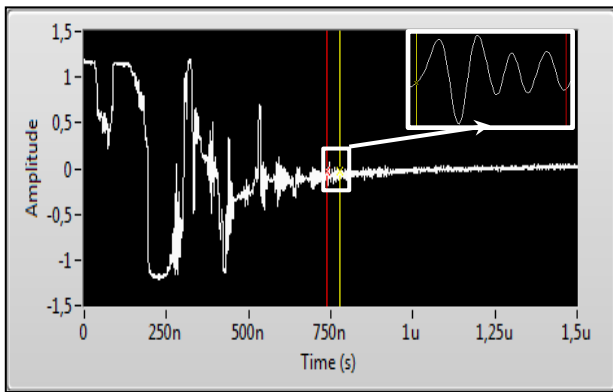
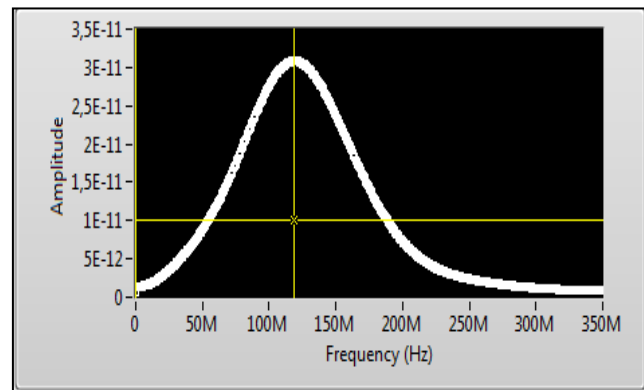


Figure 8: Transducer 1 frequency in the water pool of the reactor.



**Figure 9:** Transducer 2 temporal signal in the water pool of the reactor.



**Figure 10:** Transducer 2 frequency in the water pool of the reactor.

For the first transducer, the resonance frequency was equal to  $95.89 \pm 0.01$  MHz corresponding to a temperature of  $28.37 \pm 0.07$  °C. The measured temperature was near to the predefined one ( $T=28.3$  °C), such as the relative error was about 0.25%.

For the second transducer, the resonance frequency was equal to  $118.8 \pm 0.01$  MHz corresponding to a temperature of  $28.29 \pm 0.07$  °C. Therefore, the Measurement error was about 0.25% (such as  $\Delta T=0.07$  °C and the predefined value of the temperature was  $T=28.3$  °C). After the calibration step, the blade was then introduced into a water channel to perform, simultaneous, temperature and distance measurements.

### 3. Water channels temperature measurements

#### 3.1 Temperature measurements of the first water channel

Transducers' resonance frequency changes were evaluated by ascending the blade within the first water channel from a depth of 4 cm. Values were derived from the frequency spectrum of an echo reflected in the delay line (first series of echoes). This echo was unsaturated, rarely overlapped, and slightly influenced by the electrical noise due to the cable length.

As mentioned above, the blade was handled 5 m above the water surface and it was ascent manually. Therefore, the speed of the blade ascent was not controlled. The thermal time constant of the transducers is less than one second.

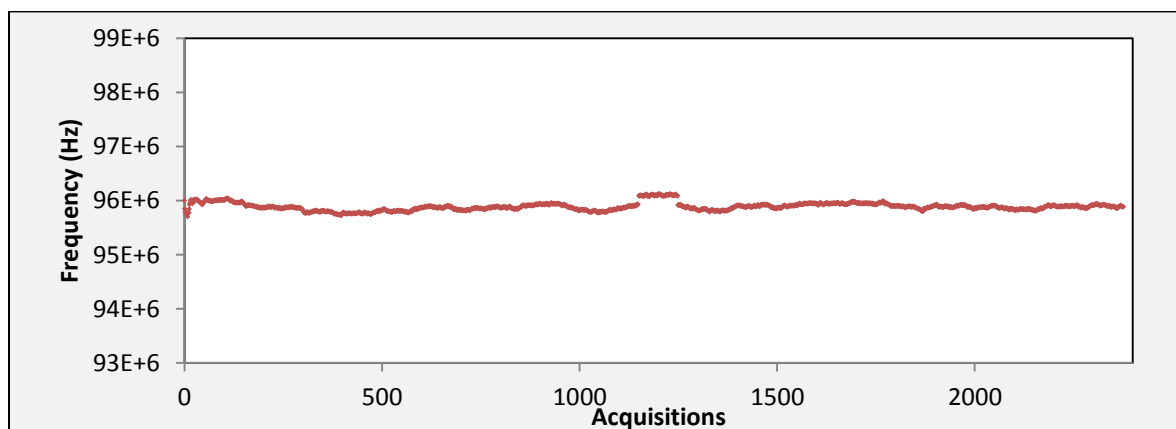


**Figure 11:** The first transducer frequency variation-values correspond to averages of 100 measured frequencies.

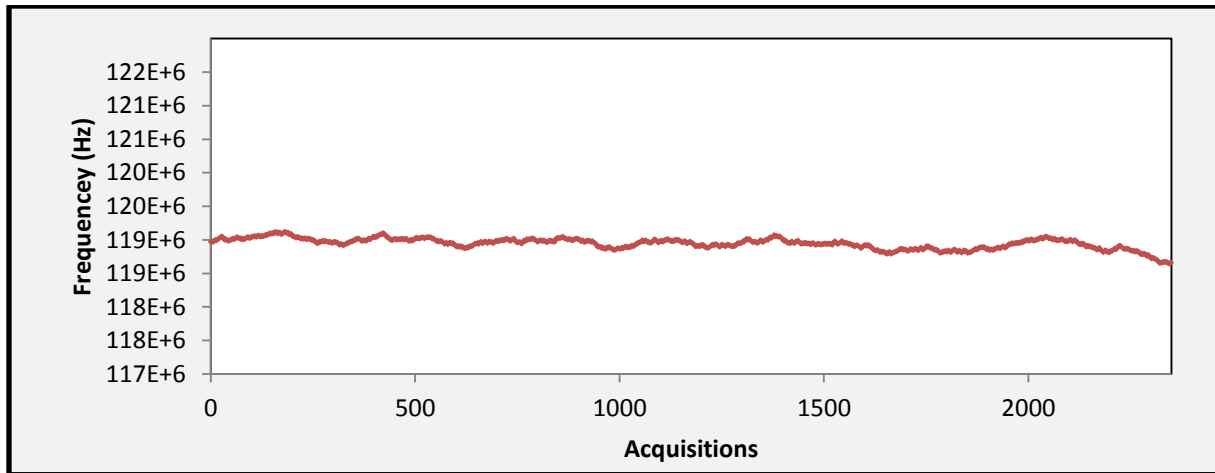


**Figure 12:** The second transducer frequency variation-values correspond to averages of 100 measured frequencies.

The Figures 11 and 12 show the transducers frequency variation, such as values correspond to averages of 100 measured frequencies. The first acquisition represents the transducer frequency at a depth of 4 cm of the water channel, while the last acquisition corresponds to the transducer frequency at the top of the plates. During this experiment, the average frequency measured by the first transducer was  $95.8 \pm 0.01$  MHz with a standard deviation of  $\sigma = 0.47$  MHz. A large frequency variation was also observed around the 1200<sup>th</sup> acquisition. For the second transducer, the average frequency was  $118.9 \pm 0.01$  MHz with a standard deviation of  $\sigma = 0.52$  MHz. The observed perturbations can be related to:

- The electrical noise caused by the length of the cables (about 15 m). Their spectral responses can be added to the transducer frequency.
- A slight overlap of the selected echo (used to evaluate the transducer frequency) with reflections on the plate. This overlap can be by moving the blade closer to the plate

According to frequency measurements shown in Figure 13, and by referring to the frequency variation law, the water temperature was deduced.

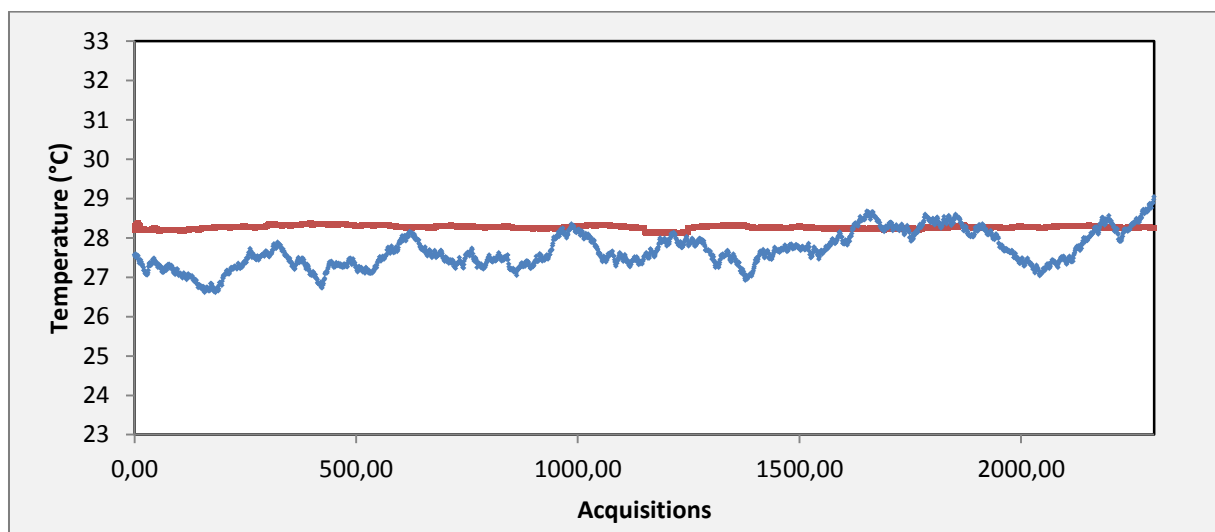


**Figure 13:** Transducers temperature measurement –the red line corresponds to the first transducer resonance frequency and the blue line to the second transducer resonance frequency – values correspond to averages of 100 acquisitions.

## Chapter IV: Experiments on the real RHF spent fuel element

Figure 13 shows a good stability of temperature measurements for the first transducer. The temperature average was about  $28.28 \pm 0.1$  °C, with a standard deviation of 0.3 °C. At the top of the fuel plates (last acquisitions), the water temperature was equal to  $28.2 \pm 0.1$  °C which is near to the water-pool temperature (equal to 28.3 °C).

The water temperature measured by the second transducer shows some perturbations. These perturbations can be caused by overlap of echoes (specially the echo from which the transducer frequency is deduced) or electrical noise. Generally, temperature measurements were around  $27.8 \pm 0.1$  °C, with a standard deviation of 0.33 °C. Therefore, the average temperature gradient between the two transducers was about  $\pm 0.48$  °C.

### 3.2 Temperature measurements of the second water channel

During the second series of experiments, the water-pool temperature was equal to 27.8 °C which corresponds to  $95.95 \pm 0.01$  MHz and  $118.9 \pm 0.02$  MHz respectively measured by the first and second transducers. Measurements were performed in the second water channel.

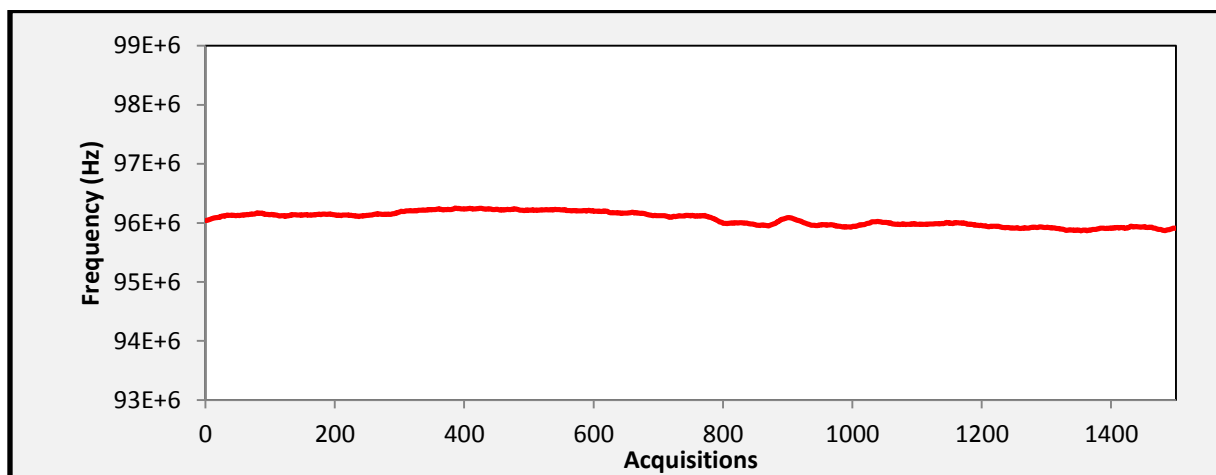


Figure 14: The first transducer frequency variation-values correspond to averages of 100 measured frequencies.

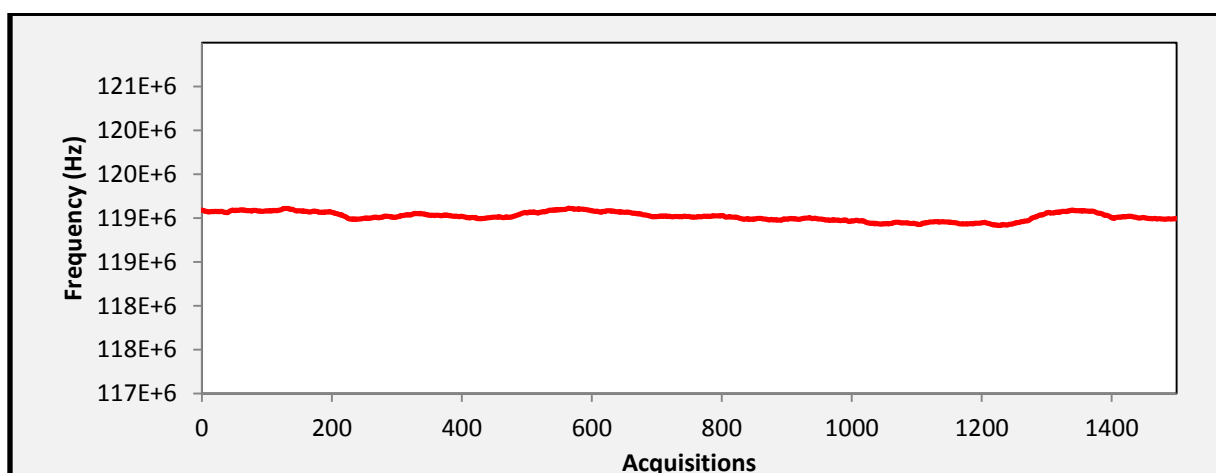


Figure 15: The second transducer frequency variation-values correspond to averages of 100 measured frequencies.

The Figures 14 and 15 present the transducers' frequency variations according to the number of measurements. The first acquisition represents the transducer frequency at a depth of 30 cm, while the last acquisition corresponds to the transducer frequency at the top of the

## Chapter IV: Experiments on the real RHF spent fuel element

plates. Several observations can be made from these figures. Indeed, for the first transducer, the frequency measurements were globally stable around a mean of  $96.1 \pm 0.1$  MHz, with a standard deviation of  $\sigma=0.26$  MHz. A slight frequency increase (about  $0.2 \pm 0.01$  MHz) was observed for the first 800<sup>th</sup> acquisitions and then a decrease of  $0.1 \pm 0.01$  MHz was observed beyond the 800<sup>th</sup> acquisitions.

The second transducer has a similar behavior than the first one. The frequency measurements were around  $119.01 \pm 0.01$  MHz with a standard deviation of  $\sigma=0.17$  MHz. A slight frequency increase (about  $0.2 \pm 0.01$  MHz) was observed between the 1300<sup>th</sup> and 1400<sup>th</sup> acquisitions.

From the frequency measurements (Figures 14 and 15), the water channel temperature was deduced (see Figure 16). The average temperature, measured by the first transducer, was equal to  $27.1 \pm 0.1$  °C with a standard deviation of 1.65 °C. At a depth of 30 cm the water channel temperature was around  $26.6 \pm 0.1$  °C and by ascending the blade, the temperature increased up to  $28 \pm 0.1$  °C.

For the second transducer, the temperature was  $27.08 \pm 0.01$  °C with a standard deviation of  $\sigma=1.06$  °C. At a depth of 30 cm the water channel temperature was around 26.6 °C and by ascending the blade, the temperature increased up to  $27.3 \pm 0.1$  °C. A sudden decrease (about 1 °C) was also observed between the 1300<sup>th</sup> and 1400<sup>th</sup> acquisitions. This variation can be related to the frequency measurement error or to the passage of a cold water flow.

The average temperature gradient between the two transducers was about  $0.02 \pm 0.01$  °C, while the difference between the water channel temperature and the water pool temperature was equal to  $0.2 \pm 0.01$  °C.

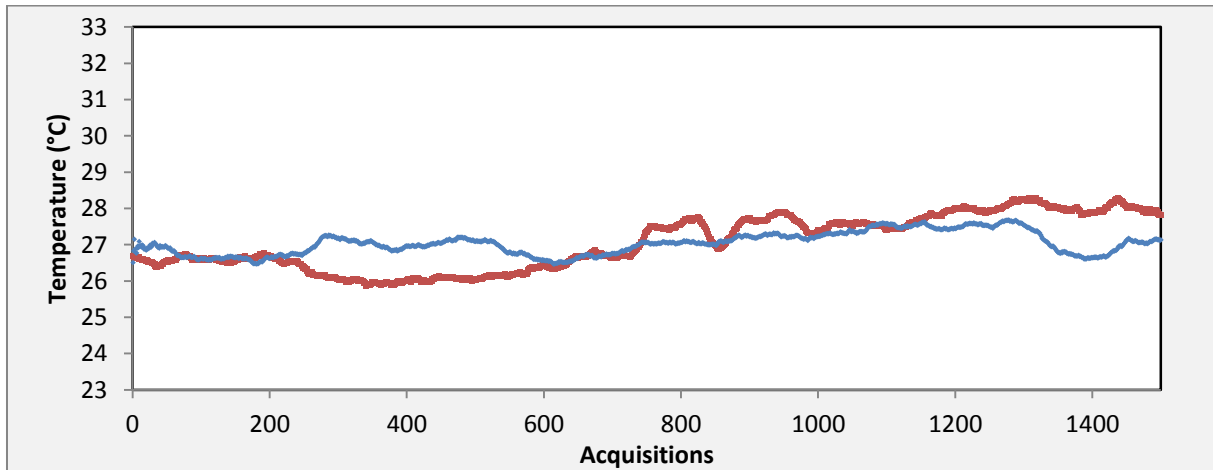


**Figure 16:** The first transducer temperature measurement –the red line corresponds to the water temperature measured by the first transducer and the blue line to the water temperature measured the second transducer – values correspond to averages of 100 acquisitions.

From the temperature measurements, it was possible to deduce the ultrasonic velocity variation along the 30 cm of the water channel (see Figures 17 and 18). For both transducers, the mean ultrasonic velocity was equal to  $1501.9 \pm 0.06$  m/s with a standard deviation of 4.1 m/s for the first transducer and 2.7 m/s for the second one.

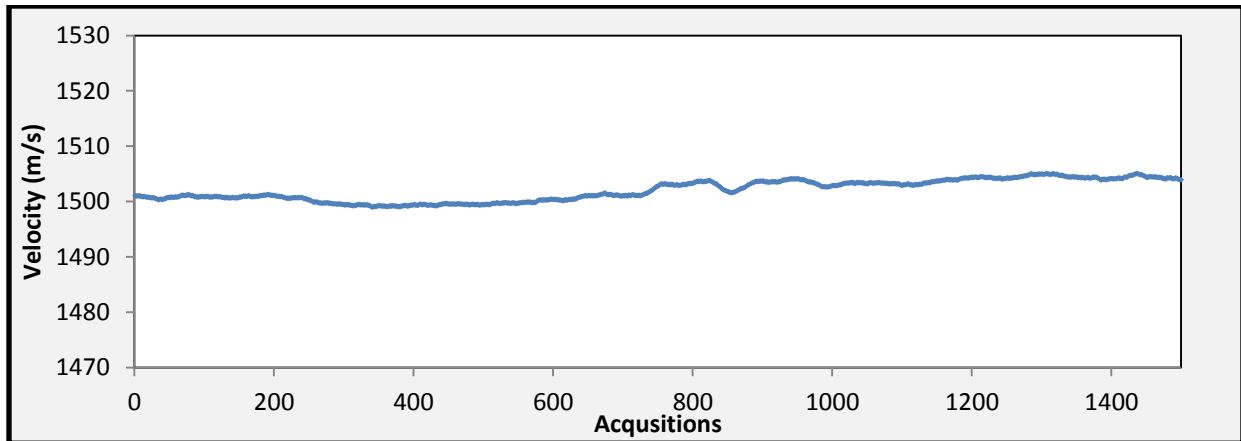


Figure 17: The ultrasonic velocity measured by the first transducer.

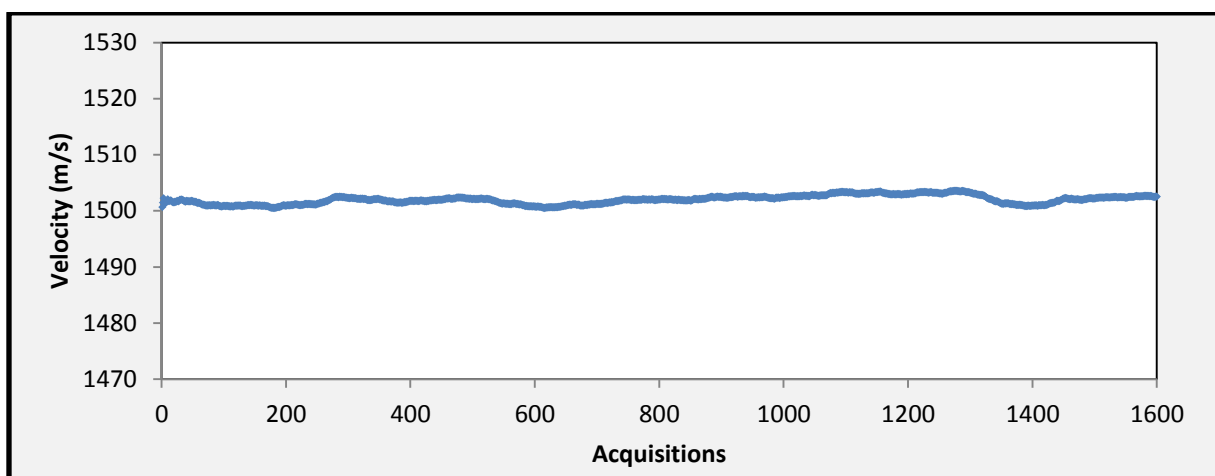


Figure 18: The ultrasonic velocity measured by the second transducer.

The difference between the measured velocity and the predefined one (1503 m/s measured at 27.8 °C in the water pool) was about  $\Delta v=1.1$  m/s. Therefore, velocity measurement error of 0.07% leads an error in the distance measurement of 0.11% (such as  $\Delta d = 2.03 \mu\text{m}$  and  $d$  (nominal) = 1,8mm).

#### 4. Distance measurements before irradiations

Before irradiation, the inter plates distance measurements were performed by CERCA (Compagnie pour l'Etude et la Réalisation de Combustibles Atomique) based on the eddy current (EC) principle. In this technique, presented in figure 19, the probes consist in a ferrite core with a surrounding electrical coil and a ceramic top pushed against the measured surface. The coil is fed by a high frequency current, producing a high frequency alternating magnetic field, inducing eddy currents in the fuel plate cladding. The magnitude of the induced eddy currents depends upon the distance between the ceramic probe tip and the electrically conductive cladding material [3].

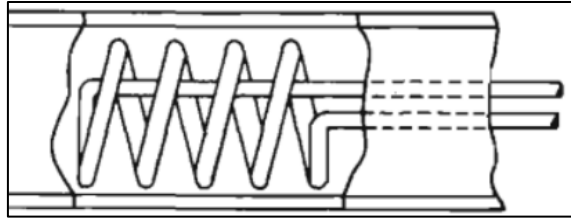


Figure 19: Internal coil [4].

An example of a thickness measurement is given in figure 20. Variations of the water channel thickness can be observed and will be measured in the following sections in-situ thanks to the ultrasonic device previously presented.

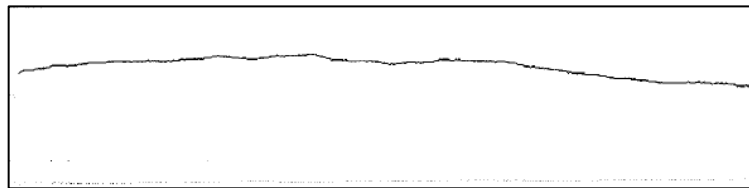


Figure 20: line scan of the water channel.

## 5. Water channel distance measurements post-irradiations

### 5.1 The first water channel thickness measurements post-irradiations

From the assessment of the ultrasonic wave time of flight and the speed of sound in water according to the temperature, the water channel thickness was deduced. Distance measurements were performed only when the blade was parallel to the fuel plates (maximum signal acquired by both transducers). Therefore, only the first 1150<sup>th</sup> temperature measurements were considered. The aberrant values due to the movements of the blade in the measurement area were removed from the results. These results are shown in Figure 23, such as each value is a mean of 5 measures.

During the first 1150 temperature measurements (see Figures 13), the water channel temperature showed a good stability. The average temperatures measured by the first and the second transducers were, respectively, equal to  $27.36 \pm 0.01$  °C and  $27.43 \pm 0.01$  °C. At these temperatures, the average ultrasonic velocity was equal to  $1502.2 \pm 0.02$  m/s in the propagation medium adjacent to the first transducer and  $1502.8 \pm 0.01$  m/s on the other side of the blade. Ultrasonic velocity measurement error of  $\Delta v = 0.6$  m/s (0.04 %) can lead to a relative error on distance measurement of 0.62%.

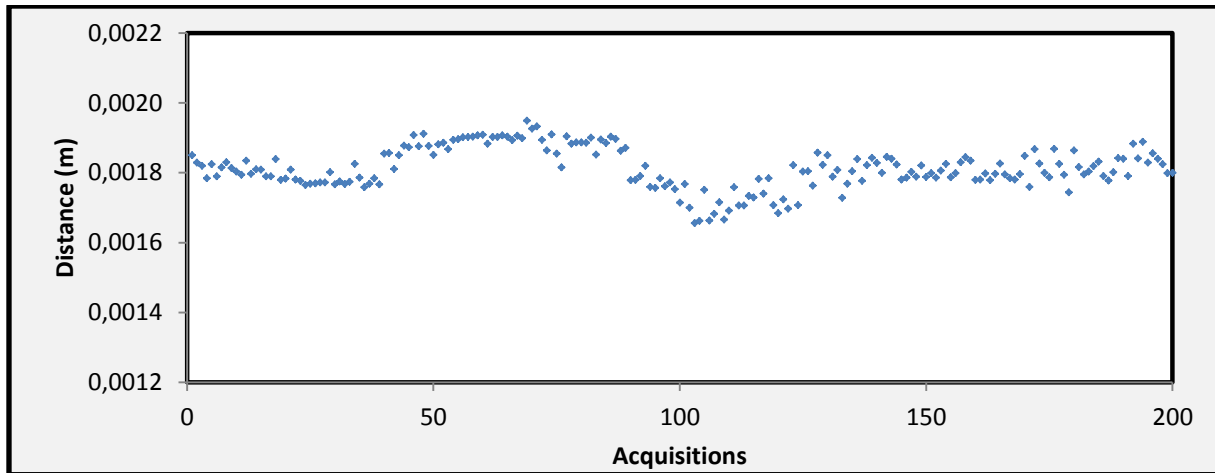


Figure 21: The first water channel thickness.

These results clearly show that in spite of the highly radioactive nature of the environment, the quality of the ultrasonic signals was sufficient to ensure a stable identification of the inter-plate distances.

Several observations can be made from Figure 21. Indeed by ascending the blade within the water channel, this later scans three different areas in the fuel plates. The first 40th values are acquired in the uranium zone of the plates. Here the average distance was equal to  $1.79 \pm 0.005$  mm with a standard deviation of  $2.4 \mu\text{m}$ . A slight increase of the distance up to  $1.89 \pm 0.001$  mm with a standard deviation of  $2.6 \mu\text{m}$  can be observed between acquisitions 44<sup>th</sup> and 87<sup>th</sup> indicating a change in the thickness of the water channel. Indeed, during these scans the blade was located outside the meat and the boron areas where no swelling is supposed to be happening. Finally, beyond the acquisition 100, corresponding to the boron zone of the plates, the water channel thickness was equal to  $1.79 \pm 0.005$  mm with a standard deviation of  $2.4 \mu\text{m}$ . This is slightly less than the average channel thickness specified by the fuel plate manufacturer (CERCA), which can probably indicate a plate swelling of  $0.1 \pm 0.004$  mm (in particular, in the uranium and boron zone).

The large variations at the 100<sup>th</sup> acquisition correspond to a slight vibration of the blade in the measurement areas and should not be considered as relevant.

### 5.2 The second water channel thickness measurements post-irradiations

As mentioned above distance measurement were also performed in a second water channel (N° 2) at two stages. At the first stage, the blade was introduced at a depth of 30 cm and then it was brought out by steps to a depth of 17 cm in the water channel. Then, the blade was brought out continuously. As mentioned above, the blade was handled manually by an operator from a distance of 5 m. Therefore, the speed of the blade ascent was not controlled. This parameter will be taken into account in the future works by developing a guiding system that allows the correlation of the measurements with the sensor position. Moreover, with this system the speed of the blade ascent/descent will be controlled.

- **Distance measurements by steps :**

The results of the first stage of distance measurement are shown in Figure 22.

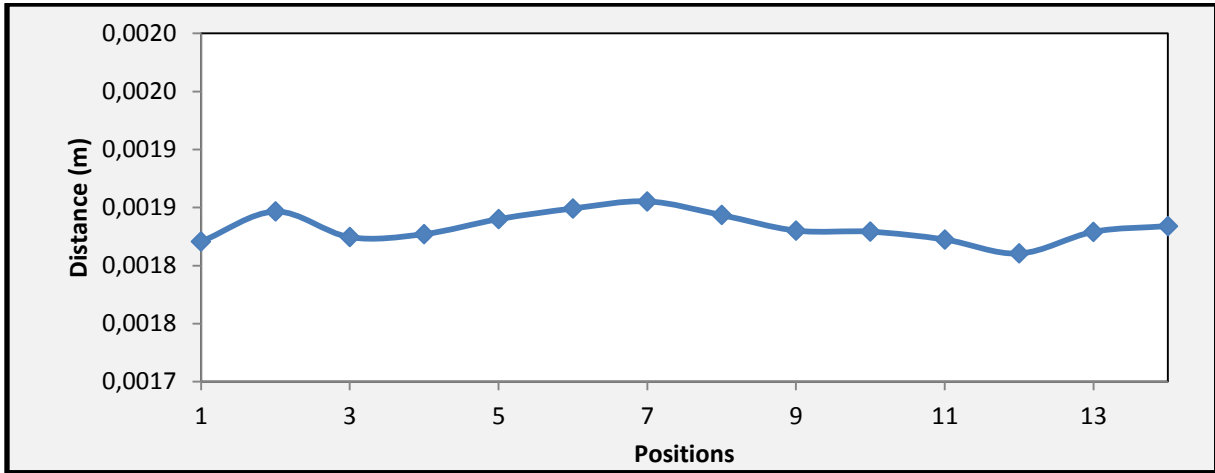


**Figure 22: Inter-plates distance measurement (from 30 cm to 17 cm depth).**

In Figure 22, the first value corresponds to the water channel thickness at 30 cm depth. Measurements were then recorded by ascending the blade by steps of 1 cm. For each position, the blade was placed perfectly parallel to the plates and hundred acquisitions were performed. For example, from the 9<sup>th</sup> to the 10<sup>th</sup> position the corresponding measurements are shown in Figure 23. This Figure clearly shows that in spite of the highly radioactive nature of the environment, the quality of the ultrasonic signals was sufficient to ensure a stable identification of the inter-plate distances. The observed disturbances are mainly due to electrical noise overlapping with the acoustic signal. Here, the average distance was about  $1.83 \pm 0.01$  mm, with a standard deviation of  $1.62 \mu\text{m}$ .

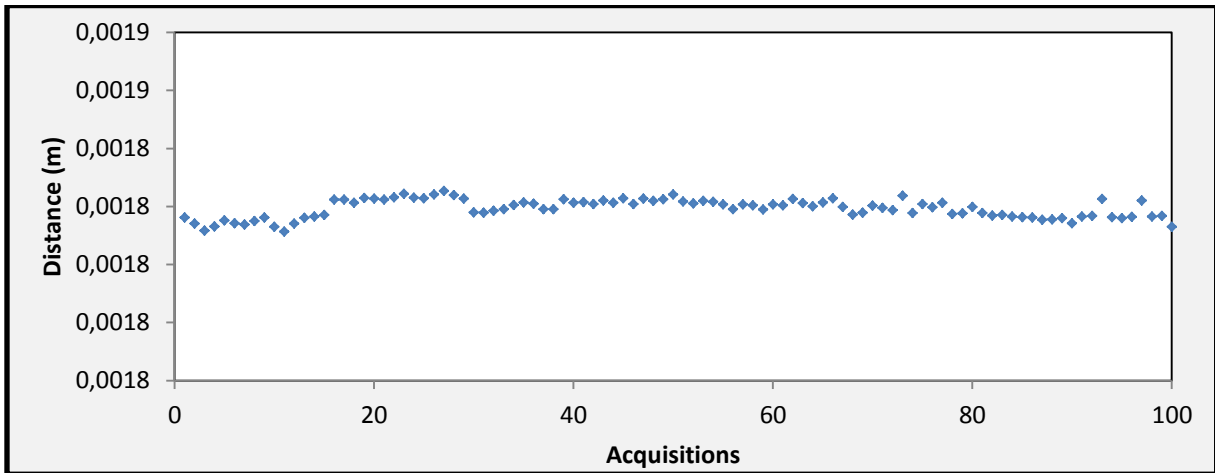


**Figure 23: Distance measurement while ascending the blade from the position 9 to 10.**

Several observations can be made from Figure 22. Indeed, along 14 cm of the water channel, the average distance was equal to  $1.83 \pm 0.003$  mm. The line scan clearly shows a deformed area with a maximum around 24 cm from the top of the plate. Locally, a thickness up to  $1.85 \pm 0.005$  mm was measured which is a decrease of  $250 \mu\text{m}$  compared to the nominal water channel thickness of 2.1 mm. A Slight decrease of the water channel thickness down  $1.81 \pm 0.001$  mm was also observed around 19 cm from the top of the plate. This thickness variation probably indicates a change of the inter-plate distance due to the plates swelling in the meat area.

## Chapter IV: Experiments on the real RHF spent fuel element

By measuring distance step by step, stable measurements at specific positions (separated of 1 cm) were performed. However, measurement points were insufficient.

- **The continuous distance measurement :**

The results of the second stage of distance measurement are shown in Figure 24. Blue points represent the raw data and the red line corresponds to an average value measured every 10 acquisitions.

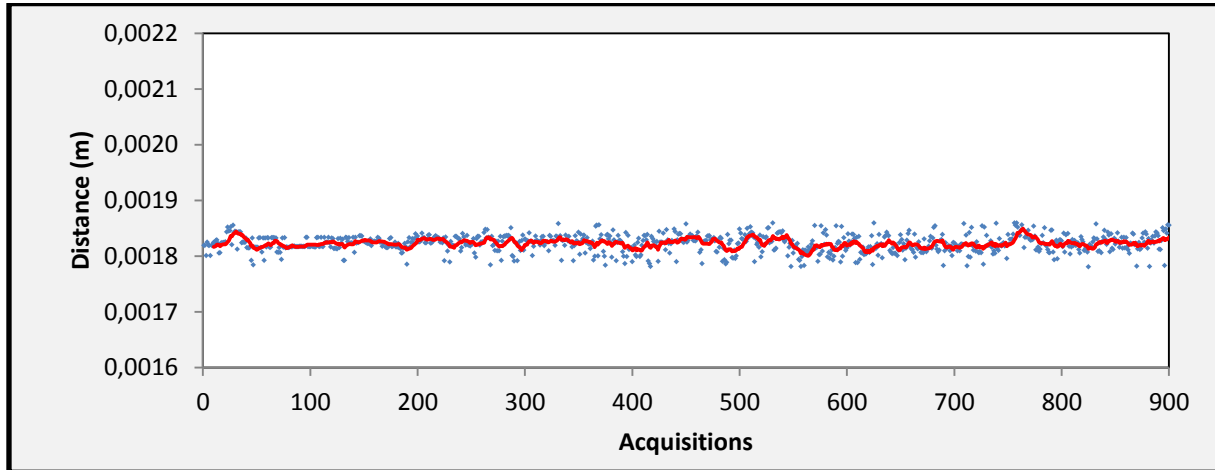


Figure 24: Distance measurements by ascending the blade continuously.

These results are a continuation of measurements presented in the previous section (Figure 22). Here, the blade was continuously displaced along the water channel (the speed of the blade ascent was not controlled).

On average the water channel thickness varies from  $1.81 \pm 0.01$  mm to  $1.84 \pm 0.01$  mm with a standard deviation of  $15 \mu\text{m}$  while ascending the blade from a depth of 17 cm to the top of fuel plates. To conclude, in this second stage, several measurements at different positions were performed continuously.

Despite the difficult conditions of the experiment and the high radioactive environment, stable and appropriate measurements to the predefined ones (by the fuel plate manufacturer) were obtained.

### 6. Experimental feedbacks

First, the feasibility of temperature measurement has already been proved with success on a full size irradiated fuel element of the RHF reactor. The advantage of this measurement technique can be summarized in the following points:

- Radiation resistance,
- Precisely accurate. Indeed, small temperature variations (about 1/10) were detected allowing, thus, accurate distance measurements of  $20 \mu\text{m}$ .
- Instantaneous response (less than one second). Indeed as well known, the smaller the sensor, the faster the response in time.

However, some flaws may still have to be corrected to perform absolute measurements. Indeed, it was observed that the temperature measurement technique was influenced by the electrical reflections in the cables of 15 m length. This adds low frequencies in the frequency

## Chapter IV: Experiments on the real RHF spent fuel element

---

spectrum of the transducers and noised echoes in the temporal signal. Therefore, the selection of echo, from which the transducer resonance frequency is deduced, becomes difficult.

On the other hand, the feasibility of distance measurements between high irradiated fuel plates was validated through the first experiment. This experiment has also proved that the different components of the ultrasonic transducers showed good resistance to radiations. Moreover, the quality of the acoustic signal was sufficient to get a very stable assessment of the inter-plate distance. Experimental constraints were identified, and then considered to improve the measurement accuracy during the second experiment. By using an updating ultrasonic device operating at frequencies up to 120 MHz, series of distance measurements were performed in different water channels. Therefore, the repeatability and the accuracy of the measurement system were proved, and quantitative measurements were obtained. Moreover, appropriate distance measurement results, compared to the values specified by the fuel plate manufacturer (CERCA), have been found with a slight difference probably indicating a water channel thickness variation. Thanks to the high frequency acquisition instruments and the ultrasonic device, distance measurements were performed with a precision of 20  $\mu\text{m}$ .

However, the accuracy of distance measurements is related to the blade tolerance. Indeed, distance between fuel plates corresponds to distance measured by each transducer plus the blade thickness. Therefore, an error on the blade thickness measurement may cause an error on the inter-plate distance measurements. In future works, the blade thickness and transducers planarity will be controlled by high frequency acoustic microscopy.

Moreover, during measurements, the blade/pole system was handled by hand thanks to an operator held in a cradle. Neither the parallelism of the blade relative to the plates nor the vertical position are respected in such a configuration. This is the reason why a new support system is being designed. The most recent drawings are presented below. Thanks to this new system, it will be possible to carry out accurate and quantitative measurements. The blade will be guided to be positioned in a water channel and then slid along the water channel to perform continuous measurements. The vertical position of the blade will be measured on line in order to correlate measurements with the sensor position. The blade can also be positioned at three different radii (inner ring side, outer ring and the middle) and in the 280 channels. The total height of the pole is around 5 m and it will be controlled from a platform located above water.

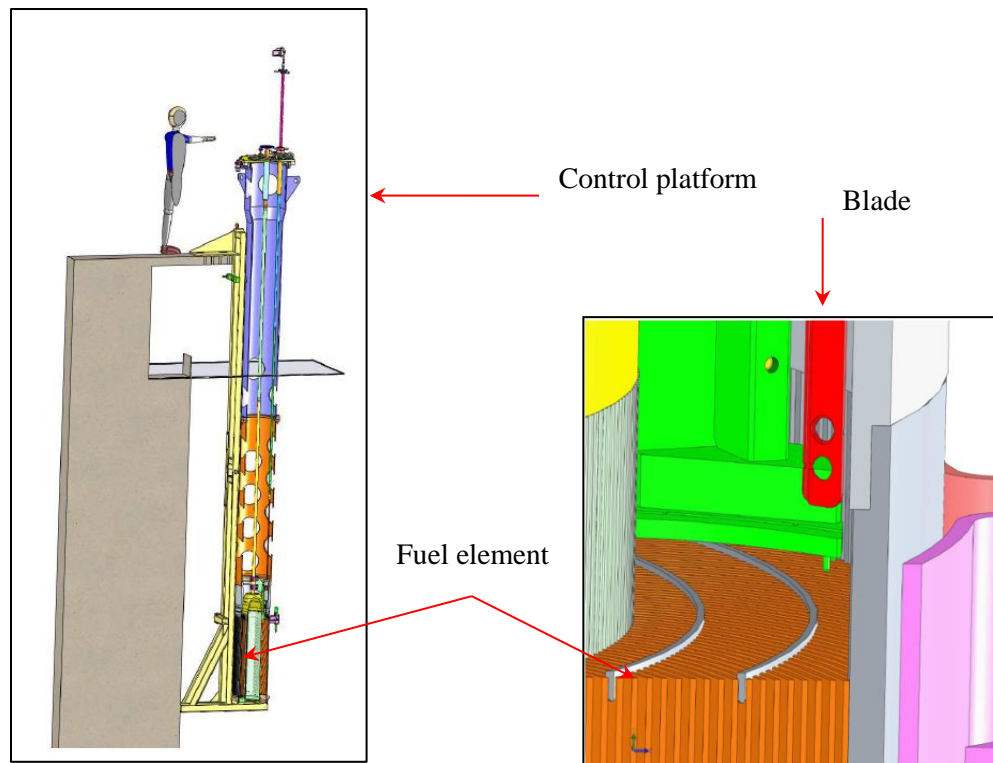


**Figure 25: The designed guiding system.**

Experiments gave us also some feedback for optimizing the transducers. One of the major options that will be tested in the next experiments is the modification of the silica glass. A small hole will be drilled in order to create an acoustic lens (see Figure 26). The aim is to focus the acoustic waves in order to compensate the possible angular discrepancy between the silica glass surface and the fuel plates. Such a discrepancy may be due to the gluing of the silica glass, which is a real challenging process.



**Figure 26: Silica glass of the transducers with and without the lens**

Moreover, future developments of the ultrasonic device are envisaged, like getting qualitative information about thermal conductivity or setting-up of a gamma sensor.

Finally, series of measurements will be carried out with the updated system on ILL spent fuel elements for both getting quantitative temperature measurements and performing absolute distance measurements.

### IV. Conclusion

This chapter presents the experimental results of the ultrasonic device using two high frequency ultrasonic transducers, radiation resistant, developed to measure fuel plates' swelling inducing water channel thickness variations inside a High Flux Reactor. The device was further attached to a cylindrical holder to be manipulated from a distance of 4 meters below the water surface. To allow a precise monitoring of the fuel element evolution, measurements were performed with a resolution up to 10  $\mu\text{m}$ . To achieve this resolution, the system was excited with frequencies up to 120 MHz and integrated into a set of high frequency acquisition instruments. Knowing the speed of sound in water, the device allows the distance measurement through the evaluation of the ultrasonic wave's time of flight. The feasibility of such a challenging measurement in a highly radioactive environment has been proved during the first series of measurements and the experimental constraints have been identified. These constraints have been considered in the second experiment, performed in a full size irradiated fuel element, to improve the measurement reliability, in particular, the temperature dependence of the distance measurement and to get accurate and quantitative measurements. During this experiment, transducers have resisted to radiation for a long time (about 6 hours).

The evaluation of the local water temperature inside the water channels was performed using the ultrasonic device as a thermometer thanks to the analysis of the spectral components of the acoustic signal propagating inside the sensor multilayered structure. The feasibility of temperature measurement was proved during the second experiment in the RHF fuel element. Some of the results have been presented which clearly show that in spite of the highly radioactive nature of the environment, the quality of the measurements was sufficient to ensure a stable identification of the water channel temperature. Some experimental constraints were also identified to improve the accuracy of the measurement in future works.

Moreover, future developments of measurement system are envisaged, like using a guiding system to ease the insertion of the blade and to stabilize its position between the fuel plates. Furthermore, to reduce the potential impact of the non-parallelism of transducers relative to the plates on the acoustic signal, a new transducer with an acoustical lens will be tested.

### List of Figures

Figure 1: Positioning of the blade between two fuel plates. ....	99
Figure 2: Positioning of the blade in the fuel element. ....	99
Figure 3: The first series of echoes of the acquired acoustic signal. ....	99
Figure 4: Experimental results of the first experiment in the RHF fuel element. ....	100
Figure 5: The updated drawing of the blade. ....	101
Figure 6: Left the blade positions within the first water channel and right the blade positions within the second water channel. ....	102
Figure 7: Transducer 2 temporal signal in the water pool of the reactor. ....	102
Figure 8: Transducer 1 frequency in the water pool of the reactor. ....	102
Figure 9: Transducer 2 frequency in the water pool of the reactor. ....	103
Figure 10: Transducer 2 temporal signal in the water pool of the reactor. ....	103
Figure 11: The first transducer frequency variation-values correspond to averages of 100 measured frequencies. ....	103
Figure 12: The second transducer frequency variation-values correspond to averages of 100 measured frequencies. ....	104
Figure 13: Transducers temperature measurement –the red line corresponds to the first transducer resonance frequency and the blue line to the second transducer resonance frequency – values correspond to averages of 100 acquisitions. ....	104
Figure 14: The first transducer frequency variation-values correspond to averages of 100 measured frequencies. ....	105
Figure 15: The second transducer frequency variation-values correspond to averages of 100 measured frequencies. ....	105
Figure 16: The first transducer temperature measurement –the red line corresponds to the water temperature measured by the first transducer and the blue line to the water temperature measured the second transducer – values correspond to averages of 100 acquisitions. ....	106
Figure 17: The ultrasonic velocity measured by the first transducer. ....	107
Figure 18: The ultrasonic velocity measured by the second transducer. ....	107
Figure 19: Internal coil. ....	108
Figure 20: line scan of the a water channel. ....	108
Figure 21: The first water channel thickness. ....	109
Figure 22: Inter-plates distance measurement (from 30 cm to 17 cm depth). ....	110
Figure 23: Distance measurement while ascending the blade from the position 9 to 10. ....	110
Figure 24: Distance measurements by ascending the blade continuously. ....	111
Figure 25: The designed guiding system. ....	113
Figure 26: Silica glass of the transducers with and without the lens ....	113

### Reference

- [1] Y. Calzavara, F. Frery, F. Thomas, H. Guyon, A. Bergeron, A. Tentner, J. Stevens, et W. Haeck, « TOUTATIS: ILL CONVERSION FEASIBILITY STUDY », RERTR 2010, Lisbon, Portugal.
- [2] K. H. Zografski, « Research Reactor Fuel Management », 10<sup>th</sup> International Topical Meeting on Research Reactor Fuel Management, 2006, Bulgaria.
- [3] W. H. Cubberly, *Tool and Manufacturing Engineers Handbook Desk Edition*. Society of Manufacturing Engineers, 1989.

---

Conclusion & Prospects

---

### Conclusion and Prospects

Examination of irradiated fuel elements is crucial for assessing the LEU fuel plate's behavior. A device using two ultrasound transducers, radiation resistant, was developed for such applications. The advantages of this device are obvious: increasing the feedback on irradiated fuel plates, shortening the cooling time needed before usual Non-Destructive Post Irradiation Examination (ND PIE) and replacing the usual ND PIE. Indeed, thanks to its small size (1 mm thickness), the device can easily be inserted within the water channel (1.8 mm nominal thickness) and thus provides measurements of one of the most feared behavior of fuel plates which is the plates swelling; i.e. the water channel variation. The operating principle is based on the measurement of the time of flight (T.o.F.), which is, the time needed for an ultrasonic wave to travel from the transmitter to the receiver after being reflected by the plate surface. Based on the pulse-echo method, the same transducer is used both as a transmitter and as a receiver. Distance measurements with a microscopic resolution are expected. Therefore, the transducers have been excited with frequencies up to 120 MHz, and integrated into a set of high frequency electronic instruments.

At high frequencies, the multilayer structure of the transducers plays a central role in the waveform of transmitted and received signals, hence the need to simulate the wave propagation inside these structures. The simulation results were then presented and compared to the experimental acoustic signal. A slight difference was observed which is being studied. To match experimental constraints, the model also includes a non-parallelism of the transducers relative to the plate surface, to estimate the error rate caused by this phenomenon.

After the manufacturing process, the structure of the transducers has been controlled by acoustic microscopy to make images of their internal features, including the fatness of layers and defects such as cracks, delamination and voids.

The high frequency ultrasonic device was then tested in a full size irradiated fuel element of the RHF reactor, proving thus the feasibility of distance measurements in a high irradiated environment. The validity of the absolute values was not confirmed, however, the excellent relative resolution, about few microns, makes possible the identification of areas of the inter-plate space contraction. The experimental constraints attached to measurement procedure were then identified. In particular, temperature measurement of the water channel was among these constraints. Indeed, the distance measurement accuracy depends on the ultrasonic wave ToF estimation and on the sound speed in water which is temperature dependent.

To address this issue, the high frequency ultrasonic device was used to perform temperature measurement along the water channel. It makes possible measurements from the study of the spectral component of the ultrasonic wave. Indeed, the thermal expansion of the piezoelectric element (which induces thickness variations) leads to a resonance frequency variation of the transducer. Therefore, the resonance frequency variation law of the transducer according to the temperature was defined, from which the water channel temperature was deduced.

The next step was to evaluate the ultrasonic device performances, in laboratory condition, by measuring the ultrasonic velocity in water contained in a tank with a known thickness. The results of this system were close to those previously proposed in the literature with less than 2% error, proving thus the reliability and the accuracy of the developed ultrasonic device.

## Conclusion & Prospects

---

A second series of measurements were then carried out in a full size irradiated fuel element. Measurements were performed by an optimized device, operating at frequencies up to 120 MHz, with the following dimensions: a thickness of 1 mm, a width of 10 mm and a length of about 1500 mm. These dimensions allowed the device to be easily inserted between fuel plates and to slide along the water channel. Through this experiment the first series of quantitative distance measurements were obtained. Measurements were performed in different water channels and appropriate results, compared to the values specified by the fuel plate manufacturer, were found with a slight difference indicating a water channel thickness variation. The feasibility of the water channel temperature measurement was also proved. The results clearly show that in spite of the highly irradiative nature of the environment, the quality of the measurements was sufficient to ensure a stable identification of the water channel temperature. Some experimental constraints were also identified to improve the accuracy of the measurement in future works.

There are many prospects for this thesis. To improve temperature measurements, it is necessary to search and eliminate all disturbance sources which can be due to an electric noise, the signal overlap, and so on.

On the other hand, a supporting device, a guiding system, is designed to ease the insertion of the sensor into the fuel element and to stabilize its position between the fuel plates. Then, in order to improve the measurement accuracy and in order to increase the amount of information recorded during the measurements, a new device having two focused transducers will be designed and studied. This step requires the development of complex models to understand the wave propagation in non-plane structures. Furthermore, experiments will be performed into highly radioactive conditions in order to improve the knowledge on the sensor behavior under high radiations.

In future works, the ultrasonic device will also make possible the measurement of irradiated fuel elements parameters of crucial importance. The first of them will be the aluminum oxide layer growth on all the fuel plates. This layer has a tremendous impact on the thermal-hydraulic margins. It must thus be characterized with the highest available accuracy. Eventually, the ILL aims also to probe the interface between the cladding and the meat, where fission gas bubbles may grow and lead to pillowing effects for example.

In long-term, the ILL is planning to use the high frequency ultrasonic sensor as a generic demonstrator designed to probe every fuel plate element.

## Conclusion & Prospects

---



# Glossary



# Glossary

---

## Glossary

<b>ANL</b>	Argonne National Laboratory
<b>CERCA</b>	Compagnie pour l'Etude et la Réalisation de Combustibles Atomique
<b>DT</b>	Destructive Testing
<b>DHI</b>	Double-Heterodyne Interferometry
<b>EC</b>	Eddy Current
<b>EPMA</b>	Electron-Probe Microanalysis
<b>FMCW</b>	Frequency-Modulated continuous wave interferometry
<b>FE</b>	Fuel Element
<b>HERACLES</b>	Highly enriched European Reactor Action for their Conversion into Lower Enriched Solution
<b>LEU</b>	High Enriched Uranium
<b>HFIR</b>	High Flux Isotope Reactor
<b>ILL</b>	Institute Laue-Langevin
<b>IES</b>	Institute of Electronics and Systems
<b>IL</b>	Interaction Layer
<b>IRPhEP</b>	International Handbook of Evaluated Reactor Physics Benchmark Experiments
<b>LED</b>	Light-Emitting Diode
<b>LEU</b>	Low Enriched Uranium
<b>MoU</b>	Memorandum of Understanding
<b>NI</b>	National Instrument
<b>NDT</b>	Nondestructive Testing
<b>NEA</b>	Nuclear Energy Agency
<b>OM</b>	Optical Microscopy
<b>PSM</b>	Phase Shift Method
<b>PIE</b>	Post Irradiation Examinations
<b>PXI</b>	PCI extension for Instrumentation
<b>PXIe</b>	PCI extension for Instrumentation express
<b>RERTR</b>	Reduced Enrichment for Research and Test Reactors
<b>RTD</b>	Resistance Temperature Detector
<b>RHF</b>	Réacteur à Haut Flux
<b>SEM</b>	Scanning electron microscopy
<b>SNR</b>	Signal-to-Noise Ratio
<b>SLD</b>	Super-Luminescent Diodes
<b>ToF</b>	Time of Flight
<b>TOUTATIS</b>	Traitement Optimisé de l'Uranium et Thermique Améliorée pour une Technologie Intégrant la Sûreté
<b>TMM</b>	Transfer Matrix Method
<b>UMo</b>	Uranium – Molybdenum
<b>UAl<sub>x</sub>/Al</b>	Uranium Aluminide-Aluminum
<b>WLI</b>	White Light Interferometry
<b>XRD</b>	X-ray diffraction

---

---

# Appendix

---

### Appendix 1: Parameters of the Transfer Matrix Method

The longitudinal and transverse velocities, the volume density and the thickness of the transducer layers are expressed in the following table:

layers	Thickness (μm)	V <sub>L</sub> (m/s)	V <sub>t</sub> (m/s)	Density
LiNbO3	25	7331	4300	4700
Chrome	≈5	6608	4005	7194
Or	≈5	3240	1200	19300
Cyanolit	≈0.01	2400	0.001	1050
SinO2	480e-6	5968	3764	2150

Table 3: Parameters of the transducers layers.

The coefficients  $a_{ij}^{(n)}$  of equation (11) can be expressed in terms of the following parameters:

$$E_n = \alpha_n / \sigma \quad F_n = \beta_n / \sigma \quad G_n = 2\sigma^2 / K_n^2 \quad H_n = \rho_n \omega / \sigma$$

The quantity  $\rho_n$  is the density of the material of the layer  $n$ ,  $\omega$  is the signal frequency, and  $\sigma$  is the component of the wave vector, such as:

$$\sigma = k_1 \sin \theta_1 = k_2 \sin \theta_2 = \dots = k_{n+1} \sin \theta_{n+1}$$

where  $\theta_i$  are the incidence angles. The quantities  $k$  and  $K$  are given by:

$$K_n = \omega / b_n \quad \text{and} \quad k_n = \omega / c_n$$

where  $b_n$  is the complex (to include attenuation) transverse velocity and  $c_n$  is the complex longitudinal velocity. The quantities  $\alpha_n$  and  $\beta_n$  are given by:

$$\alpha_n = (k_n^2 - \sigma^2)^{1/2}$$

$$\beta_n = (K_n^2 - \sigma^2)^{1/2}$$

Therefore, the coefficients  $a_{ij}^{(n)}$  for visco-elastic layer  $n$  are expressed as follow:

$$\begin{aligned} a_{11}^{(n)} &= G_n \cos P_n + (1 - G_n) \cos Q_n & a_{32}^{(n)} &= -i H_n \{ [(1 - G_n)^2 \sin P_n] / E_n + F_n G_n^2 \sin Q_n \} \\ a_{12}^{(n)} &= i [(1 - G_n) \sin P_n / E_n] - i F_n G_n \sin Q_n & a_{33}^{(n)} &= a_{22}^{(n)} \\ a_{13}^{(n)} &= - (1 / H_n) (\cos P_n - \cos Q_n) & a_{34}^{(n)} &= a_{12}^{(n)} \\ a_{14}^{(n)} &= - (i / H_n) [(\sin P_n / E_n) + F_n \sin Q_n] & a_{41}^{(n)} &= -i H_n \{ E_n G_n^2 \sin P_n + [(1 - G_n)^2 \sin Q_n] / F_n \} \\ a_{21}^{(n)} &= i E_n G_n \sin P_n - i [(1 - G_n) \sin Q_n] / F_n & a_{42}^{(n)} &= a_{31}^{(n)} \\ a_{22}^{(n)} &= (1 - G_n) \cos P_n + G_n \cos Q_n & a_{43}^{(n)} &= a_{21}^{(n)} \\ a_{23}^{(n)} &= - (i / H_n) (E_n \sin P_n + \sin Q_n / F_n) & a_{44}^{(n)} &= a_{11}^{(n)} \\ a_{24}^{(n)} &= a_{13}^{(n)} \\ a_{31}^{(n)} &= - H_n G_n (1 - G_n) (\cos P_n - \cos Q_n) \end{aligned}$$

## Appendix 2: Acquisition software

The acquisition software operates as follows way:

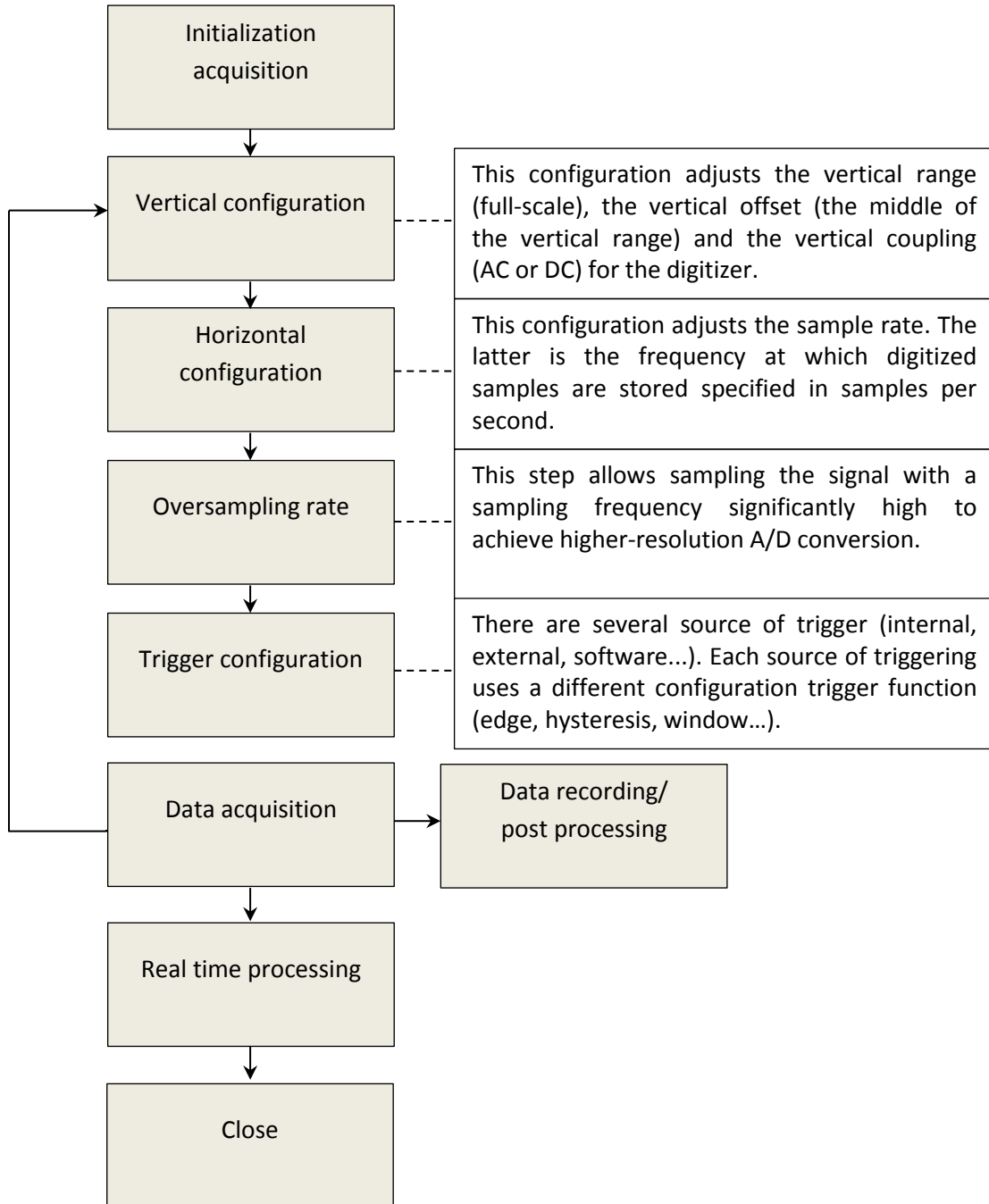


Figure 1: Block diagram of the acquisition software.

# Appendix

The signal acquisition program is divided into two parts:

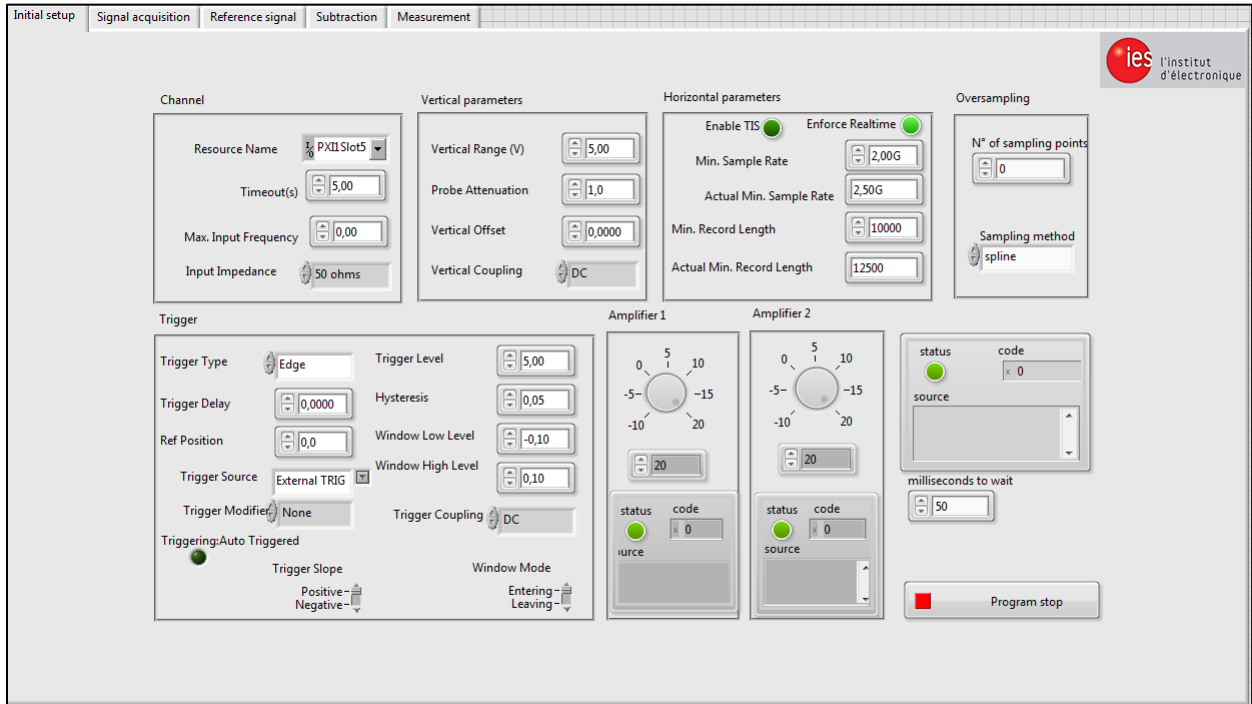


Figure 2: Acquisition system software – Initial set-up

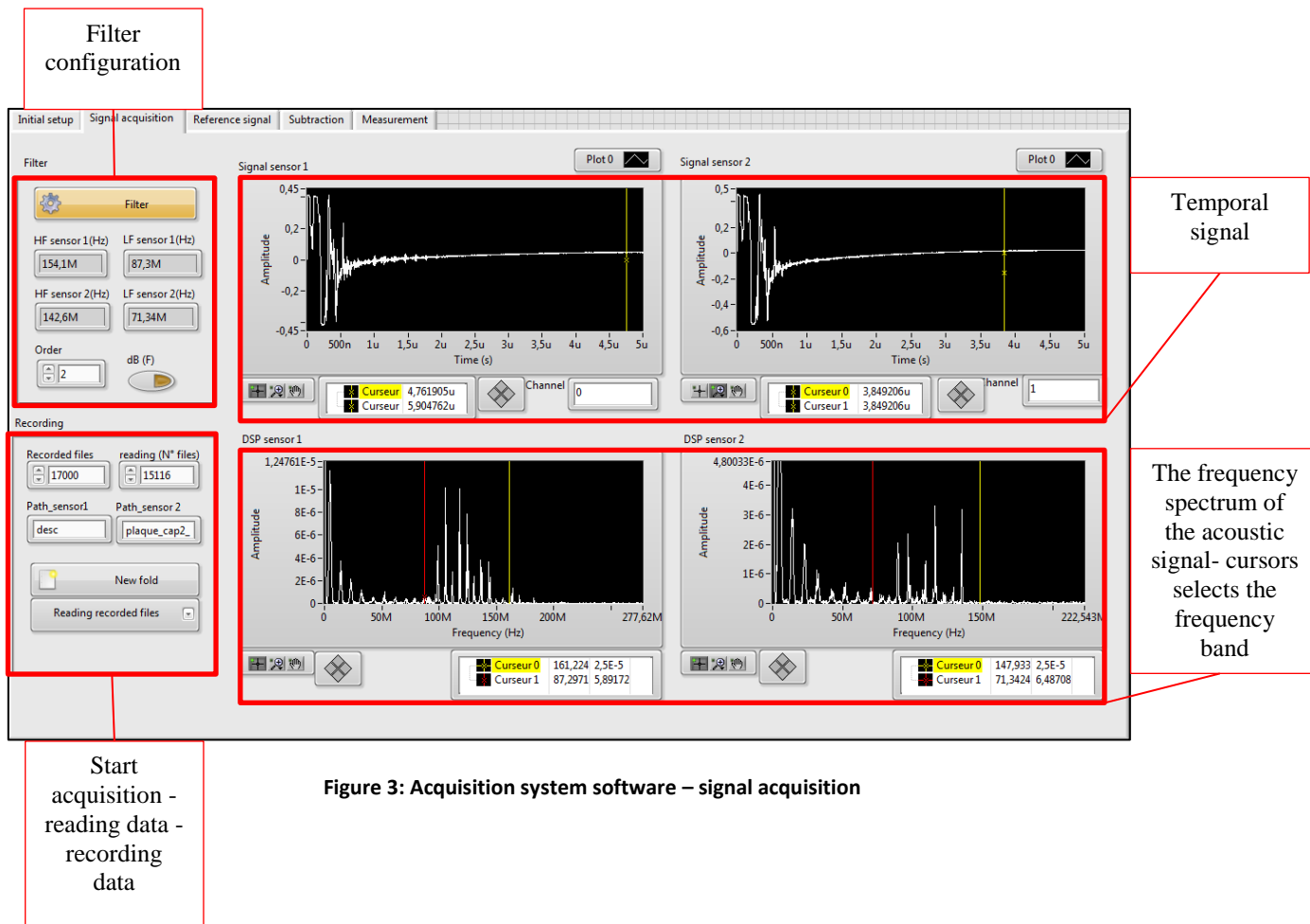


Figure 3: Acquisition system software – signal acquisition

## Appendix 3: Signal processing

The block diagram of the processing signal is shown below:

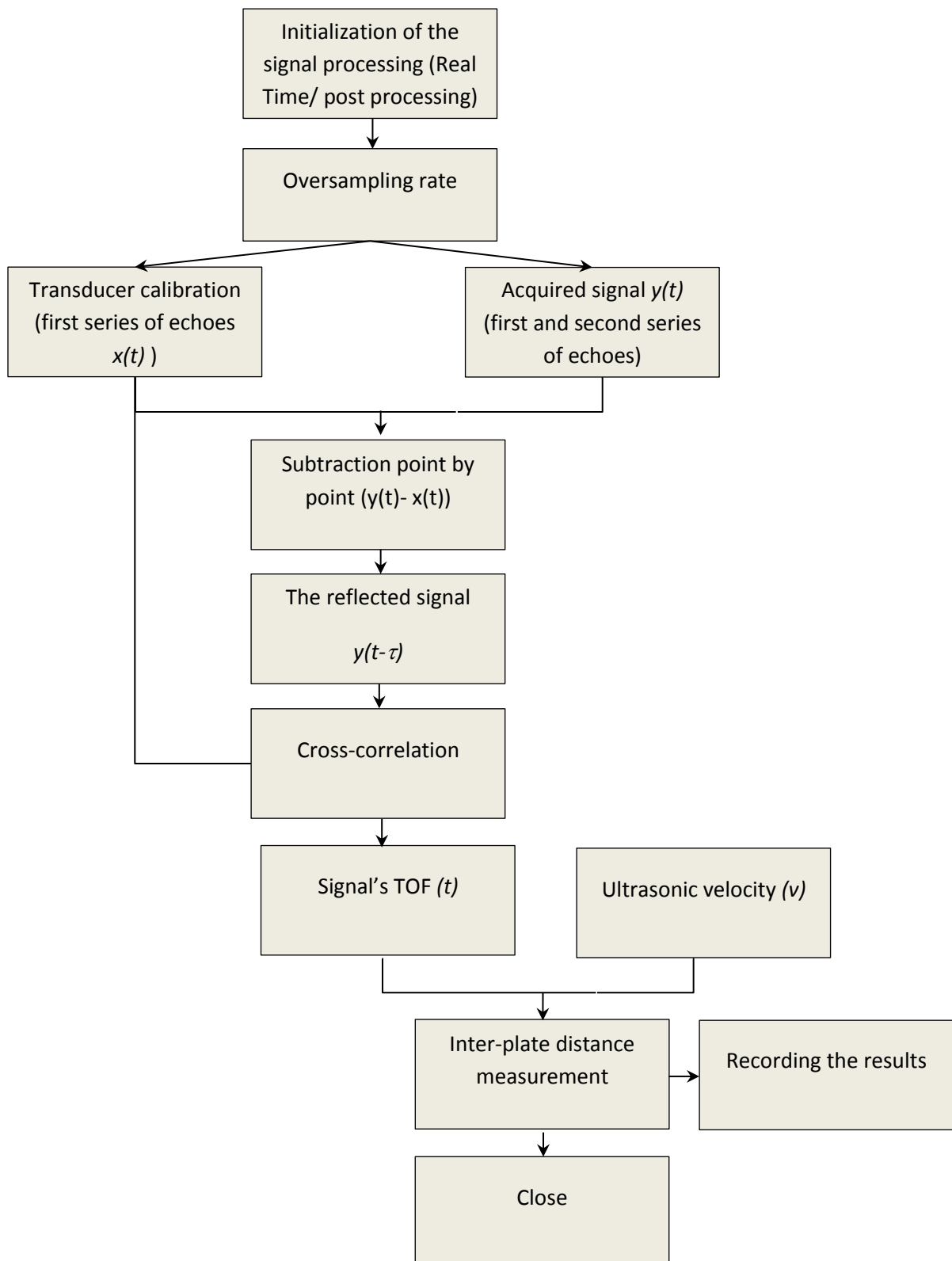
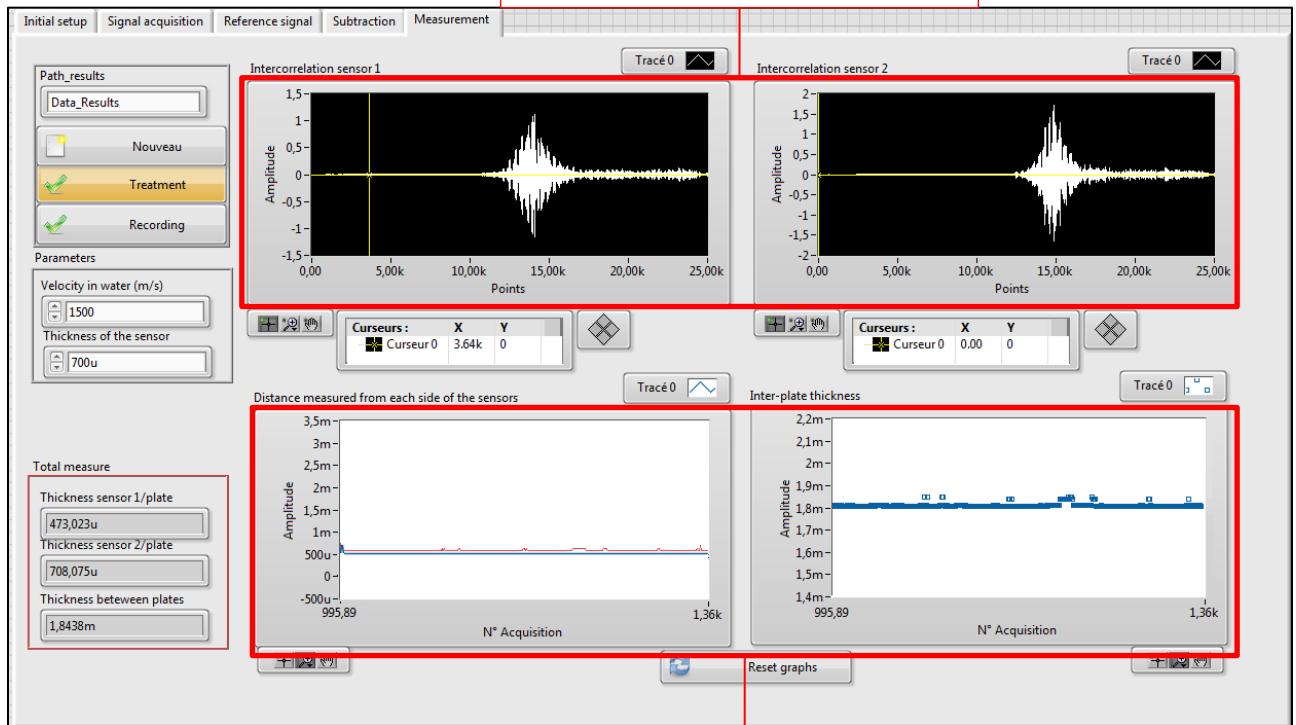


Figure 1: Block diagram of the signal processing.

# Appendix

The inter-correlation results for both transducers



The inter-plate distance measurement: the figure on the left represents the distance measured by each transducer; the figure on the right corresponds to the total distance (distances measured by each transducer + the blade thickness)

Figure 2: The signal processing software

## Appendix 4: Temperature measurement

The control software of the temperature acquisition is shown below:

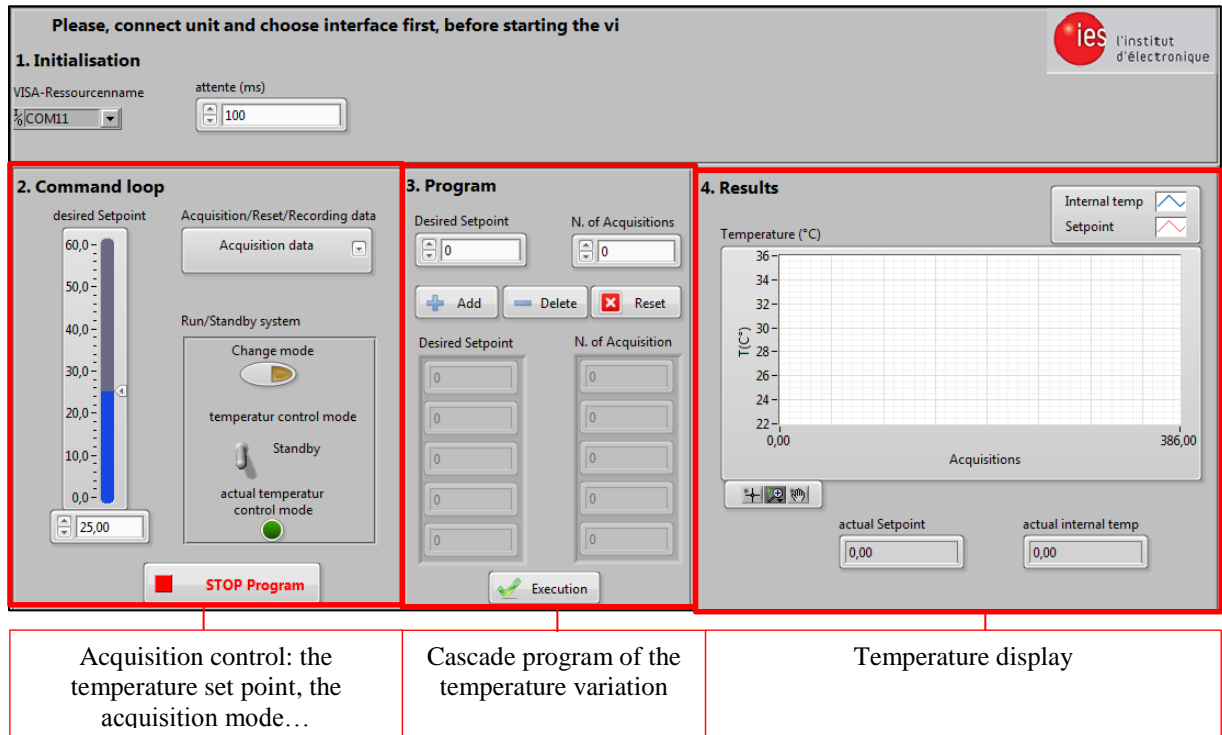


Figure 1: The control software of the temperature acquisition

# Appendix

---



# Communications



## Communications

### National and International articles

- **Two papers will be submitted during 2015/2016**
- G. Zaz, Y. Calzavara, E. Le Clézio, et G. Despaux, « Adaptation of a High Frequency Ultrasonic Transducer to the Measurement of Water Temperature in a Nuclear Reactor », *Phys. Procedia*, vol. 70, p. 195-198, 2015.
- G. Zaz, A. Dekkious, P. A. Meignen, Y. Calzavara, E. Le Clézio, et G. Despaux, « High Frequency Transducer Dedicated to the High-resolution in Situ Measurement of the Distance between Two Nuclear Fuel Plates », *Phys. Procedia*, vol. 70, p. 191-194, 2015.

### Invited lectures in an international congress

- G.ZAZ, Y. CALZAVARA, E. LE CLEZIO, G. DESPAUX: « **Post Examination of the Reactor high flux Single Element with Ultra-Sounds**», *Argonne National Laboratory Nuclear Engineering Division Argonne, Illinois* on October 28-30, 2013 HERCALES-US Technical Meeting.

### Communications with proceedings in an international congress

- G. Zaz, A. Dekkious, P.A. Meignen, Y. Calzavara, E. Le Clézio, G. Despaux: « **High frequency transducer dedicated to the high-resolution in situ measurement of the distance between two nuclear fuel plates**», *2015 International Congress on Ultrasonics*, 2015 ICU Metz, France.
- G. Zaz, Y. Calzavara, E. Le Clézio, G. Despaux: « **Adaptation of a high frequency ultrasonic transducer to the measurement of water temperature in a nuclear reactor**», *2015 International Congress on Ultrasonics*, 2015 ICU Metz, France.
- G.ZAZ, Pr. E. LE CLEZIO, Dr Y. CALZAVARA, Pr. G. DESPAUX: «**High frequency piezoelectric transducer dedicated to the first experimentation of a high resolution measurement of inter-plate distance in a High Flux Reactor**», *Piezoelectric Micro and Nano Structures and their Applications*, 25-26 September 2014, INSA-CVL, Blois, France.

### Communications with proceedings in a national congress (France)

- M. CHRIFI ALAOUI, G.ZAZ, Dr Y. CALZAVARA, Pr. G. DESPAUX: «**Mesure de distance inter-plaques d'un réacteur nucléaire par méthode ultrasonore haute fréquence**», *7<sup>ème</sup> Colloque Interdisciplinaire en Instrumentation (C2I)*, 2016 Saint-Nazaire (France). (In progress)
- G.ZAZ, Dr Y. CALZAVARA, Pr. G. DESPAUX: « **Transducteur acoustique haute fréquence mesurant la distance inter-plaques d'un réacteur nucléaire** », *6<sup>ème</sup> Colloque Interdisciplinaire en Instrumentation (C2I)*, 2013 Lyon France, p 103-108.
- G.ZAZ, Dr Y. CALZAVARA, Pr. E. LE CLEZIO, Pr. G. DESPAUX : « **Mesure haute résolution in situ de la distance entre deux plaques combustibles nucléaires** », *Congrès Français d'Acoustique*, 22 – 25 Avril 2014 Poitier, p 1191- 1195.

### Communications without proceedings in national and international congress

- G. ZAZ, E. LE CLEZIO, Y. CALZAVARA, G. DESPAUX (2013), « **Mesure de distance inter-plaques par méthode ultrasonore haute fréquence**», *JAPSUS 2013 - XIIIèmes Journées Scientifiques du GAPSUS*, 12-14 Juin 2013, Montpellier.
- G.ZAZ, Y. CALZAVARA, E. LE CLEZIO, G. DESPAUX: « **High frequency transducer dedicated to the experimentation of a high resolution measurement of inter-plate distance in a High Flux Reactor**», *Anglo French Physical Acoustic Conference 2015 (AFPAC 2015)*, 14-16 Janvier 2015, Fréjus, France.